Electronic Thesis and Dissertation Repository

1-26-2024 2:00 PM

The Impact of Simulated Image Acquisition Time Reduction on Image Quality and Parameters of Myocardial Perfusion Imaging Using a Dedicated Cardiac Camera

Alireza Khatami, *Western University*

Supervisor: Stodilka, Robert Z, *The University of Western Ontario*
Co-Supervisor: Warrington, James C, *The University of Western Ontario*
A thesis submitted in partial fulfillment of the requirements for the Master of Science degree in Medical Biophysics
© Alireza Khatami 2024

Abstract

Heart disease is the second leading cause of death in Canada, highlighting the crucial role of early diagnosis in disease management. Myocardial perfusion imaging (MPI), is widely employed for this purpose, involves injecting a radiopharmaceutical into the body, imaging its distribution with a gamma camera, and revealing cardiac blood flow patterns. A significant challenge in MPI is the lengthy 8 to 10 minutes required for stress and rest imaging, potentially causing patient discomfort and compromising image quality due to movement. In a clinical study with 26 patients, post-processed data manipulation simulated a reduction in MPI imaging time. The findings indicated that MPI imaging time can be effectively shortened to 4 and 5 minutes for stress and rest imaging, respectively, maintaining clinical interpretation quality in our cohort. This promising outcome prompts further exploration of timely, comfortable MPI imaging feasibility for managing ischemic heart disease in a broader and diverse patient population.

Summary for Lay Audience

Ischemic heart disease is Canada's second most common cause of death. Myocardial perfusion imaging (MPI), a form of nuclear medicine imaging, is frequently used to help diagnose ischemic heart disease. In MPI, the patient receives a radioactive drug that is distributed in the heart according to its blood flow. The radioactive drug is then imaged using a special camera designed to detect radiation. MPI helps physicians identify if there are any blocked arteries in the heart, causing heart disease. MPI is challenging because the patient must remain motionless for the 8- and 10-minute duration of the stress and rest part of the scan. Any patient motion can comprise image quality and diagnostic value of MPI. One way of minimizing the likelihood of patient motion is to reduce imaging time. However, this can only be done at the expense of image quality degradation.

Our study focused on determining to what extent MPI imaging time could be reduced while still having diagnostically useful images produced. We recruited 26 participants and their images were manipulated by commercial software to simulate imaging time reduction. The results of this study showed that imaging time could be shortened to as little as 4 and 5 minutes from the original 10 and 8 minutes respectively, while still producing diagnostically useful images. These positive findings encourage further exploration into the feasibility of quicker and more comfortable MPI for a broader range of people with ischemic heart disease.

Acknowledgments

Dedication

To my dearly loved wife, Mastooreh,

Throughout my academic journey, your unwavering support, patience, love, and understanding have served as the foundation upon which I have built my achievements. Your steadfast belief in me, even during the most challenging times, has been a constant source of strength and motivation. As I navigated the complexities of balancing family responsibilities with my pursuit of knowledge, you stood by my side as my unwavering rock. Your reassuring presence and words of encouragement became my guiding light, especially when obstacles appeared insurmountable. This thesis not only represents the culmination of my academic endeavors but also symbolizes our shared commitment to personal and intellectual growth. Together, we've embraced the challenges and setbacks, demonstrating resilience and determination in the face of adversity.

To my cherished daughter and son, Hasti and Reza,

You inspire me every day with your curiosity, ambition, and boundless potential. As you navigate your own paths through life, know that your strength and determination fuel my own aspirations. This thesis is dedicated to you, with the hope that it serves as a reminder of the importance of perseverance and lifelong learning.

With love and gratitude,

Table of Contents

List of Tables

List of Figures

List of Abbreviations

2-D	Two-dimensional
3-D	Three-dimensional
AC	Attenuation correction
ALARA	As Low As Reasonably Achievable
BGO	Bismuth germanium oxide
BP	Blood pressure
CAD	Coronary artery disease
CI	Confidence interval
COM	Center of mass
Co-PI	Co-Principal investigator
CT	Computed tomography
CTAC	CT-attenuation correction
CZT	Cadmium-Zinc-Telluride
DCC	Dedicated cardiac camera
EC	Electron capture
ECG	Electrocardiogram
EDV	End-diastolic volume
EF	Ejection fraction
EST	Exercise stress test
ESV	End-systolic volume
FBP	Filtered backprojection
F-18	Flourine-18
Fig	Figure
FWHM	Full-width half max
GE	General Electric
GI	Gastrointestinal
HR	Heart rate
IC	Internal conversion
ID	Identification
IHD	Ischemic heart disease

IR	Iterative reconstruction
KeV	Kiloelectron volts
LAD	Left anterior descending artery
LCX	Left circumflex artery
LOR	Line of Response
LPO	Left posterior oblique
LSO	Lutetium oxyorthosilicate
LV	Left ventricle
LVEF	Left ventricular ejection fraction
MBq	Megabecquerel
MIBI	Methoxyisobutilisonitrile
MLEM	Maximum Likelihood Expectation Maximization
Mo-99	Molybdenum-99
MPI	Myocardial perfusion imaging
MRI	Magnetic resonance imaging
mSv	millisievert
N-13	Nitrogen-13
NaI	Sodium Iodide
OSEM	Ordered Subset Expectation Maximization
PET	Positron emission tomography
PET-CT	Positron emission tomography -Computed tomography
PI	Principal investigator
PMT	Photomultiplier tube
QGS	Quantitative gated SPECT
QPS	Quantitative perfusion SPECT
RAO	Right anterior oblique
Rb-82	Rubidium-82
RCA	Right coronary artery
SD	Standard deviation
SDS	Summed difference score
SMS	Summed motion score
SPECT	Single photon emission computed tomography

SPECT-MPI	Single photon emission computed tomography- Myocardial perfusion imaging
SRS	Summed rest score
SSS	Summed stress score
STS	Summed thickness score
Tc-99m	Technetium-99m
TID	Transient ischemic dilation
Tl-201	Thallium-201
TlCl	Thallium chloride
TPD	Total perfusion deficit
WBR	Wide-beam reconstruction

Chapter 1

1   Introduction

Ischemic heart disease (IHD) is the second leading cause of death in Canada. A report from Canadian Chronic Disease Surveillance System in 2017-2018 demonstrated that every hour, 14 Canadian adults older than 20 years old with heart disease die (approximately 122,000 annually)(1). Though, the trend is declining from 277,000 deaths in 2003(2). The direct economic burden of ischemic heart disease including the cost of hospital admission, physician visits, imaging, laboratory tests and drugs was $3.4 billion in 2018. The indirect cost is related to monetary value of health loss on the economy by losing productivity due to disability, illness and premature health which was higher at $5.7 billion(3).

The word ischemia originated from the Greek word "ischien" which means to suppress, with the suffix "-emia" which means blood. Ischemia means a reduction in blood supply to the tissue, so ischemic heart disease defines a condition of reduced blood supply to the heart muscle by narrowing or obstructing the coronary arteries that supply blood to the myocardium or heart muscle.

Physicians rely on various investigative tools to diagnose IHD including blood work, electrocardiography (ECG), exercise stress test (EST) and non-invasive and invasive imaging modalities. Non-invasive methods include: Echocardiography and stress echocardiography, computed tomography (CT) coronary angiography, magnetic resonance coronary angiography, and nuclear medicine imaging which is called myocardial perfusion imaging (MPI),

The invasive imaging method which is considered the gold standard for the diagnosis of IHD is coronary angiography. In this method, physicians use a catheter inserted through one of the arteries in the upper or lower extremities to reach the coronary arteries and then inject a dye to see the arterial anatomy. This technique is not only a diagnostic tool but also a treatment tool by removing the blockage or narrowing in the coronary arteries with stents and balloon angioplasty if the patient's condition is appropriate for this procedure.

Cardiac imaging is essential in diagnosing, following up, and treating ischemic heart disease(4). Myocardial perfusion imaging prognostic information has an incremental value added to other invasive and non-invasive methods for better evaluation of heart disease(5).

1.1 Nuclear Medicine

Nuclear medicine refers to procedures where radiopharmaceuticals are delivered into the body via oral, respiratory, or intravenous routes; and their distribution visualized to measure body functions and diagnose disease. In therapeutic nuclear medicine, radiopharmaceuticals are delivered in higher quantities to treat some diseases.

A radiopharmaceutical is a radioactive element compounded with other biologically relevant or active molecules. In diagnostic applications, the radiopharmaceutical is administered into the body in very low concentrations, low enough that no pharmacological effect is elicited.

 This radiopharmaceutical localizes in the body based on chemical or other specific characteristics. It emits radiation photons which are detected by a device called a gamma camera. The detected photon has information about the source of radiation inside the body and the intensity of the radiation. The computer uses this information to reconstruct an image. These data also provide information about the function of the organ of interest in the body.

Nuclear medicine is also called functional imaging because in this imaging the function of human organs, including the blood flow, excretion, or absorption of substances can be evaluated by using radiopharmaceuticals. This information is helpful for physicians in clinical decision-making(6).

Nuclear cardiology is a section of nuclear medicine dedicated to imaging the heart. It provides a non-invasive, cost-effective imaging technique used extensively for evaluating and managing coronary artery disease, risk stratification, and some non-ischemic cardiovascular conditions.

There are two categories of imaging devices, one category is called gamma camera because it detects gamma radiation being emitted from the radiopharmaceutical inside the patient. The gamma camera can acquire tomographic information by rotating around the patient. This type of acquisition is referred to as Single Photon Emission Computed Tomography (SPECT). Other type of imaging device in MPI is called Positron Emission Tomography-Computed Tomography (PET-CT) scanner which detects positron emitted from inside of the patient following a positron-emitting radiopharmaceutical injection. The SPECT-MPI is the subject of this study and is the term will be used commonly in this thesis.

SPECT-MPI has emerged as a widely recognized and captivating method for cardiovascular imaging over the last few decades. This technique is widely used worldwide, with an estimated 15–20 million procedures performed annually(7).

The SPECT- MPI evaluates not only the functional parameters of the left ventricle, including volume and ejection fraction (EF) but also the extent and percentage of myocardial ischemia. Study showed that SPECT has incremental prognostic value compared to clinical evaluation and can provide a better direction for further management plan(8).

1.2   Radionuclide and Decay Process

The atomic nucleus contains neutrons and protons. The following notation demonstrates an atom's number of neutrons, protons and mass numbers.

$$^A_Z X_{(N)}$$ X: chemical symbol of an element, A: mass number (# nucleons), Z: atomic number (# protons) and N: number of neutrons.

A radionuclide is an atom with an excess number of energies that makes it unstable. This extra energy escapes in three ways; 1- emission from the nucleus as gamma radiation, 2- creating and releasing new particles from the nucleus and 3- transferring the energy to an electron and releasing it as a conversion electron. The process that an unstable atom losses energy through radiation is called radioactive decay. Some of the radioactive decays are as follows;

1.2.1 Isomeric Transition

Isomeric transition is a form of radioactive decay in which a long-lived metastable parental nucleus loses its energy by emitting gamma rays to reach a more stable status without any changes in the nucleus's number of protons and neutrons. An example of a radionuclide that decays by isometric transition is Technetium-99m (Tc-99m) (Fig.1. 1). The daughter nucleus of the decay process is Tc-99. The dominant decay process of Tc-99m releases gamma rays with an energy of 140 kiloelectron volts (keV). The element in this decay has not changed (the product of the decay is technetium). The gamma rays of this decay process have suitable energy for imaging purposes because they interact very well with the detectors of the gamma camera.
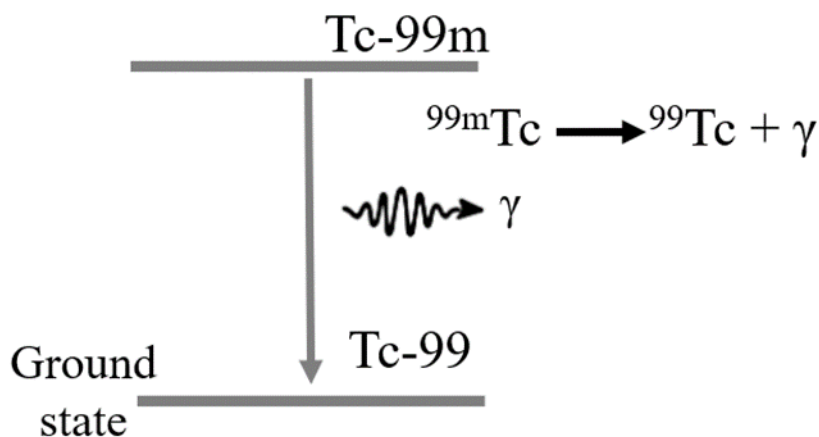
Figure1. 1 Isomeric decay of Tc-99m to ground state Tc-99. The vertical arrow shows the change of the energy level of Tc-99m to a more stable state of energy. Tc-99 has a half live of 2.11 x 10^6 years. The γ defines the gamma rays release in this decay. The notation of the decay is shown in the top right side of the figure.

Other types of decay create high-energy particles due to the loss of neutrons or protons in the nucleus and creating a new element as the decay product.

1.2.2 Beta Minus Decay

In this decay, a neutron-rich nucleus (high numbers of neutrons compared to protons) undergoes decay by converting a neutron to a proton and creating an electron. The decay product is a new element with a mass number the same as the original element (parent's element), but the atomic number increases by one (Fig.1. 2).

$$^{14}_{6}\text{C}$$

$$^{A}_{Z}\text{X} \xrightarrow{\beta^-} {}^{A}_{Z+1}\text{Y} + {-\nu_e}$$

156 kev β^- emission

$$^{14}_{7}\text{N}$$
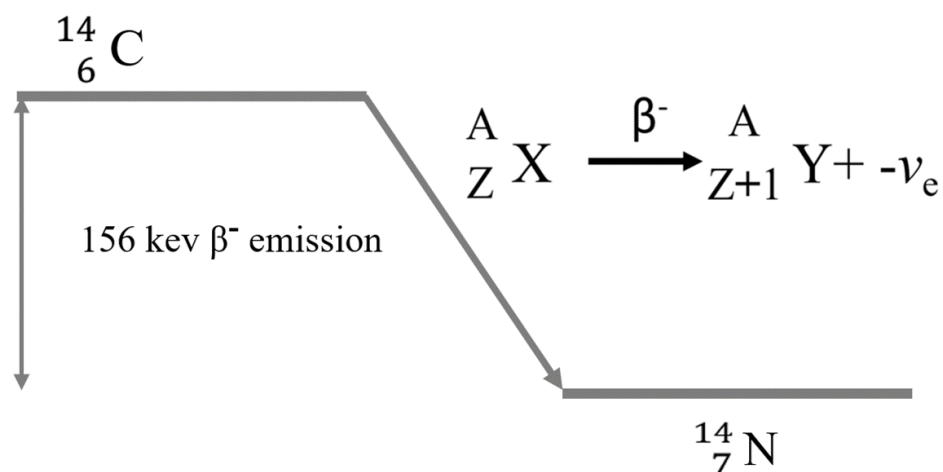
Figure1. 2 A beta minus decay scheme of a C-14 atom. It creates high-energy beta particles with total transition of energy of 156 keV which is shown as a double arrow heads line on the left side of the diagram. The product of the decay is a new element with one proton more than its parent atom, so the decay is to the right as shown by the oblique arrow on the right side because the atomic number Z is increased by one. Part of energy is also released as antinutrino $-\nu_e$. The notation of the decay is shown in the right side of the figure.

1.2.3 Beta Positive Decay

This process involves a nucleus with a high number of protons relative to neutrons. A proton transforms into a neutron, and the nucleus emits a positron. A positron is a particle with a mass like an electron with a positive charge (Fig. 1. 3). Because a positron ejected from atom, the daughter atom has an excess one negative charge compared to its parent atom, so an orbital electron should be released from the atom to reach to a ground state.

Let's review some basic concepts of nuclear physics for better understanding this type of decay and energy changes.

The energy and mass are related to each other through the relationship $E= mc^2$.

Where the E is the kinetic energy in joules, m is the mass in kg and C is the speed of light in vacuum in meter per seconds (m/sec). The basic unit of mass (abbreviated as u) is equal to 1/12 the mass of a C-12 carbon atom, so 1 u is equal to 1.66054×10^{-27} kg. The mass of an electron is $9.1093837 \times 10^{-31}$ kg which is equal to 0.000548 u. Also, we know that the mass of an electron and a positron are the same.

On the other hand, the basic unit of energy called electron volt (eV) which is the energy that an electron acquires when it is accelerated through an electrical potential of 1 volt. The relationship between unit of energy and mass is defined based on the following equation:

1) 1 electron volt (eV) $=1.6022 \times 10^{-19}$ kg.m^2/sec^2 (joules).

By plugging the mass of an electron in relationship of $E=mc^2$, and conversion the energy in joules to eV based on equation 1) we end up with an energy of 511 KeV for each electron. Because a positron and an electron are ejected from an atom in positron decay, the minimum energy for this transition should be 511 KeV x 2=1022 megaelectron volt (Mev) due to loss of these two particles from the atom. The extra energy of the parent atom can be transferred to the positron as kinetic energy of the positron which is varied depends on the atom. For example, in the following decay of O-15 atom, the kinetic energy of the positrons is 1.7 Mev then, the total energy change in this decay is 1.022 MeV + 1.7 MeV = 2.722 MeV.
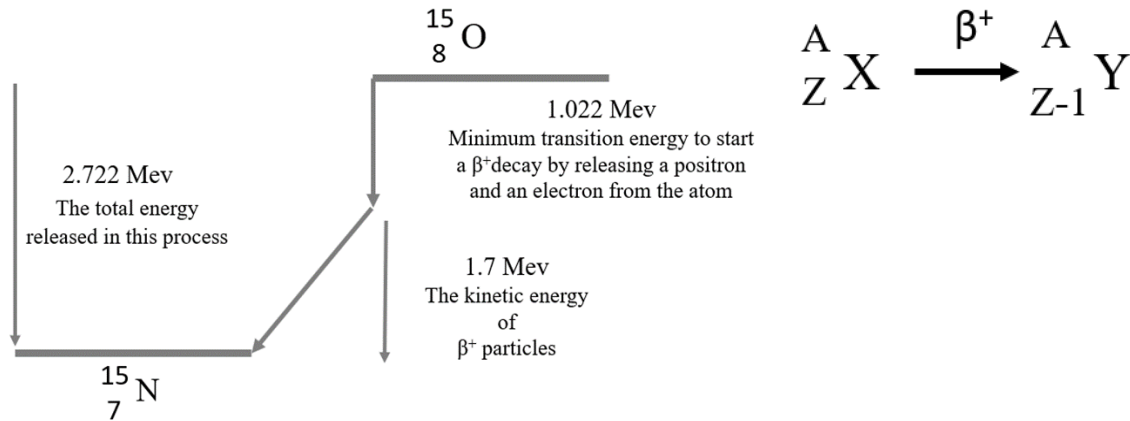
Figure1. 3 Schematic representation of a beta positive (positron) emission decay. The product of the decay is a new element with the same mass number but one proton less than its parent atom so the decay is to the left as it shown by oblique arrow. The transition energy which is shown as the upper small vertical arrow in the middle of the figure is the energy for releasing a positron and an electron from the atom. The long arrow in the left side of the figure is the total energy change in the process of decay which is the sum of the transition energy and the kinetic energy of the beta positive particles which is shown as lower vertical arrow in the middle of the figure. The notation of the decay is shown in the right side of the figure.

Positrons of beta-positive decay are very high-energy particles; however, unlike the product of beta minus decay (beta particles) that are very penetrating, a positron collides an electron due to opposite charges at a very short distance from the source of creation and annihilation occurs which creates two high-energy photons.

1.2.4 Electron Capture EC

This decay process occurs when a nucleus with high numbers of protons captures an internal orbital electron (Fig.1. 4 A). This electron combines with a proton to form a neutron so the decay product is a new element (daughter element) with a mass number same as the original element (parent's element) but the atomic number is reduced by one. The vacancy in the orbital is filled by another electron from the outer layers. The transition of electron between orbitals releases energy as characteristic x-rays. The energy of the

characteristic x-ray releases during the filling vacancy is related to the energy of the K shell electron which depends on the element's atomic number. For example, for Iodine -125 with 53 atomic number is 0.035 MeV. Instead of releasing a characteristic X-ray, the energy released from transition electron in EC decay may be transferred to another outer orbital electron and ejects the electron as an Auger electron. Electron capture daughter element usually is in metastable or excited state which finally releases gamma rays or a conversion electron which is mentioned below to reach to stable state.

1.2.5 Internal Conversion IC

This process defines that an unstable nucleus transfers its energy to an inner orbital electron which is ejected from the atom instead of releasing gamma rays. The ejected electron leaves a which then become filled by an outer orbital electron. The difference of the energy between the outer and inner orbits is released as characteristic x-rays or releasing another outer orbit electron, which is called an Auger electron (Fig.1. 4B).
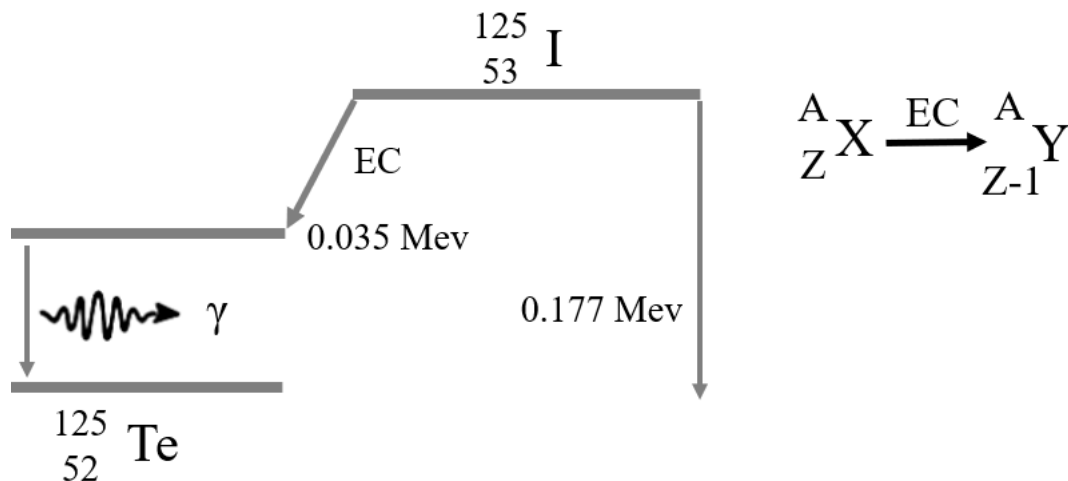
A)
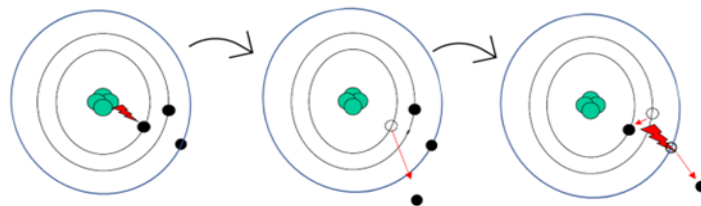
B)

Figure1. 4 A) Schematic representation of electron capture decay of the element X. The product of the decay is a new element Y with the same mass number but one proton less than its parental atom, so the decay is to the left as shown with the oblique arrow. During the electron capture the daughter atom remains in a metastable or excited state which releases its energy as gamma rays as shown with Greek letter γ in the figure. Internal conversion B) is an alternative way of releasing gamma rays energy from unstable nucleus by transferring energy to an inner orbital electron (left), and ejecting an inner orbital electron as beta minus particle (middle). The vacancy is filled by an outer orbital electron. The difference of the energy between the outer and inner orbits may release as characteristic X-rays or the energy may release another orbital electron as an Auger electron (right).

1.2.6 Alpha Decay

In this type of decay, a heavy atomic nucleus emits a particle containing two neutrons and two protons during the decay process. This particle has characteristics identical to a Helium-4 atomic nucleus. The alpha and beta particles are high-energy particles used for treating various diseases in nuclear medicine.

1.3 Types of Myocardial Perfusion Imaging

There are generally two types of MPI, which use different types of radiopharmaceutical and detecting devices.

1.3.1 The SPECT-MPI

Gamma radiation can be detected by SPECT cameras and is used in diagnostic nuclear medicine. SPECT-MPI is an imaging method of the heart using SPECT gamma camera for imaging a gamma emitting radiopharmaceutical.

The most common radionuclide used in the gamma emitting radiopharmaceutical for this technique is technetium 99m (Tc-99m). It is compounded with different ligands to create various radiopharmaceuticals, i.e., Tc-99m Sestamibi or tetrofosmin. Tc-99m predominantly emits gamma rays with 140 KeV energy with 89.1% abundance.

Another radiopharmaceutical used for SPECT-MPI is Thallium-201 (Tl-201). Tl-201 demonstrates poor imaging characteristics because it predominantly (88%) emits lower energy X-rays of 67-82 KeV and with a lower abundance (12%) emits gamma rays with energy of 135 and 167 KeV which are not ideal for creating a high-quality image.

The SPECT radiopharmaceuticals used in MPI have a relatively long half-life, from 6 hours for Tc-99m to 73.1 hours for Tl-201.

Tc-99m is a product of the Molybdenum-99/ Technetium -99m generator (Mo-99/ Tc-99m or Moly generator) by decaying parent radionuclide Mo-99 with a half-life of 66 hours to a daughter radionuclide Tc-99m with a half-life of 6 hours. Tc-99m can be obtained by means of a process called elution from Moly generator. During approximately 24 hours after each elution, the amount radioactivity in form of Tc-99m generated by the generator has reached its maximum. This level of radioactivity is useful for operating the nuclear medicine department's radiopharmacy during the next day. Because of the decaying parent radioisotope (Mo-99), the amount of daughter radionuclide (Tc-99m) created by the generator system reduces over time and reaches a level which is not enough for running the radiopharmacy so the generator should be replaced approximately every week.

The 6-hour half-life of Tc-99m enables physicians to image patients up to one hour after the radiopharmaceutical is injected into the patient. This time delay is important in MPI, as radiopharmaceuticals injected into a patient are not only absorbed by the heart muscle but also accumulated in the liver, gallbladder and stomach. Delayed imaging makes it possible to have a good image quality by letting the remaining background activity in the blood removed and the accumulated radioactivity in the liver, and gallbladder further excreted to bowel and moved away from the imaging field of view to distal part of the bowel. This delay causes a better image quality by a better target (uptake in the heart) to background uptake and signal to noise ratio. Long half-life is also important for acquiring imaging for EST-MPI.

For an EST, patients receive radiopharmaceuticals during activity on a treadmill or a bike, not under a gamma camera. The test lasts 15-minute and the patients are being monitored for a few minutes later. If radionuclide has a short half -life like majority of current PET

radionuclides, the time of exercise and monitoring patient will cause decaying the radionuclide to such a degree that the quantity of remaining radioactivity inside the body is not enough for a good quality imaging. For these reasons Tc-99m radiopharmaceutical is appealing for MPI.

1.3.2 Positron Emission Tomography (PET)-MPI

A positron is an anti-matter particle which is created as part of the decay process from a positron-emitting radionuclide. From the decaying site, it travels inside the body until it encounters an electron, then the positron and electron are both annihilated and 1022 KeV energy is released from that annihilation. The energy is released in the form of two 511 keV photons travelling in approximately opposite directions. A conventional SPECT camera, using either NaI crystals or solid-state detectors can detect 511 KeV photons. However, that detection's efficiency is poor, resulting in unacceptable image quality. Thus, conventional SPECT cameras are not used to image positron-emitting radiopharmaceuticals.

Imaging of positron-emitting radiopharmaceuticals is performed by PET scanners. A PET scanner is similar to a SPECT camera, in that it employs scintillating crystals coupled to a photomultiplier tubes. However, denser scintillators are chosen to detect high energy photons efficiently. Examples of denser scintillators include bismuth germanium oxide (BGO) and lutetium oxyorthosilicate (LSO).

A PET scanner is designed to acquire images from positron-emitting radiopharmaceuticals. Myocardial perfusion imaging with a positron-emitting radiopharmaceutical is called PET-MPI. The PET scanner is usually coupled with an X-ray CT system, and this instrument is called a PET-CT scanner.

The half-lives of the majority of positron-emitting radionuclides are very short. The most common positron-emitting radionuclides used in nuclear cardiology are Rubidium-82 (Rb-82), with a half-life of 76 seconds, and Nitrogen-13 (N-13), with a half-life of 10 minutes. These short half-lives make them unsuitable for an EST during PET-MPI; however, they are ideal agents for pharmacologic stress PET-MPI. Unlike SPECT radiopharmaceuticals,

positron-emitting radiopharmaceuticals are created by a cyclotron (although Rb-82 is created in a generator). Cyclotrons are expensive and not available in every city or province. A new PET radiopharmaceutical using Fluorine-18 (F-18) as radionuclide called F-18 Flurpiridaz has a long half-live of 110 minute which is optimal for performing EST-MPI with a PET scanner. This radiopharmaceutical is under evaluation by FDA to receive its approval in the near future.

1.4 Coronary Circulation

Like other tissues, heart muscle (myocardium) needs a blood supply to maintain their function. Unique coronary artery circulation, unlike the rest of the body, provides temporal blood supply to the myocardium during the diastolic phase of the cardiac cycle. In this phase, the aortic valve is closed, and the ventricular muscle is relaxed, allowing blood flow from the aorta to the myocardium.

Myocardial perfusion involves the epicardial coronary arteries, arterioles, and endothelial layers. Epicardial coronary arteries commonly comprise 1) the left main coronary artery, further divided into the left anterior descending artery and the left circumflex artery and 2) the right coronary artery. Left and right coronary and circumflex arteries are further divided multiple times to reach very small-sized vessels, arterioles which distribute blood to capillary beds. Small arteries with a diameter of less than 300 micrometres, including arterioles and capillary vessels, create coronary microcirculation, which regulates flow resistance and perfusion to the myocardium. Arterioles are the resistive part of the myocardial microcirculation, which means these vessels have muscular layers in their walls that constrict or relax in response to the nervous system and the presence of chemicals in the blood. By constricting and relaxing, these vessels regulate the perfusion to the myocardium in various situations(9). The endothelial layer has a vital role in coronary artery hemodynamics.

The endothelium releases some mediators, including vasodilators, especially nitric oxide, and vasoconstrictors. The vasodilator substances are released in response to increased blood pressure. Damage to the endothelial layer by chronic increased blood pressure, typical of patients with hypertension, or an increase in serum cholesterol and triglycerides,

as seen in hyperlipidemia, can cause endothelial dysfunction, which is defined as a reduction of vasodilators and an increase of vasoconstrictor substances. A study by Zeiher et al. showed that endothelial-dependent vasodilation does impair in an early stage of epicardial atherosclerosis, so the consequence of epicardial atherosclerosis may extend into the coronary microcirculation. The phenomenon of releasing nitric oxide by endothelium in response to increased pressure inside vessels is called the flow-mediated endothelial-dependent release of nitric oxide, which is impacted by atherosclerotic changes in coronary arteries(10).

1.5 Kinetic Characteristics of Myocardial Perfusion Agents

1.5.1 Radiopharmaceutical Uptake Versus Flow

Myocardial uptake and concentration of a radiopharmaceutical depend on the quantity of the radiopharmaceutical delivered to the heart through coronary artery blood flow and the extraction fraction of the radiopharmaceutical by myocardium. The following equation demonstrates the relation between net uptake and flow.

Net uptake= F x (C_A-C_V)

Where F is the blood flow to the organ in mL/min, C_A is the concentration of the radiopharmaceutical in arterial blood in mg/mL and C_V is the concentration of the radiopharmaceutical in the venous blood in mg/mL.

Extraction of a radiopharmaceutical occurs across the membranes of the capillary endothelial cells and myocytes.

The Renkin-Crone model assumes that extraction fraction from blood to tissue (unidirectional extraction) is related to the permeability P, surface area S of the capillary bed and blood flow F through a capillary.

The following equation demonstrates the relationship between the extraction fraction of the radiopharmaceutical and the above-mentioned parameters. E_u defines the extraction fraction.

$$E_{u=}1 - e^{-(PxS/F)}$$

As we can see, the extraction fraction reduces by increasing the blood flow.

For a radiopharmaceutical to be useful, it is important to know how efficiently the radiopharmaceutical is absorbed by tissue, and what factors affect that efficiency. For many radiopharmaceuticals, the rate at which they are absorbed depends on blood flow. For an ideal radiopharmaceutical, there is a linear relationship between radiopharmaceutical uptake and blood flow. This simple relationship makes it relatively straightforward to determine blood flow, provided the radiopharmaceutical's uptake can be measured. At this time, there is only one radiopharmaceutical that is known to have such an ideal linear relationship: the PET radiopharmaceutical oxygen-15 H_2O. See diagram in fig.1.5. Unfortunately, oxygen-15 H_2O is impractical and expensive to use since it radioactively decays quickly (with a 2-minute half-life) thereby requiring a nearby medical cyclotron for its production.

The most common radiopharmaceutical used in blood flow measurements is Tc-99m sestamibi. This radiopharmaceutical is convenient and inexpensive. However, the uptake of Tc-99m sestamibi is less than ideal. At low blood flow rates (less than 1 mg/min/g) it exhibits a linear relationship with blood flow. However, as blood flow increases, the uptake of Tc-99m sestamibi demonstrated a roll-off phenomenon and reaches to a plateau with no further increased in uptake by increasing blood flow. This plateauing feature complicates the extraction of blood flow information from MPI using this radiopharmaceutical.
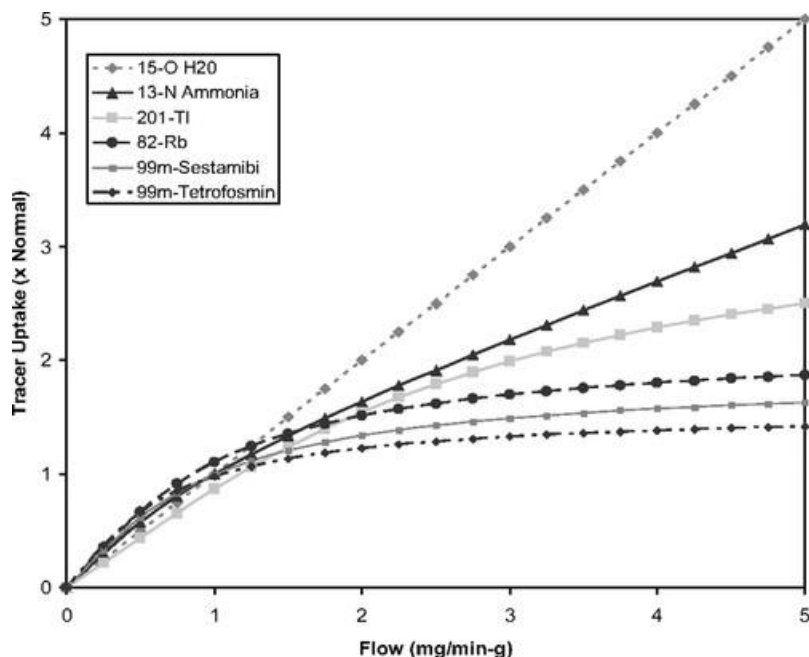
Figure1. 5 The relationship between myocardial blood flow and SPECT and PET perfusion agents' uptake demonstrates a roll-off phenomenon at high flow rates. It results in reduced sensitivity for less severe coronary stenosis. Adapted from Michael Salerno. Circulation: Cardiovascular Imaging. Noninvasive Assessment of Myocardial Perfusion, DOI: (10.1161/circimaging.109.854893)(10).

1.5.2 Myocardial Kinetics of the SPECT Radiopharmaceuticals

An ideal perfusion radiopharmaceutical should possess the following five characteristics. #1) It should demonstrate high first-pass extraction, the percentage of radiopharmaceutical extracted from blood flow to the myocardium during the first circulation through the myocardium. The ideal extraction should be close to 1.0. The extraction mechanism is different based on the type of radiopharmaceutical. It could be an active extraction using a transport system, meaning that the radiopharmaceutical is actively transported into the myocyte by cell-membrane through a Na+/K+ pump or a passive diffusion through endothelial, interstitial, and intracellular sarcoplasmic membranes. #2) The radiopharmaceutical should be stable and maintain retention within a viable myocardial tissue. #3) It should demonstrate a proportional uptake to blood flow in a wide range of

blood perfusion rates.. #4) It should demonstrate less uptake by adjacent structures, including the liver, gastrointestinal (GI), and lung, which impacts the image quality. #5) The radiopharmaceutical should demonstrate excellent characteristics for imaging, such as having a gamma emission energy 100-300 keV, a half-life longer than biokinetics (but not so long as to create excessive radiation burden to the patient), and chemical stability (meaning the radionuclide does not separate from the radiopharmaceutical molecule).

Thallium-201 Chloride (Tl-201 Cl) was introduced in 1976 as the first useful radiopharmaceutical for myocardial imaging(11). Tl-201 is a metallic element with properties resembling potassium in the biological environment and can substitute potassium to activate the K-Na ATPase pump. The mechanism of absorption of this radiopharmaceutical is an example of active transport. Because active transport needs energy, the cell should be viable and have intact cellular and sarcoplasmic membranes. The uptake of Tl-201 Cl is proportional to myocardial blood flow in a wider range of blood flow compared to the newer SPECT radiopharmaceuticals though, it also demonstrates roll-off phenomenon and approaches to plateau in higher flow rate compared to Tc-99m Sestamibi (Fig 1. 5).

The low photon energy of 80 KeV and a long half-life of ≈ 73 hours make it less desirable for imaging due to the high radiation dose to patients(9).

Today, the most common radiopharmaceutical used for SPECT MPI is Technetium-99m sestamibi. The radioactive decay of Tc-99m results in the emission of a 140 keV gamma-ray, which is suitable to interact with the Sodium Iodide (NaI) detectors of SPECT gamma cameras. Tc-99m also has a shorter half-life of 6 hours compared to a longer ≈ 73 hours half-life of Tl-201.

Unlike with Tl 201 Cl, there is no active transport for the uptake of Tc-99m Sestamibi. This radiopharmaceutical has a positive charge due to the Tc-99m atom in the compound.

Tc-99m Sestamibi diffuses passively into the myocardial cell because of the lipophilic characteristics of the radiopharmaceutical. However, the net uptake/ retention within the myocardium is driven by a negative transmembrane potential, mainly at the level of the

sarcolemma and mitochondrial membranes. This later process is energy-dependent, and the energy maintains the transmembrane potential(12)(13) so only viable tissue with membrane integrity can uptake Tc-99m Sestamibi. Otherwise, redistribution with washout of the radiopharmaceutical will happen(9)(10). For this reason, Sestamibi is applicable for the evaluation of perfusion and viability of the myocardium(10).

1.5.3 Biodistribution of Tc-99m Sestamibi

Technetium 99m-Methoxyisobutilisonitrile (Tc-99m Sestamibi) is one of the most common myocardial perfusion agents. Its biodistribution is characterized by rapid blood clearance and early uptake by the myocardium. The first pass extraction of Tc-99m Sestamibi is 55-68%, and the myocardial uptake is about 1.2% at rest and 1.5% post-stress of the total injected activity(10). Blood clearance of Tc-99m Sestamibi has a half-life (T ½) of 4.3 min during rest imaging and 1.6 min on post-stress imaging. The myocardium and the liver take up Tc-99m Sestamibi. However, the half-life of the radiopharmaceutical in the heart is approximately six hours, but in the liver, it is 0.5 hours.

The liver demonstrates initial intense uptake, which clears up to the gallbladder about an hour post-injection. The optimal time to have a enough quantity of radiopharmaceutical absorbed in the heart compared to the adjacent structures like the liver, lung or bowel for a good quality image target-to-non-target ratio is between 60 and 90 minutes post-injection(12). However, in practice, there is a 30–45-minute delay between the radiopharmaceutical injection and imaging in MPI to account for liver uptake clearance. The kidney participates in a small fraction of the excretion of sestamibi.

1.6   Imaging Equipment

1.6.1 Anger Gamma Camera Systems

Hal Anger developed an early form of gamma camera in 1952. This camera employed a pinhole absorptive collimator and a large flat crystal of thallium activated NaI coupled with a photographic plate. This device could generate an image from a tumour utilizing 740 MBq of radiopharmaceutical activity. This process was referred to as radioautography(14).

1.6.2 Single Photon Emission Computed Tomography (SPECT) Gamma Camera

Hal Anger's work led to the development of more advanced cameras. Modern SPECT gamma cameras still use the same concept which Hal Anger employed in his original camera, so that SPECT cameras are also referred to as Anger gamma cameras(15). The SPECT camera, designed to detect gamma rays, has five essential components: A collimator, detectors, electronics, a computer unit and a gantry system.

1.6.2.1 Collimators

Collimators in gamma camera are absorptive collimators which are made from heavy material like lead or tungsten. The collimator is placed anterior in relation to the gamma camera. It projects the image of the source distribution originating from inside the body onto the detector by allowing the gamma rays to travel in certain directions(16). The collimator directs photons toward the detectors by defining a line of response (LOR). More specifically, the collimator prevents gamma rays not aligned with the direction of the holes from reaching the detector. The effect of the collimator is to help to improve image quality by absorbing photons which do not have good information pertaining to the source distribution so that such photons do not reach the detector. This comes at the cost of absorbing more than 90% of the photons en route between the source distribution and the detector(17).

The most common collimator in use in SPECT gamma camera is a parallel hole collimator. Other types of collimators are converging, diverging, and pinhole collimators. The new dedicated cardiac camera (DCC) employs pinhole collimators instead of a parallel hole collimator. Fig.1. 6 schematically demonstrates different types of collimators.
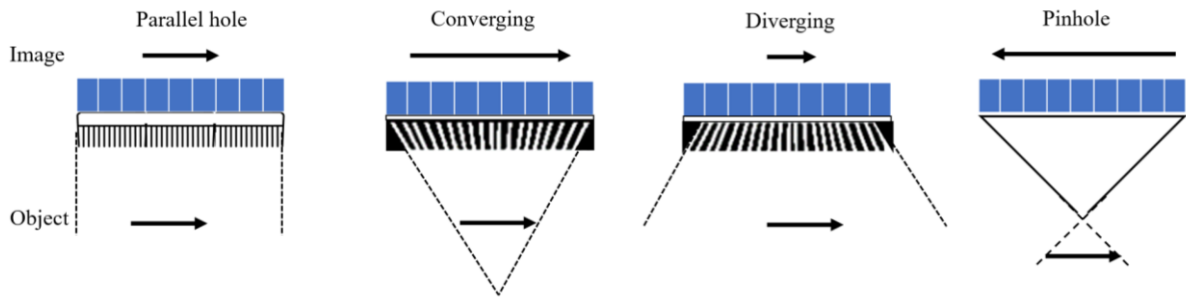
Figure1. 6 Various types of collimators and their impact on the image of an object.

1.6.2.2 Detectors

Detectors play a central role in the operation of a gamma camera. They are composed of NaI crystals which receive photons passing through the collimator. These photons interact with the detector's substances in two major interactions, the photoelectric effect (a beneficial interaction) and Compton scatter (which is not helpful from an imaging perspective). The photoelectric effect produces optical photons at the detector surface, so these detectors are referred to as scintillation detectors.

Each crystal is optically coupled to a device called a photomultiplier tube (PMT), the role of which is to capture the optical photons created at the surface of the detector. The PMT produces electrons in response to each light photon it receives, intensifies these electrons by a factor of millions, and converts these electrons at the anode end of the device to a measurable electrical signal.

There are other types of detectors, such as photodiodes and semiconductors. These other detectors are smaller than the combination of NaI crystals plus PMT and have higher efficiency (Fig.1. 7).
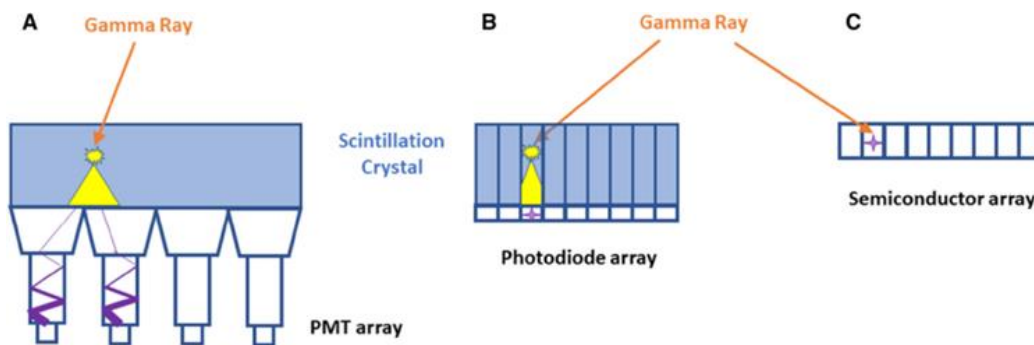
Figure1. 7 Various types of detectors; Left) scintillation crystal with NaI and PMT. Middle) photodiode array scintillation detector. Right) Semiconductor detectors. Adapted with permission from Dorbala S et al. Single Photon Emission Computed Tomography (SPECT) Myocardial Perfusion Imaging Guidelines: Instrumentation, Acquisition, Processing, and Interpretation. *J Nucl Cardiol* [Internet]. 2018;25(5):1784–846(18).

1.6.2.3 Electronics

These components receive pulses from PMTs and amplify and convert pulses from analog to digital signals. Electronics detect the position of pulses (events) on the detector surface and measure energy signals. The electronic circuits are coupled to each photomultiplier tube. They localize the position of the interaction on the detector surface and determine the timing of photon gamma-ray interaction on the surface of the detectors(17). The electronics create x and y coordinates for each event (scintillation) on a crystal(16). Electronic circuits also analyze the energy of the interacting photons and reject signals with lower threshold energy to prevent their contribution to image reconstruction.

1.6.2.4 The Computer System

The computer system is the central processing component of the camera. The information from the interaction of the gamma photon on the detector from the previous steps is converted into signals, time-stamped, passed through localization circuits, and finally sent to a computer for analysis and creation of a two-dimensional (2D) image.

1.6.2.5 The Gantry System

A supporting system which holds and moves the gamma camera around the patient(17).

1.7 Single Photon Emission Computed Tomography- Myocardial Perfusion Imaging (SPECT- MPI)

Myocardial perfusion imaging MPI is an important modality in diagnosing ischemic heart disease. SPECT-MPI often starts with the injection of a radiopharmaceutical into blood circulation. This radiopharmaceutical is taken up by myocardial cells (myocytes), becomes entrapped within such cells, and decays to the ground state by emitting gamma-ray photons. The most common SPECT camera utilizes two detectors. The detectors convert non-visible photons into optical photons, amplify the signal and convert optical photons into electrical signals(19).

The SPECT camera suffers from relatively low spatial resolution with a full-width half max (FWHM) of 10.5 mm. Also, detector sensitivity is somewhat low using the traditional SPECT technique, thereby requiring higher activity of radiopharmaceutical and longer patient image times under the camera to maintain image quality.

Using a collimator reduces the number of photons interacting with the detector, effectively reducing the signal produced by the detector because of poor count statistics.

The poor count statistics cause reduced energy resolution. The low energy resolution is associated with image contamination by scattered photons which further reduces spatial resolution(15).

Besides conventional SPECT cameras, DCC with Cadmium-Zinc-Telluride (CZT) detectors and PET-CT represent other nuclear myocardial perfusion imaging modalities.

Myocardial perfusion imaging provides static and functional information derived from the radiopharmaceutical distribution. Acquisition of images in different physiological conditions, such as at rest, during stress, and depiction of morphologic changes throughout the cardiac cycle (gated images) provides both perfusion data and cardiac wall motion-related information(20).

1.8 Conventional SPECT-CT Scanner; Discovery NM/CT 670 Pro

A SPECT-CT scanner is a device which integrates two diagnostic modules. The gantry of a SPECT-CT scanner includes a SPECT scanner coupled with a X-ray CT scanner. The SPECT and CT scanners share a common bed used to move the patient through both scanners sequentially.

The CT component of the hybrid SPECT-CT camera is mainly used for attenuation correction (AC). CT attenuation correction (CTAC) refers to transmitting CT x-ray photons through the body. After passing through the patient's body, the x-ray photons interact with a detector which effectively measures x-ray photon attenuation. The reconstructed CT transmission scan is used for attenuation correction of radionuclide images(21). In conventional SPECT imaging, myocardial perfusion data are acquired by rotating a two-headed gamma camera (which contains two planar detectors) in an orbital fashion around the patient covering 360 degrees of the patient's outer surface. The gamma photon energy and position in this camera are determined from the interaction of the gamma photon with either one of the detectors, each covering 180 degrees of the outer patient surface(15). Fig.1.8 demonstrates a conventional SPECT-CT camera (GE Discover NM/CT 670 pro)

Figure1. 8 A conventional SPECT-CT camera with two detectors, GE Discovery 670 Pro.

1.9 New Dedicated Cardiac Camera DCC

The limitations pertaining to conventional gamma cameras described in section 1.7 motivated researchers to design faster cameras with higher spatial resolution and better image quality.

One advancement in the design of gamma cameras stems from the development of semiconductor detectors. These detectors have better photon detection compared with scintillation detectors. Signal production for semiconductor detectors occurs by direct electron-hole creation following interaction with gamma-ray photons and eliminating the scintillation process and PMTs. These detectors are highly efficient in electron creation and are as small as 2.5 x 2.5 mm pixel size. This small size improves image spatial resolution.

The chemical constituents used in this type of detector are mainly cadmium, zinc, and telluride or CZT. This type of detector is popular in the new DCC for SPECT- MPI, so these cameras are also known as CZT cameras.

Various companies manufacture different types of DCCs. A key feature of DCC operation is that its detectors are stationary, unlike its predecessor, Anger SPECT cameras, whose detectors rotate 180 degrees around the patient.

1.9.1 Discovery NM 530 SPECT Camera DNM 530

Discovery NM 530 is a prototype of DCC (Fig.1. 9). The technology of this camera combines a multi-pinhole collimator with a multidetector array of pixelated CZT detectors. The combined detectors and pinhole collimators focus on the heart. The size of the CZT modules in this camera is smaller than the NaI detector, and each module is 4 x 4 cm with pixelation as small as 2.45 x 2.45 mm. This technology allows multiple stationary detectors to acquire images from the heart simultaneously to ensure enough information for a three-dimensional sampling of the heart(15).

This camera is different from a conventional camera in the following aspects: A) the system uses 19 CZT detectors, each coupled with a pinhole collimator, B) these detectors are fixed in position, in 3 arrays with a U-shaped configuration located in front and left posterolateral positions in relation to the patient's chest, gathering photons emitted from the patient in a 180 degrees arc extending from the RAO (right anterior oblique) to LPO (left posterior oblique) positions, C) all collimators are centered on the assumed position of the heart in the chest, perpendicular to the longitudinal patient axis (Fig.1. 10 & 11).

The advantages of the new CZT camera over conventional SPECT-CT cameras are;
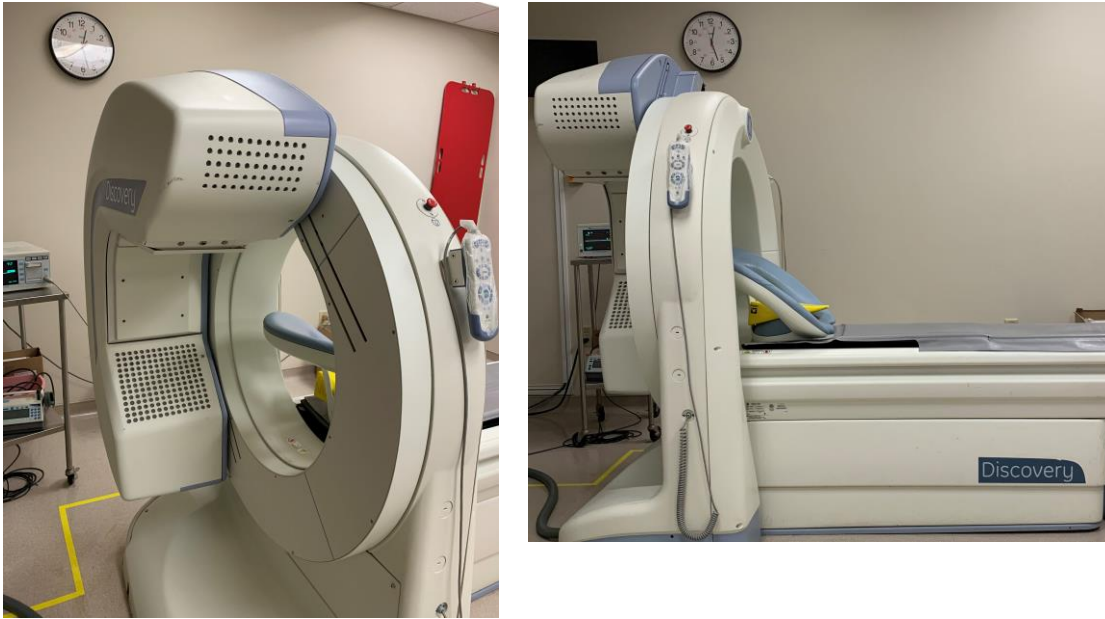
Figure1. 9 Photographs of Discovery NM 530 SPECT Camera.

Discovery NM 530C   Detector configuration in Discovery NM 530C

Fixed detectors
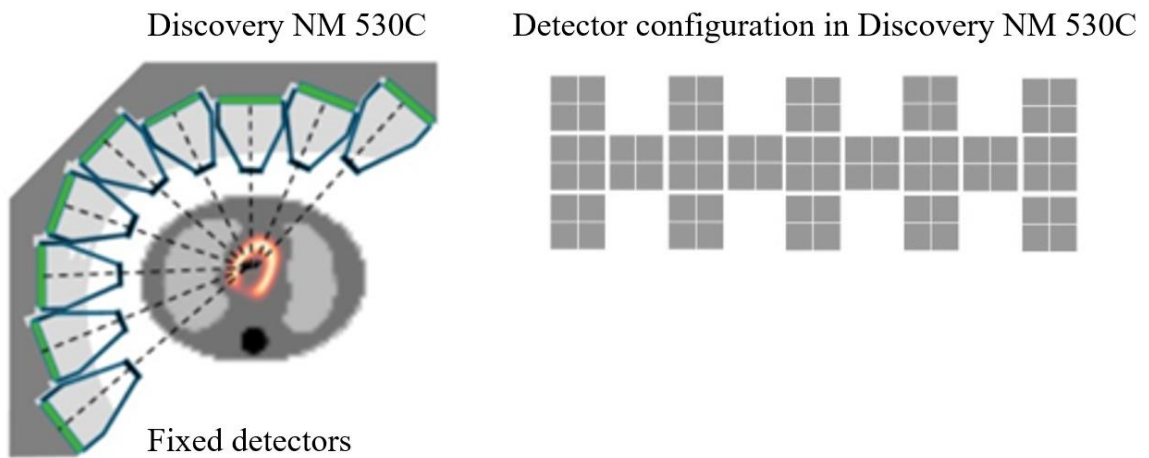
Figure1. 10 Position of the detector array in DNM530 and schematic focus of the detector-collimator modules toward the heart. A adapted from Ljungberg M et al. SPECT/CT: an update on technological developments and clinical applications BJR 2018 with permission(22).
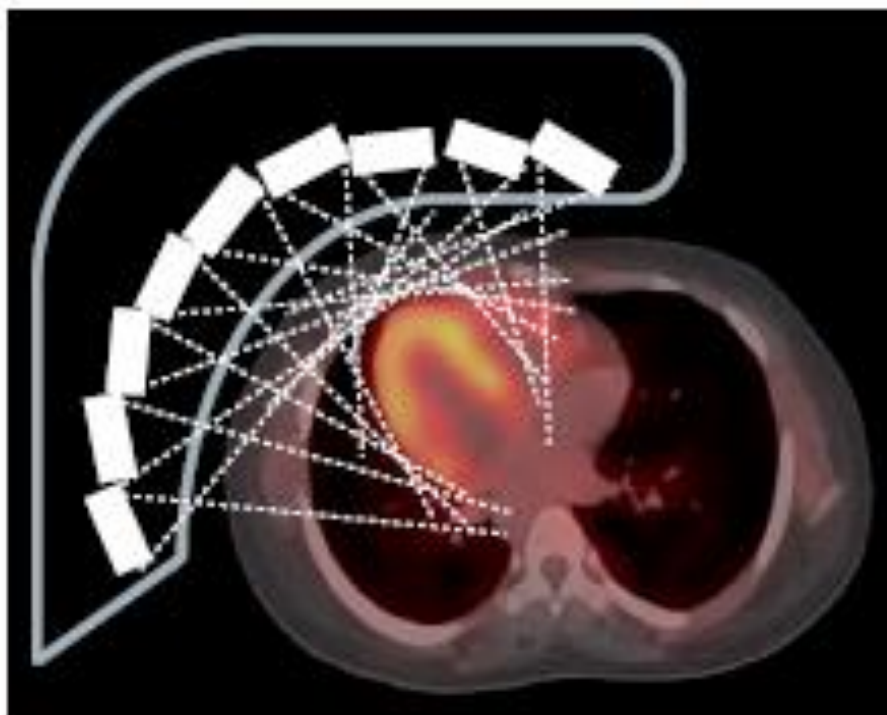
Figure1. 11 Schematic representation of myocardial perfusion image acquisition
by DNM530 cardiac camera adapted from Dewey M et al(4).

This design resulted in enhanced sensitivity of 5 to 10 times, achieved by directing each
detector field of view specifically towards the heart (Fig.11)(23)(24)(25), along with an
improved spatial resolution of 6.7 mm (in contrast to the 10.5 mm of conventional
cameras), and faster data acquisition.

1.10 Differences Between Two Types of Cameras and Challenges of SPECT MPI

There has been much prior work committed to the optimization of image acquisition and
development of reconstruction algorithms for more precise image reconstruction on DCC
cameras.

The conventional SPECT camera uses standard parallel-hole collimators developed nearly half a century ago. This collimator allows only a small fraction of incident photons to pass through. The photons then subsequently interact with the NaI detector. The detection of photons by the parallel-hole collimator-detector combination is quite inefficient as there is a low proportion of photons approaching the collimator which interact with and are registered by the detector.

The introduction of solid-state detector technology represents a relatively new technological advancement in SPECT camera systems. The small-sized semiconductor detectors which directly convert gamma-ray photon energy into an electrical signal (i.e.,digitize the image acquisition directly without the need of NaI detectors and PMTs) have been regarded as revolutionary.

DCC employs a series of detectors surrounding the patient, which image the heart simultaneously with a pinhole collimator with solid-state CZT detectors. These detectors provide a 5-10-fold increase in count sensitivity with no loss of resolution(23)(24)(25). Nudi et al(26) in a meta-analysis composed of 2092 evaluating the diagnostic accuracy of CZT SPECT in comparison of invasive coronary angiography showed that the CZT SPECT system has a high sensitivity of 84% (95% Confidence interval CI:0.78 to 0.89) and a specificity of 69% (95% CI:0.62 to 0.76) for demonstrating obstructive coronary artery disease.

Image reconstruction algorithms and software employed in conventional dual-headed SPECT CT for use in DCC with CZT detectors has been validated in previous work. In practice, some differences between the normal reference range of LV volumes and left ventricular ejection fraction (LVEF) calculated by two cameras should be considered. For example, LV volume was larger, ranging from 12-27%, and LVEF was 5-15% lower, for CZT cameras as compared with conventional SPECT cameras(27). Fig. 1. 12 schematically demonstrates the difference in the field of view between the two types of cameras.
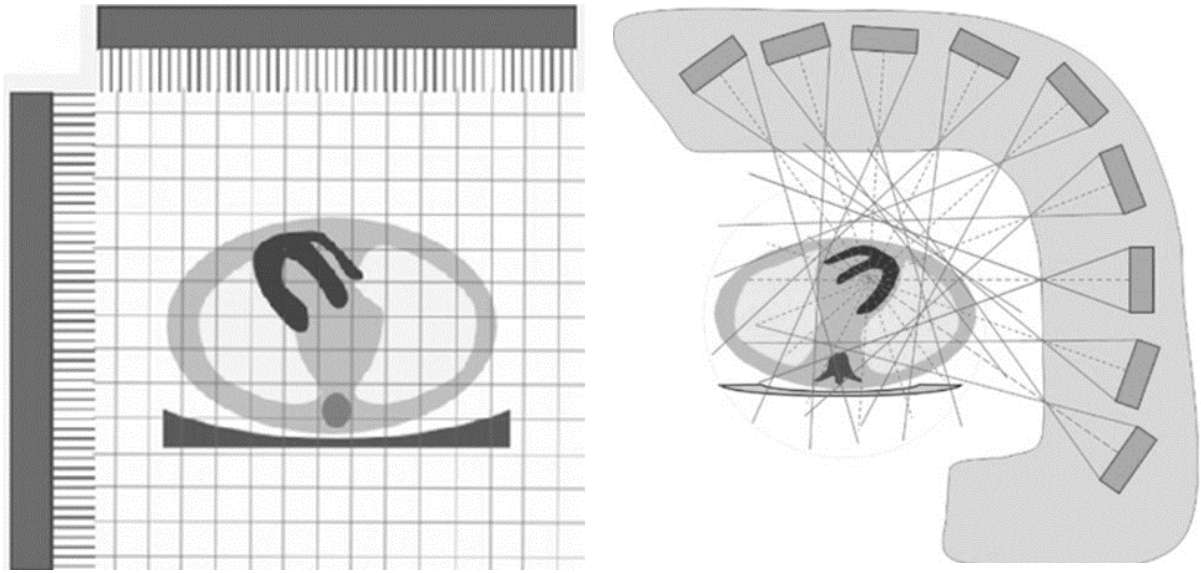
Figure1. 12 Field of view of a conventional dual-detector SPECT with a parallel hole collimator on the left, a dedicated cardiac camera and its 19-pinhole detectors are all directed at the heart on the right. (Adapted from 'Brian G. Abbott(28) with permission).

A disadvantage of conventional parallel hole collimators is loss of resolution with increasing source distance away from the collimator. A software improvement known as resolution recovery with iterative image reconstruction addresses the loss of resolution and mathematically corrects the resolution degradation. This algorithm suppresses noise as additional counts become available to generate a more accurate image and thereby lessen noise.

The 5 to 10-fold increased sensitivity for DCC compared with more conventional cameras (gained without a corresponding loss in resolution) has the potential advantage of rapid acquisition of a myocardial perfusion stress scan in 2 min with a standard injected activity while maintaining the same image quality of a conventional SPECT camera with 14-16 minutes of image acquisition and the same radioactive amount. The increased sensitivity of the detector also allows a lower radiation dose across a wider range of patient body habitus including high body mass index (BMI). The CZT detector of the DCC demonstrates

improved spatial and energy resolution compared with more conventional detectors(15)(29).

This high sensitivity enables the acquisition of high-quality images with shorter imaging times or smaller injected radiopharmaceuticals activity, is the latter being beneficial toward lowering the administered radiation dose to patients.

There have been studies aimed at shortening imaging time from 15–30 min using conventional SPECT scanners down to 2–3 min with a dedicated cardiac camera with CZT detectors while using a standard amount of injected radioactivity(30)(31).

Researchers demonstrated the potential of CZT detectors in dose reduction. They reconstructed images acquired by a dedicated cardiac camera with an iterative reconstruction algorithm called Ordered Subset Expectation Maximization (OSEM) with attenuation, scatter, and resolution recovery and showed that the image could be diagnostically accurate until injected activity was reduced to 25% of the initial administered activity (32).

A new recent multicenter trial comparing conventional SPECT and DCC cameras suggested that imaging with a DCC camera can be completed with an effective dose as low as one mSv. At the same time, the image quality remained superior to that obtained with a conventional SPECT camera(33).

1.11 Data Processing and Image Reconstruction

1.11.1 Tomographic Image Reconstruction in Nuclear Medicine

Imaging a 3-dimensional (3-D) object is challenging because the structures in front and back of it can obliterate an internal structure. Tomographic imaging addresses this issue by acquiring multiple two-dimensional 2-D images of a 3-D structure in a given plane. These images are acquired by positioning rotating detectors around the patient. The detectors take multiple images at different angular views, which are used for image reconstruction using various mathematical algorithms.

A one-dimensional projection profile of an object is created when a detector images an object in a single angular view or projection. (Fig.1. 13). As the detector acquires multiple such angular views, these profiles contain a complete representation of the distribution of radioactivity inside the object. All the acquired one-dimensional projection profiles are stacked along each other and generate a projection profile called a sinogram. A sinogram is a 2-D representation of the intensity of a set of projections (Fig.1. 14).
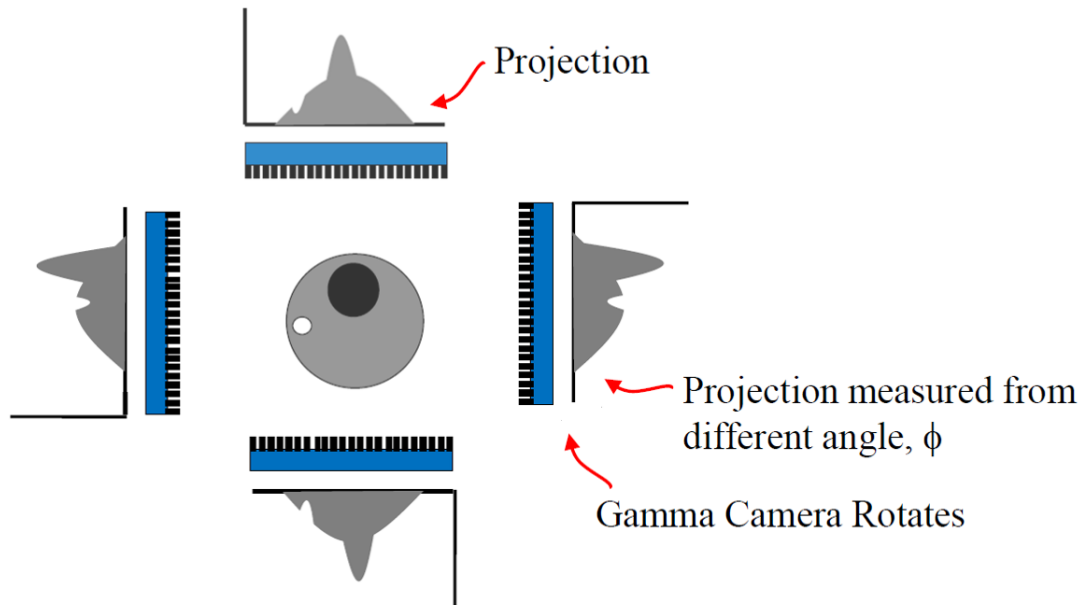
Figure1. 13 Schematic representation of angular projection around an object in one slice.
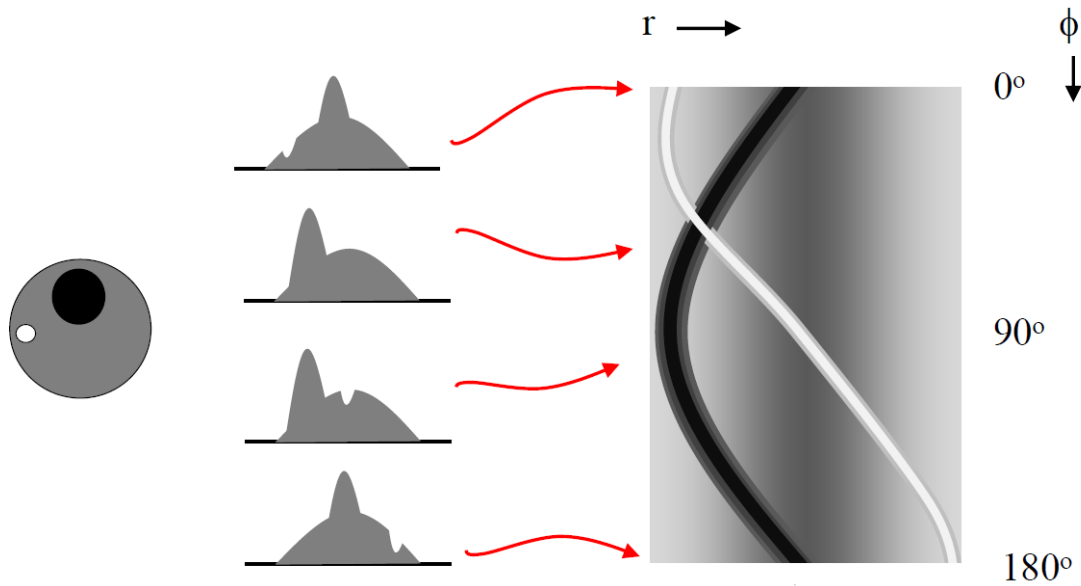
Figure1. 14 A sinogram of projection profiles (r) and angular views of the projection (Φ).

1.11.2 Filtered Backprojection FBP

A conventional SPECT camera acquires projections from the source of radioactivity inside the body by rotating the detectors around the patient at various angles. Stationary detectors at various positions around the body in CZT cameras replace this step.

Image reconstruction is used to create a 3-D image from projection data. The 3-D images are then used for review by physicians. There are various algorithms which can be employed in image reconstruction.

FBP is one of these algorithms. FBP gathers projections along multiple though selected lines of response (LOR) on a sinogram. Backprojection works by recasting or spreading the profile of a single angular projection across the image from one edge to the other along the angle of the projection. The value of each pixel recorded along each LOR from which the photon originated is spread back along the image (Fig.1. 15 A-B). As shown in the schematic image, intensification occurs where LORs intersect resulting in reconstruction of regions of activity as they would occur in the source distribution. The intersecting lines make a star-like appearance which is more prominent when the source and detector

distance increase (Fig.1. 15 C-E). The star artifacts reduce image resolution, so a ramp filter is applied to projection data before they are backprojected to reduce star artifacts and improve image sharpening (Fig.1. 15 F).
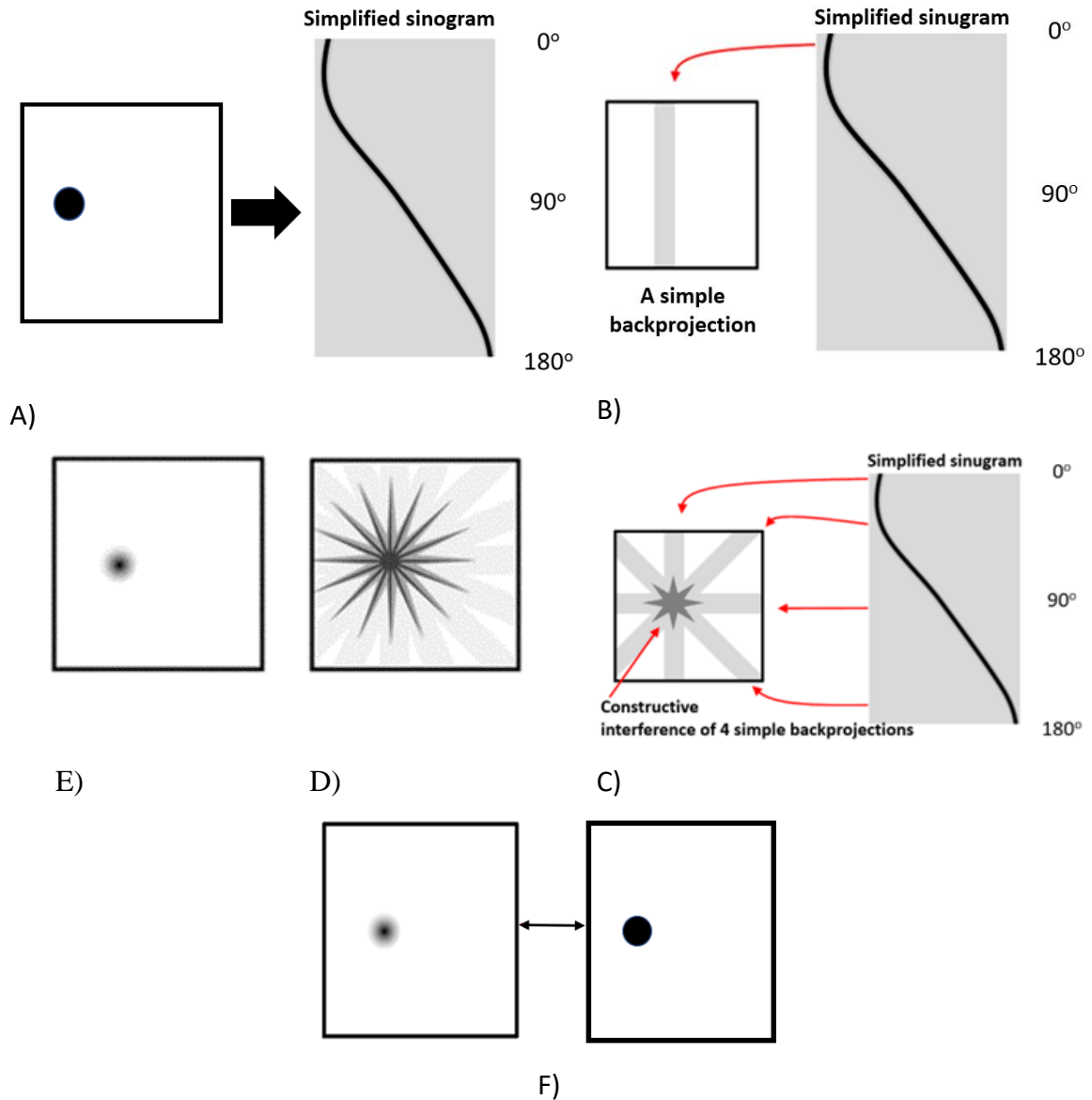
Figure1. 15 A-F Schematic representation of filtered backprojection image reconstruction. A) Simplified sinogram, B) A simplified backprojection, C) Interference of 4 backprojections, D) right and E) left demonstrate interference of 8 backprojections (star)

and 128 backprojections (blur) respectively and F) Ramp- filter application on projection before backprojected to compensate star/ blurriness.

The intensity of the intersecting lines changes with the distance of the detector from the patient. The ramp filter increases the noise and reduces the image quality; however, this FBP algorithm is fast and easy to use. A low-pass filter can be applied to the reconstruction to improve image quality and reduce noise. This filter reduces the high-frequency signal components from the image, such that noise is reduced at the expense of loss of image sharpness. Reduction of image sharpness causes some loss of image resolution.

1.11.3 Iterative Reconstruction (IR)

Iterative reconstruction, unlike FBP, is not an analytic algorithm. Instead, iterative reconstruction commences by guessing an initial distribution of activity, such as a uniform distribution or a simple object such as a disc. Projections are then determined based on the initial guessed distribution. These projections are then compared with the actual projection data by way of a "cost function". An "update function" then uses the output of the cost function to create a revised estimation of the activity distribution. Projection data from the new estimated activity distribution are again determined to create a new cost function and new update function. This process is successively repeated until the projection data derived from the estimated activity distribution is sufficiently close to the measured projection data. Each round of modification is referred to as an iteration. Fig. 1. 16 schematically demonstrates the IR algorithm.

Object　　　　Measured projected
data sinogram ρ(r,φ)

Forward
projection

Image estimate
f*(x,y)

Calculated
projection data
ρ(r,φ)

Compare
Converged?

Yes

No

Update image
estimate
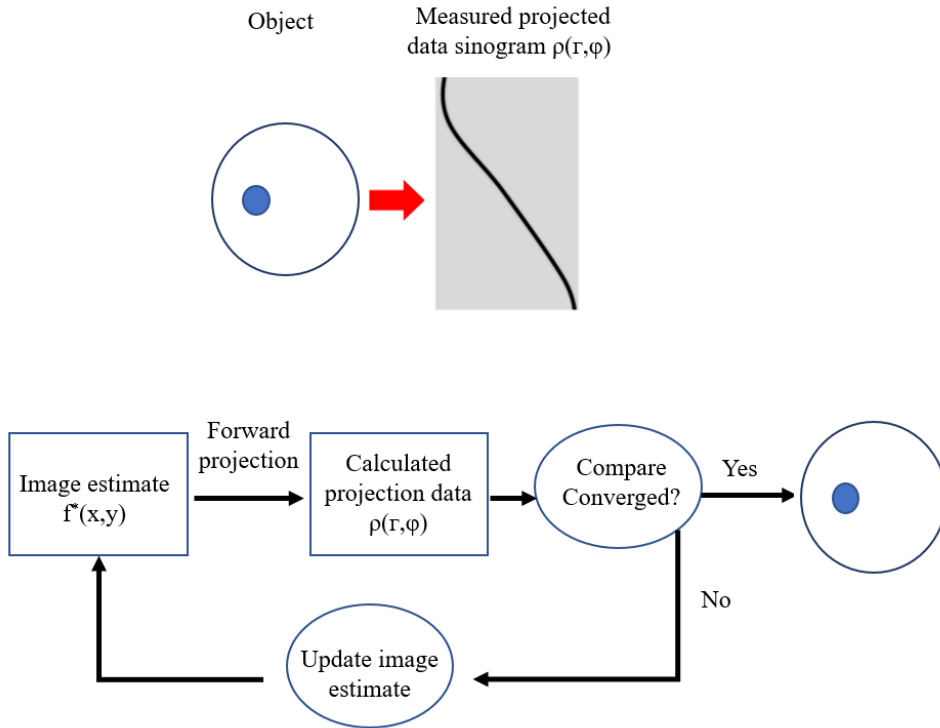
Figure1. 16 Illustration of the iterative reconstruction algorithm.

IR incorporated information about the voxel activity, system matrix, and probability that a photon emitted from a voxel in an object is detected in a bin on the detector. This algorithm incorporates the information of the intrinsic detector response and septal penetration of the collimators into the image analysis, which needs laborious computational efforts. This algorithm can handle source distance resolution loss and account for noise and attenuation better than FBP.

One iterative reconstruction algorithm is known as Maximum Likelihood Expectation Maximization (MLEM). This algorithm maximizes the likelihood function when the difference between calculated and measured projections becomes minimal, and the two come to an agreement.

1.12 Software Review

Nuclear cardiology software typically provides quantitative evaluation of left ventricular perfusion and function, including; 1) extent and severity of LV myocardial perfusion deficits, summed scores for stress and rest perfusion abnormalities, indices of reversibility of perfusion abnormalities, and total perfusion deficit (TPD), 2) LV function parameters include left ventricular ejection fraction (LVEF), LV end-systolic volume (ESV) and end-diastolic volume (EDV), 3) Myocardial wall motion, wall thickening, and dyssynchrony, 4) Transient ischemic dilation (TID) ratio, and LV eccentricity.

1.12.1 Gated Cardiac Imaging

Gated cardiac imaging is a mode of image acquisition which enables visualization of the moving heart throughout the cardiac cycle. The cardiac cycles on an ECG are divided into 8-16 bins, each called a frame, and ECG triggers the acquisition of each frame, when it occurs. The gated images are generated by successively displaying sequential ECG-designated-binned counts. A count refers to the signal created by an interaction between a gamma ray photon with the detector. In gated mode image acquisition, the counts are recorded from many cardiac cycles by placing a camera around the patient's chest. Each count becomes associated with a frame based on the time the count is registered by the camera in relation to the simultaneous bin position of the R-R cardiac cycle. Counts/cardiac images from every gated "frame" are summed up separately. Fig. 1. 17 schematically demonstrates gated mode image acquisition.
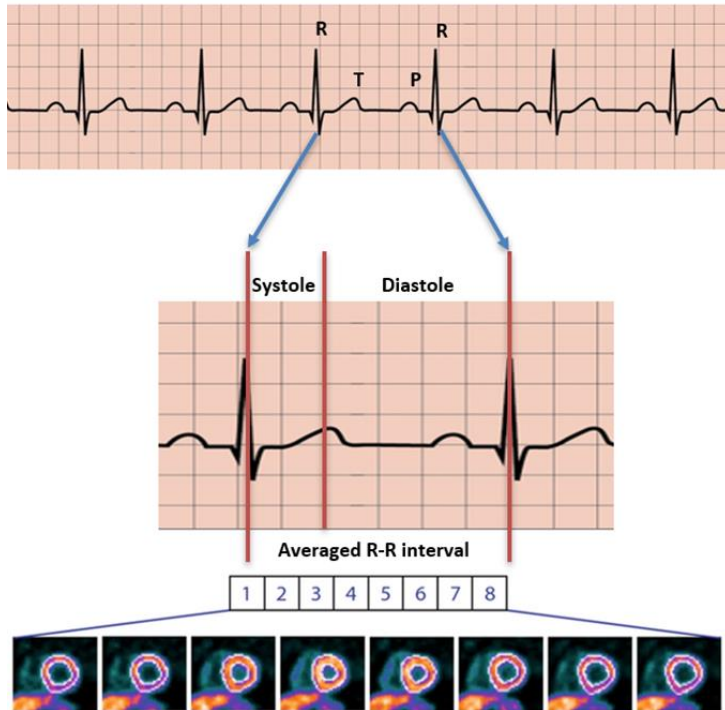
Figure1. 17 Represents gated cardiac image acquisition and binning of images in 8 bins from hundreds of heart cycles.

A moving depiction of the heart for an average cardiac cycle is generated by this process. Such images permit the calculation of functional parameters including left ventricular end-systolic volume (ESV), left ventricular end-diastolic volume (EDV), left ventricular ejection fraction (LVEF). Such images are also used for the evaluation of left ventricular wall motion and wall thickening.

Wall motion is not uniform in a normal heart, the cardiac apex exhibits greater motion than the basal segments, and the anterolateral and inferolateral segments exhibit greater motion than the anteroseptal and inferoseptal segments.

The summed motion score (SMS) denotes a semi-quantitative evaluation of left ventricular wall motion using a 17-segment model and is based on a 6-point scale for each segment Table 1.1.

Table 1. 1 Left ventricular wall motion score

Motion	Score
Normokinesis	0
Mild hypokinesis	1
Moderate hypokinesis	2
Severe hypokinesis	3
Akinesis	4
Dyskinesis	5

For the calculation of the SMS, the software compares the acquired data from each patient with a set of averaged respective values from a healthy population. The SMS demonstrates differences between the patient's wall motion scores and the normal database. It reflects the severity of left ventricular wall contractility abnormalities(34). The same approach is applied to left ventricular wall thickening which is instead based on a four-score scale Table 2.1

Table 1. 2 Wall thickness score

Wall thickness	score
Normal thickening	0
Mildly reduced	1
severely reduced	2
No wall thickening	3

1.12.2   Image Processing with Cedar-Sinai Quantitative Gated Software/ Quantitative Perfusion Software QGS/ QPS

Myocardial perfusion SPECT has been used in clinical settings since the 1990s. The technique and software have undergone continuous improvement over many years. In 1995 an automatic algorithm for quantitative measurement of left ventricular ejection fraction was developed by a group of scientists at Cedar-Sinai research institute(35) and Emory University(36). The efforts to improve software analysis continued in the following years, which resulted in the development of a new algorithm in 2000 by Germano et al., which has since been generally employed in the quantitation of myocardial perfusion SPECT imaging(37). The software packages were developed and validated with more diversity in the early 2000s(38)(39)(40).

 The Cedar-Sinai QGS/QPS software is among the most commonly utilized standard software applications utilized in practice and the software used for clinical image analysis in this study.

The heart is oriented obliquely in the thorax and is not aligned with the body's long axis. Therefore, the long axis of the left ventricle is not perpendicular to the long axis of the body. If image planes with horizontal long axis perpendicular to the long axis of the body rather that the heart were selected, such as in standard tomographic imaging for typical non-cardiac applications, part of the myocardium would be imaged with artifactual increased myocardial thickening obliquely, thereby resulting in image distortion(41). Cardiac tomographic images are first reconstructed as a set of transaxial images and then reoriented to display three sets of images perpendicular to the orientation of the heart in the thorax. The resulting images represent the standard display of MPI for clinical evaluation and interpretation. These planes are 1) short axis, 2) vertical long axis, and 3) horizontal long axis. These planes minimize image distortion and artifacts mentioned previously. (Fig.1. 18).

Vertical Long Axis   **Short Axis**   **Horizontal Long Axis**
VLA   **SA**   **HLA**
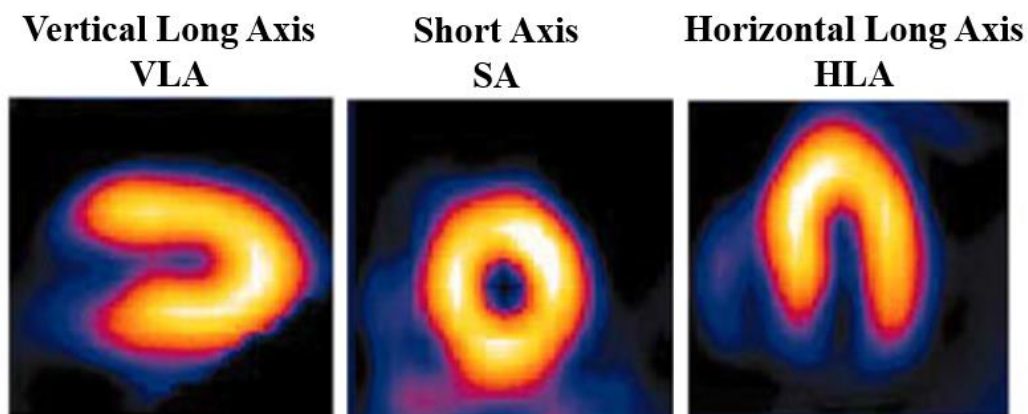
Figure1. 18 Demonstrates each cardiac axis created for SPECT-MPI.

The QPS/QGS software automatically recognizes the maximum counts in the myocardium's transaxial (short axis) section and uses this information for left ventricular segmentation (which refers to the separation of the left ventricle from the remainder of the image). It then employs an algorithm in which a 50% threshold profile is generated extending both inward and outward from the site of maximum counts in the middle of the myocardium to delineate both the endocardial and epicardial surfaces, which are used for left ventricular volume, wall motion profile, and ejection fraction measurements(35). A detailed automated segmentation algorithm for QPS/ QGS software describing steps in image processing for delineating myocardial thickness and identifying the endocardial and epicardial surface was described by Germano et al(35). This method is fully automated, thereby eliminating operator manipulation and operator-dependent errors. In this algorithm, segmentation starts with the reconstruction of short-axis images of the myocardium. The algorithm considers the maximal voxel count in each short-axis plane as the mid-myocardium. Then, it defines the center of the left ventricle (also called the center of the mass or COM) in the short-axis plane. From the COM, the software acquires a set of standard longitudinal and latitudinal equispaced sampling of myocardial perfusion data.

The software begins sampling every 10 degrees longitudinally (18 total profiles, each extending from the apex to the valve plane of the left ventricle) and latitudinally (36 profiles in total covering mediolateral plane surfaces) with overall 648 count profile of

myocardium to extract mid myocardial maximum count profile throughout the whole myocardium.

The software uses another count profile extending 20 mm inside and outside mid-myocardial counts to define the endocardial and epicardial surfaces and then measures the standard deviation SD of count profiles by fitting an asymmetric Gaussian to new count profiles inside and outside of the mid-myocardial count. Germano et al.(35) experimentally determined that 65% of SD inside can reliably define the endocardial contour. The software completes tomographic imaging of the left ventricle after delineating the endocardial and epicardial surfaces. Delineation of endocardial and epicardial left ventricular surfaces is crucial for the accurate evaluation of left ventricular volume, wall motion profile and ejection fraction (Fig. 1.19).

A)   B)   C)   D)
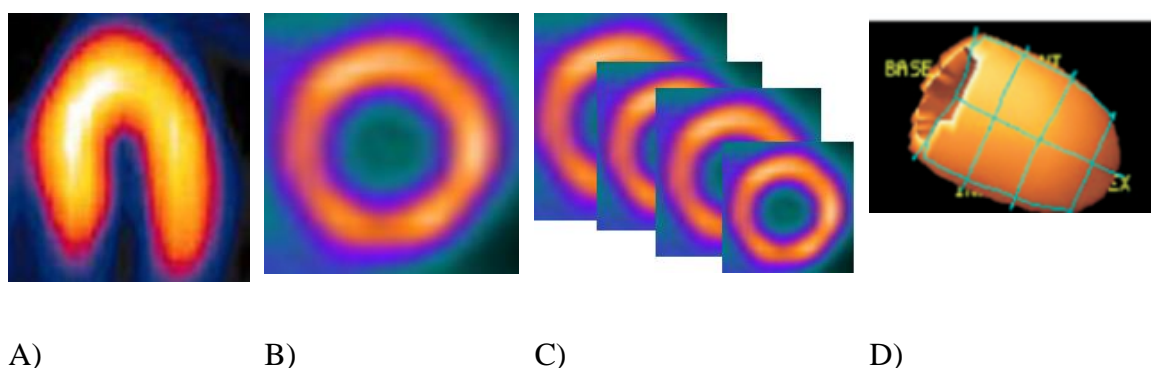
Figure1. 19 A) endocardial and epicardial surfaces recognized by the algorithm, B) sectional images created by the software, C) stacked on one another, and D) creation of a 3D image of the left ventricle.

As the quantification of myocardial perfusion images is relative in nature, image normalization is required. Normalization may be simply performed in relation to total myocardial counts. However, this can result in other problems, such as potential over-normalization of large perfusion defects, thereby reducing the apparent magnitude of such defects. Alternatively normalizing to maximum left ventricular counts at the site of a focal hot spot may artifactually give the appearance that the remainder of the myocardium is hypoperfused.

Another method of normalization is the 2-pass iterative method employed by Cedar Sinai software and has shown improved quantification accuracy(42). The limitation of relative perfusion imaging of SPECT MPI has been confirmed with PET MPI and absolute myocardial blood flow quantification, which has shown that SPECT MPI can underestimate the severity and extent of coronary artery disease(43).

Tomographic images provide a three-dimensional view of myocardial perfusion, which guides physicians to localize the abnormalities in different walls and planes. Another practical way of representing myocardial perfusion data for reviewing physicians is through a polar map or a bull's-eye image. This technique employs a two-dimensional representation of three-dimensional information derived from short-axis MPI slices. DePasquale first utilized this technique to display and quantify an entire study in a single functional image(44).

A polar map can be generated following the segmentation. First, a sector sampling of count statistics is obtained from the center of the LV cavity of the short-axis slices (12-15 slices). Each sector is 9 degrees, so the software acquires the count values of 40 sectors for each short-axis slice. Then, each sector's maximal count per pixel is identified and plotted in a circumferential profile. This process is repeated for all sectors in the slice and results in a ring profile to be incorporated into the polar map (with the profile being representative of maximal counts per pixel per angular location in a particular slice). This process is repeated for all slices in a short-axis plane to create multiple rings in the polar map, which ultimately results in a 2D representation of 3D images (Fig. 1. 20).
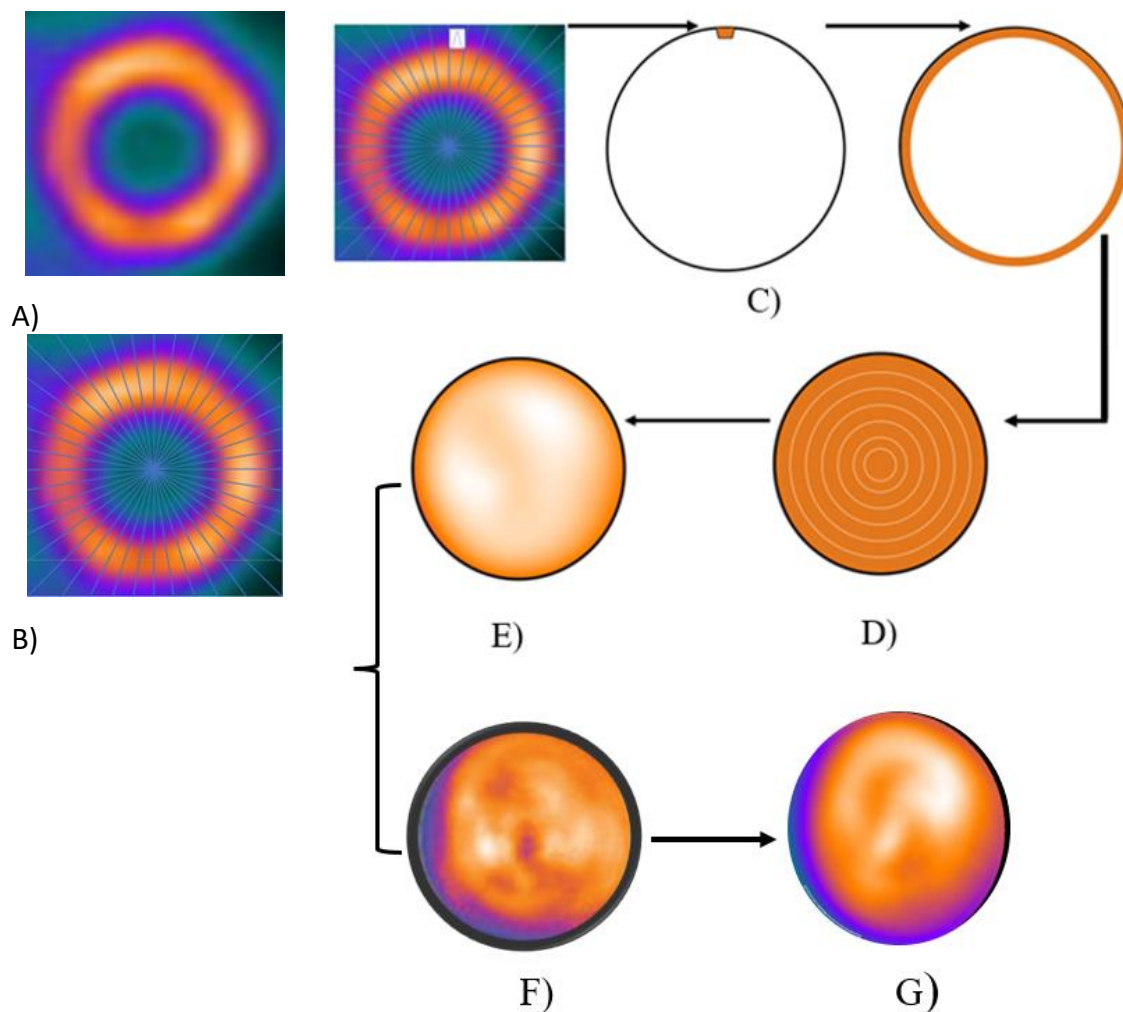
Figure1. 20 Polar map reconstruction. A) Short axis slice of the left ventricle; B) Sampling each short axis section with 40 sectors; C) Maximum counts per pixel of the sector is mapped onto a circle with the location on the circle depending on the location of the segment in the heart, with this process being repeated for all sectors in the slice; D) A drawing which includes many repetitions of step C for each short axis slice to create a map; E) A normalized real image of step D; F) Normalized image on step E undergoes a further quantification by comparison with an average normal database polar map, to create the patient quantified polar map which is used for evaluation of perfusion abnormalities G).

The polar map aims to represent myocardial perfusion information in a parametric way for standardized reporting and less inter-observer variability. Because of differences in body habitus between patients, physiological differences, various injected activity, and the

fraction of extracted counts by myocardium, a polar profile based on absolute counts of the LV myocardium could show variability between patient and even for the same patient with multiple MPI at different time points(42).

There have been different approaches for creating polar maps based on count profile per pixel(38)(39)(40). The Cedar Sinai QPS/QGS algorithm considers the average count in the sample from endocardial to epicardial along with the count profile by averaging 2-3 voxels. This method provides better noise characteristics for the sampled perfusion data than the maximal-count approach. In this method, the software calculated the 80th percentile of the maximum count in the patient image and subsequently normalized each parametric image to the 80th percentile to reduce artifacts related to presence of hot spots(37)(45). For example, normalization to total counts in the myocardium would over-normalize studies with large defects.

The normalization process quantitatively compares the perfusion data on a polar map to the polar map derived from a normal database acquired from patients with a low likelihood of CAD; the purpose of which is to provide a quantitative measure of perfusion abnormality.

To create a normal database, a group of 20-40 patients referred for MPI with a low likelihood (risk ≤5%) of having coronary artery disease based on age, sex, EST result, symptoms, and coronary artery disease risk factors are selected. Physicians review the images of these patients visually and disregard the images with any abnormality on the polar map. The application adds the normal images to the normal database(42). Figure 1. 21 schematically demonstrated normal database generation and the patient polar map quantification .
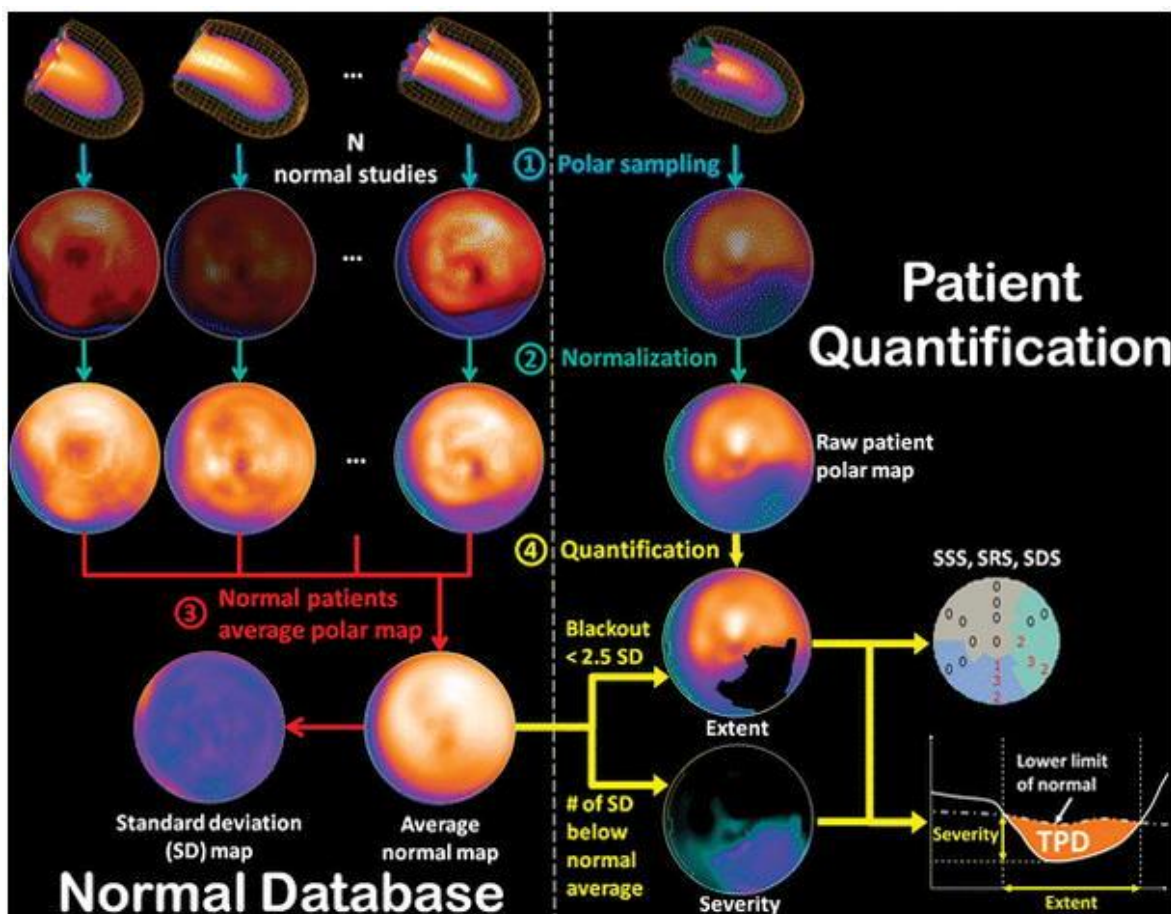
Figure1. 21 This figure demonstrates the normal database generation and patient quantification. 1. Polar sampling is used to discretize the patient perfusion information to a finite number of samples represented in a polar map. 2. A normalization step is required to allow a comparison among patients. 3.The normal patients' normalized polar maps are averaged to produce an average and standard deviation normal polar map, constituting the normal database or normal limits. 4. This database is used to compare against the diseased patient, allowing the generation of extent and severity polar maps, which will be used to compute the TPD and the summed scores (SSS, SRS and SDS).

TPD = total perfusion deficit, SSS = summed stress score, SRS = summed rest score, SDS = summed difference score.(Adopted from Mathieu Rubeaux et al(42). Normal Databases for the Relative Quantification of Myocardial Perfusion Current Cardiovascular Imaging. Springer Nature Jun 30, 2016 with permission).

Figure 1. 22 illustrates the position of myocardial walls and vascular territories within polar maps and17 and 20-segment models for polar maps.
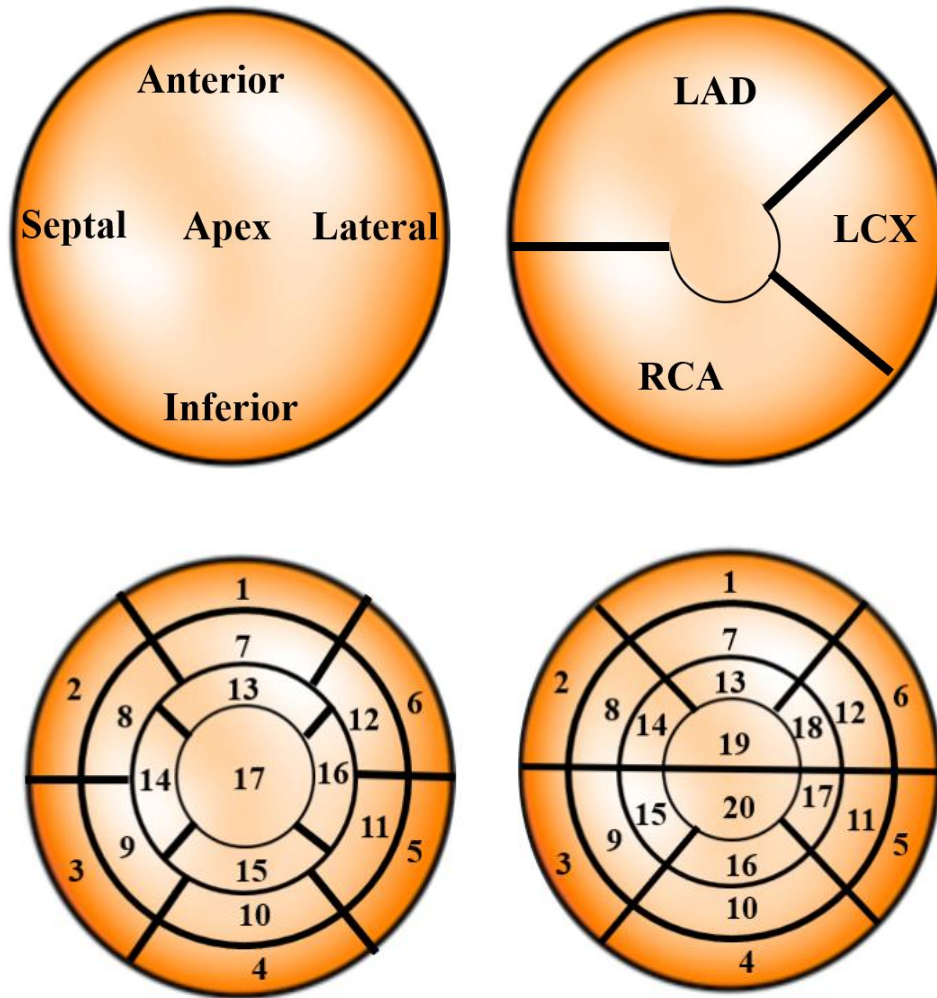
Figure1. 22 Upper left shows LV walls and apex. Upper right demonstrates vascular territories on a polar map, and the lower right and left demonstrate 17 and 20-segment polar map segmentation. LAD: Left anterior descending artery, RCA: Right coronary artery, LCX: Left circumflex artery.

The software uses different approaches to define lower normal limits in each segment; 1) absolute value 25% lower than the mean value of the normal database, 2) 2.5 SD below the

mean value of the normal database(46). Any segmental count value below this number of SDs is considered abnormal.

The normal database is specific for the camera, collimator, acquisition and reconstruction protocol utilized and differs for males and females(47). Indeed, due to differences between radiopharmaceuticals' biodistribution at stress and rest, the normal database is also radiopharmaceutical specific. Each software package has several such databases(42).

The algorithm in the software compares pixel by pixel the patient and normal database with respect to individual pixels in polar maps, with respect to segment and coronary artery territory; and the software defines abnormal segments. The software employs a 0-4 point grading scale to semi-quantify the perfusion deficit. The score definitions are as follows: 0 = normal counts, 1 = mild count reduction (not abnormal), 2 = moderate count reduction (abnormal), 3 = severely abnormal and 4 = no counts.

The QPS/QGS software usually creates two normalized polar maps after comparing the patient polar map to the normal database 1) the severity and 2) the extent of a perfusion deficit (blackout map).

The QPS/QGS software also creates the blackout map by setting the pixels of the patient to zero (or a black colour) when counts are below 2.5 SD compared to a normal database polar map.

1.12.3 Cedar Sinai QPS/QGS Software for Evaluation of Perfusion and Functional Abnormalities

As discussed earlier, the polar map is a convenient approach to evaluate myocardial perfusion abnormalities. It displays the radiopharmaceutical distribution in the myocardium in a 2D plane. The polar map is segmented based on the model suggested by American Heart Association into 17 segments. Normalized polar maps are generated for both rest and stress imaging.

The computer quantifies the extent of perfusion deficits as an area or percentage of the defect compared to the remaining part of the LV. The perfusion defect severity is a

parameter which is used to visually grade the magnitude of a perfusion defect in a polar plot Table 3.1.

Table 1. 3 A five-point scale for scoring myocardial perfusion polar maps

Normal perfusion	0
Minimal, mild impairment of perfusion	1
Moderate impairment of perfusion	2
Significant impairment of perfusion	3
No perfusion	4

A score of 1 or 2 indicates the segment retains approximately 100-80% or 80-60% of counts (respectively) in comparison to the regional maximum radiopharmaceutical accumulation; however, a score of 3 indicates a radiopharmaceutical activity between 40% -60%, while a score of 4 indicates radiopharmaceutical activity below 40% compared to area region with 100% activity.

The summed scores are generated by the software application for the purpose of global scoring of myocardial perfusion reduction and quantification of ischemia and infarct. Specifically, they are referred to as the Summed Stress Score (SSS), the Summed Rest Score (SRS), and the Summed Difference Score (SDS).

The SSS is the sum of the individual scores from the 17 segments of the polar map obtained during stress.

SSS of 0-3 is considered normal or minimal perfusion abnormality.

SSS of 4–8 indicates mild perfusion deficit.

SSS of 9–12 indicates moderate perfusion abnormality.

SSS 13 or more demonstrates severe perfusion abnormalities.

The number of segments with an abnormality is also essential.

Involvement of 1-2 segments (less than 10%) is considered small, 3 and 4 segments is considered moderate, and five or more segments is considered a severe amount of perfusion reduction.

SDS is the difference between the SSS and the SRS (SDS = SSS − SRS). SDS accounts for the degree of reversible perfusion deficit (inducible hypoperfusion).

The SDS score 0-1 is considered no ischemia.

SDS 2-4 indicates mild ischemia,

SDS 5-6 indicates moderate ischemia, and

SDS 7 and more indicates severe ischemia.

The software can generate percentages for summed stress, rest, and difference scores and denote them as SS%, SR%, and SD%. To generate this percentage, SSS and SRS are divided by the product of the number of segments in the polar map multiplied by 4 (score of maximum perfusion abnormality). For example, if the polar map has 20 segments, the score is divided by (20x4=80), and if it has 17 segments divided by (4 x 17=68). The product of the previous step is then multiplied by 100.

For example, if the SSS is 10 in a 17-segment polar map, the SS% would be (10/ 68) x 100=14.7%.

The SS% values up to 4% indicate normal perfusion,

5–9% is a mild abnormality,

10–13% is moderate, and

14% or more is severe perfusion abnormality.

An SD% greater than 10-13% tends to result in patient referral for coronary artery angiography with potential revascularization; however, patients with SD% less than 10% are often managed with lifestyle changes and medication optimization.

Total Perfusion Deficit (TPD) is another useful measurement for quantifying perfusion deficits. This score is calculated based on both the extent and severity of ischemia. As shown in Fig. 1.23, the total perfusion deficit quantifies the extent and severity of perfusion reduction encompassing all myocardial segments. The TPD is first calculated as circular activity profiles of the myocardium at distinct radii within the polar plot. The individual TPD values for all such polar plot radii are then added together to generate the overall total perfusion deficit.
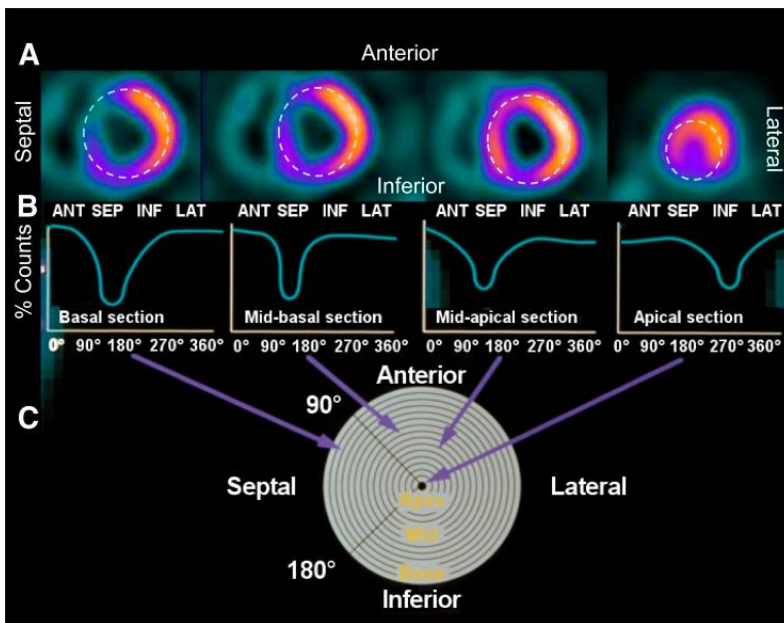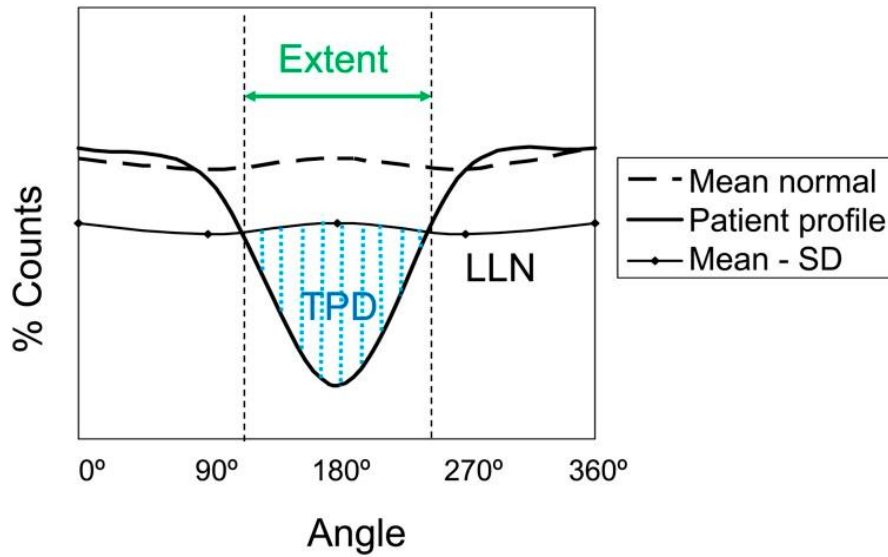
Figure1. 23 Top) method for polar map representation of LV myocardial perfusion distribution. (A) Circumferential count profiles are extracted from each short-axis slice from apex to base, depicted here as dashed circles (only 4 shown). (B) Circumferential profiles extracted from each LV short-axis slice plotted as normalized percentage counts extracted vs. angle around short axis for patient with hypoperfused septum. (C) Mapping of individual count profiles into rings, creating polar map. Bottom) methods for detecting and measuring the degree of hypoperfusion. The plot depicts how circumferential count profile is tested for abnormality. Patient's normalized count profile (solid line) is compared against lower limit of normal (LLN) profile calculated as mean normal count response profile minus set number of SDs (usually 2–2.5). The extent of deficit is given by angular range of count profile falling below LLN. Severity of deficit may be measured as sum of SD below mean normal profile for all abnormal angular samples. Total perfusion deficit (TPD) is marker of deficit severity similar to SSS but measured for each sampled voxel, where each sample is scored from 0 (normal) to 4 (no uptake). Normal polar map generates TPD of 0, and maximally abnormal polar map (no myocardial uptake) would result in TPD of 100% Image adopted from Garcia E et al(48).

Normal-range values of TPD are less than 5%,

TPD of 5–9% indicates a slight abnormality,

TPD between 10–14% indicates a moderate abnormality and

TPD of 15% or more denotes significant abnormality(49).

Table 4.1 summarizes the definition of various scores generated by computer.

Table 1. 4 Definition of computer-generated perfusion scores

SSS	SDS	TPD (%)	Result
0-3	0-1	< 5	Normal/minimally abnormal
4-8	2-4	5-9	Mildly abnormal
9-13	5-7	10-14	Moderately abnormal
>13	>8	>14	Significantly abnormal
SSS: Summed stress score, SDS: Summed difference score, TPD: Total perfusion deficit.			

The image in Fig.1. 24 is a screen display of perfusion images and the computer-generated score by the QPS application for clinical interpretation.

The QGS application provides information related to functional parameters and wall motion. Fig.1. 25 demonstrates a screen display of the QGS images and parameters.
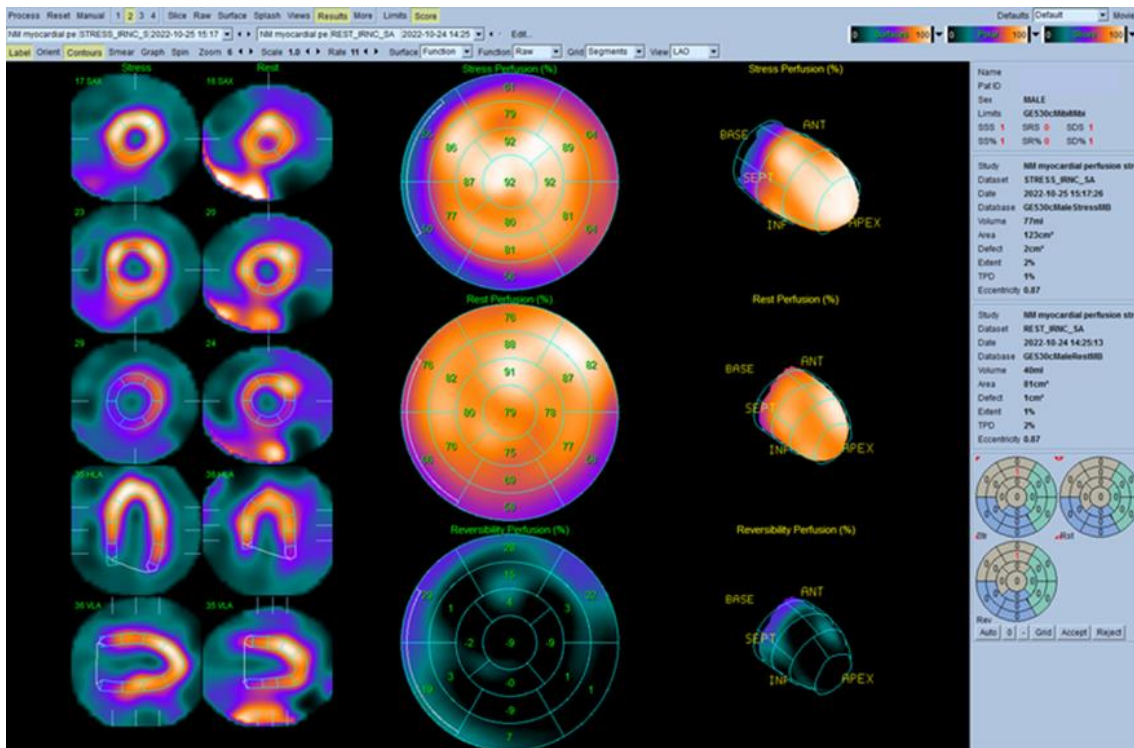
Figure1. 24 Polar maps with stress perfusion image (top) and rest perfusion image (bottom) of a non-diseased participant in a 17-segment polar map layout. The right pane provides parametric scores generated by the QPS application.
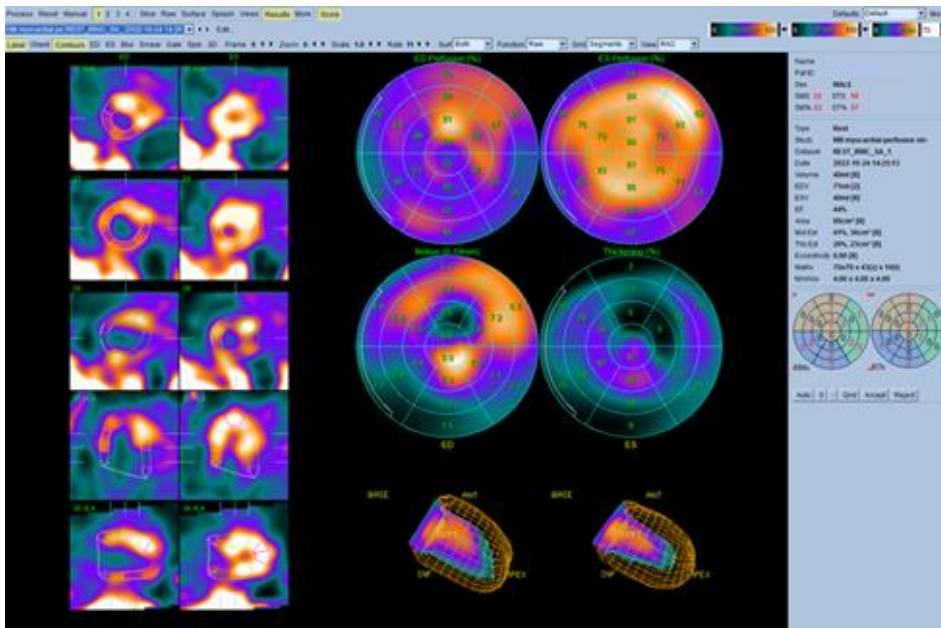
A)
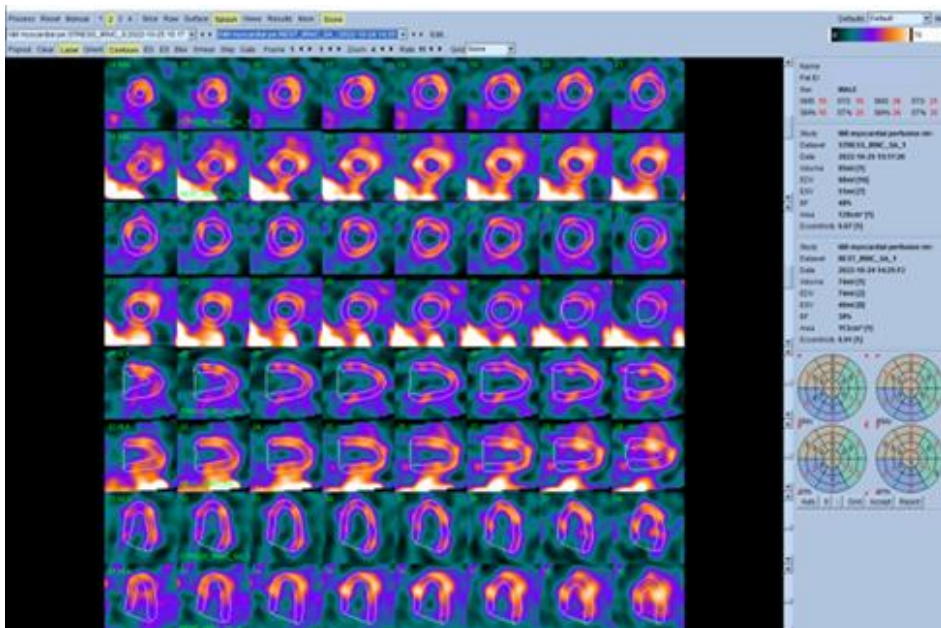
B)

Figure1. 25 Samples of gated images by QGS. Wall thickness and motion are mapped onto a 20-segment polar map (Top A). Sectional gated images with wall thickness and motion scores are shown in (Bottom B).

The image below is a magnified view of the computer-generated parametric score panes shown in the preceding images (Fig. 1. 26). The perfusion image parameters are on the left, and the gated image parameters are on the right side of the figure.
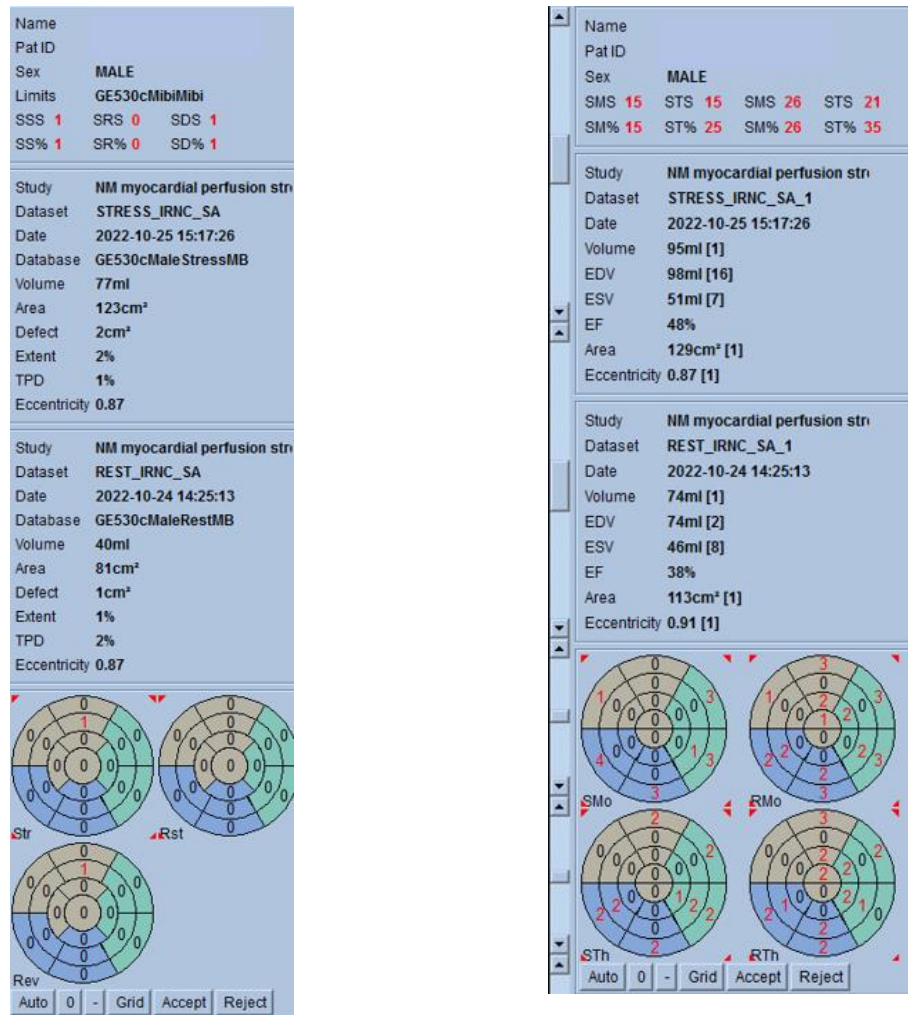
Figure1. 26 Left) Perfusion score parameters from a normal study; SRS=0, SSS=1, SDS=1, TPD 2% at rest, and 1% on stress images (polar maps with overlying scores at the bottom of the left pane). Right) Gated parameters from an abnormal (gated) study. The wall motion and thickness are non-uniform. There are more abnormal segments in the inferior part of the heart (polar maps with overlying segmental scores at the bottom of the right pane).

1.13 Summary of Introduction

In summary, MPI is a commonly employed technique for investigating IHD. Recent engineering advancements, particularly with high-sensitivity DCC with CZT detectors, have successfully halved the radioactive administered activity for patients and significantly reduced image acquisition time compared to traditional SPECT gamma cameras. However, despite these improvements, the current DCC still poses challenges with prolonged imaging time, leading to the risk of undesired motion artifacts.

The primary aim of this thesis is to leverage software and engineering advancements to simulate further reductions in image acquisition time before reaching a point where image quality becomes impractical for interpretation. This investigation utilizes standard-of-care clinical images from a group of consenting patients. The simulation of image acquisition time reduction is performed post-processing, employing software capable of selectively removing certain image information to mimic the effect of reduced imaging time. This approach ensures that the quality of standard-of-care images obtained from patients is not compromised.

The subsequent two chapters explore the study's design, sample size, image acquisition, and the multi-step post-processing procedure simulating imaging time reduction. Additionally, the chapters cover image analyses, results, a comprehensive discussion of findings, and a conclusion that emphasizes the significance of the study's results. Limitations of the study are acknowledged, and future avenues for research are highlighted.

Chapter 2

2   Thesis Structure

Ischemic heart disease is prevalent among the adult population, leading to a significant number of fatalities and morbidities, thereby imposing a substantial financial burden on the healthcare system. Various efforts have been made to enhance the efficiency of imaging tools, such as reducing radiation doses to patients and expediting the image acquisition process. The introduction of the new DCC has revolutionized this imaging study, addressing the aforementioned goals. However, there is still room for improvement in these aspects. Chapter 2 is dedicated to providing an in-depth exploration of the background and current practices, research questions, objectives, methods, study design, image reconstruction, statistical analysis, results, and discussions related to the study.

2.1 Background and Literature Review

Myocardial perfusion imaging (MPI) is one of the most commonly-utilized modalities for the evaluation of coronary artery disease. There are typically two types of cameras used for SPECT MPI, with different engineering, designs A) conventional SPECT CT Anger camera utilizing rotating dual-headed NAI scintillation detectors or B) new DCC, using stationary CZT detectors with multiple pinhole collimators. This new DCC has improved sensitivity by 5-10 folds, compared with the traditional Anger camera, making it feasible to acquire images in shorter time durations and with lower administered activity than for conventional SPECT gamma cameras. New iterative reconstruction algorithm, which tend to generate better quality images, is usually employed with modern SPECT cameras. Advancements in computer hardware technology have provided faster processors and more computer memory, thereby enabling list mode acquisition of imaging data. which is a feature of conventional and DCC SPECT cameras. List mode image acquisition provides the capability to re-bin acquired image data within shorter image time frames to simulate shorter overall image acquisition time intervals. By reconstructing the simulated shorter image data, we can create a simulated time-reduced polar map and simulated time-reduced computer-generated functional parameters.

The count statistics of a gamma camera in part depend on the administered activity and image acquisition time. Simulating time reduction reduces the count statistics similar to that of a reduced-injection of radiopharmaceutical. Several studies investigated the potential of dose-reduction strategies based on this principle(47)(50)(51)(52)(53)(54). A study by Lecchi et al(50). assumed that a shorter acquisition time impacts the count statistics similar to that of lower injected activity. They implemented three full-time, half-time, and quarter-time scans on 80 patients and showed that reducing the imaging time to 25% of the non-time-reduced MPI (time reduction to 25% of MPI reference) negatively impacted the image quantification in patients with high BMI. They suggested that reducing the injected radiopharmaceutical activity to 25% of the reference for normal-weight patients is reasonable. They suggested an activity reduction of 50% for overweight and obese patients.

2.2 Current Practice in MPI

In current practice, it is possible to perform MPI with almost half the administered activity of the radiopharmaceutical compared to a conventional SPECT camera due to the increased sensitivity of the dedicated cardiac camera. Many nuclear cardiology labs perform MPI as a two-day rest and stress study. For rest MPI, the patient receives an intravenous radiopharmaceutical injection between 111-370 MBq based on BMI (instead of 300- 1110 MBq used in conventional SPECT imaging), waits for 45-60 minutes in a waiting room, and undergoes image acquisition for 10 minutes under a DCC. The process for the stress study begins with a slow intravenous injection of a vasodilator drug called dipyridamole for a duration of four minutes. This drug causes coronary artery vasodilation and increases coronary blood flow 4-5-fold compared to baseline. Three-minutes after the completion of dipyridamole injection and at peak vasodilation, the patient receives an intravenous radiopharmaceutical injection similar to the rest study (111-370 MBq). The vasodilator agent is typically inactivated approximately 10 minutes after the start of the stress test. The patient's blood pressure, heart rate and cardiac rhythm/ECG are monitored throughout the stress procedure. At the end of the test, the patient returns to the waiting room and stays for 30-45 minutes. The patient then undergoes stress image acquisition for approximately 8 minutes under the DCC.

Alternatively, exercise stress can be performed instead of chemical/vasodilation stress. Frequently, treadmill exercise is undertaken if the patient is able to effectively do so. In some cases combined protocols are employed whereby exercise stress is used to supplement vasodilator stress, e.g. combined vasodilator and cycle exercise.

The duration of the stress image acquisition is slightly shorter than the duration of the rest image acquisition due to increased blood flow to the heart during stress Increased myocardial blood flow which occurs for radiopharmaceutical localization during stress as compared to rest also usually results in greater myocardial radiopharmaceutical deposition at stress compared to rest. Consequently, slightly less image time is necessary to acquire adequate stress images than for rest images. After image acquisition, a dedicated application is run on the camera's workstation utilizing the raw image data. The application reconstructs tomographic images of the left ventricle in various planes, including transaxial, horizontal long axis, short axis, and vertical long axis or HLA, SA, and VLA. These orientations are standard planes used in myocardial perfusion imaging.

The images can be further modified by using a CT attenuation map to create an attenuation-corrected image data set. For this study, patients underwent a low-dose CT scan derived from a separate SPECT CT camera. This low-dose CT scan provided the attenuation map used for attenuation correction of DCC-acquired images.

The software application reconstructs non-AC and AC datasets both for rest imaging and for stress imaging. The rest and stress images provide a flow-dependent distribution of the radiopharmaceutical within the myocardium. Comparing the two sets of images allows for the detection of "resting" myocardial perfusion defects which are present on both rest and stress images or so-called reversible perfusion defects which are visualized on stress images but not present on rest images. Because the heart is a moving object, the location of the heart changes during each heartbeat. The cardiac cycle represents the changes which occur in the heart during one heartbeat. The cardiac cycle is repeated with every subsequent heartbeat, Gated image acquisition allows for determination of the temporal changes in the myocardium which occur during the cardiac cycle. To acquire gated mode images, ECG electrodes are placed on the patient's chest wall. The R-R interval on the ECG, which

defines one beat of the cardiac cycle, can be determined for every heartbeat. Each R-R interval or cardiac cycle is subdivided into 16 equal time bins. Each time bin is associated with its corresponding temporal myocardial image. Such that 16 images are generated for each cardiac beat. The images corresponding to bin 1 for multiple cardiac cycles is summed, as are the images corresponding to bin 2, bin 3 and all other bins for the cardiac cycle. The time duration of each bin is dependent on the heart rate. As an example: If the patient's heart rate is 60 beats per minute, each cardiac cycle will be 1 second. To acquire 16 bins per cardiac cycle, the time for each bin will be 1/16th second or 62.5 milliseconds. Because the myocardial location changes during the heart cycle, the x and y coordinates of the time-stamped events cyclically change during the heart cycle. The image reconstruction algorithm uses changes in cardiac conformation to evaluate myocardial function, including left ventricular volume and ejection fraction. Fig.2.1 demonstrates a schematic representation of our center's two-day rest and stress MPI protocol.
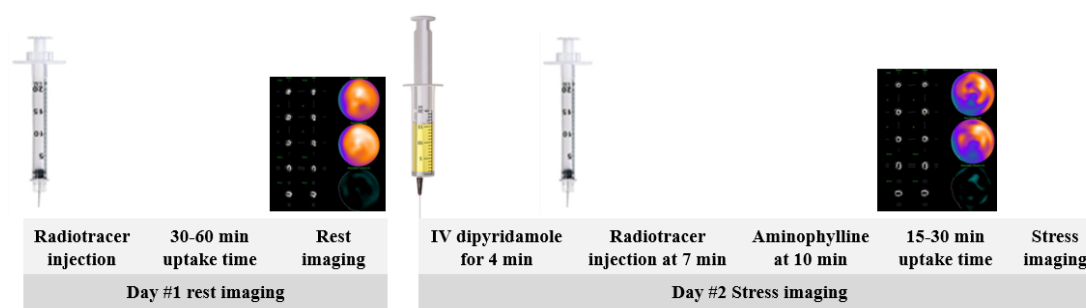
Figure 2. 1 Demonstrates the sequence of injection and imaging in a two-day rest and stress SPECT MPI protocol.

Time reduction can improve patient comfort during the MPI as well as increase the throughput of the nuclear cardiology lab. Image distortion can occur with patient movement. Image time reduction reduces the chance of patient movement during the study, preventing motion-related image distortion.

2.3 Research Question and Objective and Methods

The number of counts recorded by radioactive detectors in part defines image quality. The number of counts increases proportionally by 1) delivering more radiopharmaceuticals to

the body or 2) increasing the time that the patient remains under a gamma camera during image acquisition. Both time and administered activity can be interchangeably increased and decreased to create an image with the similar count statistics and image quality.

Patient radiation dose reduction is an important consideration in nuclear medicine and when imaging with ionizing radiation in general. There has been an assumption that administered activity reduction results in a proportional decrease of detected events by the same factor. This assumption is supported by data pertaining to the relationship between injected activity and image acquisition time as described by Herzog et.al(30). In this study, it was observed that as the injected activity was reduced, the image acquisition time was extended linearly to compensate for count loss associated with decreased activity. This adjustment aimed to maintain a constant number of counts in the resulting image. However, it overlooked the fact that reducing the injected activity may still introduce the potential confounding factor of patient motion during extended image acquisition periods.

The impact of dose reduction on image quality was evaluated through simulating dose reduction on PET imaging. Gatidis et al. implemented this idea using list mode data acquired from PET imaging in vitro and simulated administered PET radioactivity reduction with retrospective under-sampling of list-mode data(51).

There is the possibility of reducing administered activity while maintaining image quality on DCC with high sensitivity detectors. For example, a new DCC with a 10-fold increase in sensitivity can provide an image with a half administered activity while maintaining a 5-fold increase in sensitivity for equal imaging times(25).
There have been efforts to reduce administered activity on MPI with conventional SPECT/CT systems using various image reconstruction algorithms. Pretorius et al performed a human observer study and confirmed in a clinical model that iterative reconstruction with OSEM at 25% of the total administered activity demonstrated similar results to a filtered back-projection (FBP) algorithm with a full administered activity for depicting a cardiac perfusion defect on MPI(52).

With a high-sensitivity camera and improved reconstruction algorithm, we should be able to reduce imaging time or administered activity to a greater extent than that used in current

practice. However, a simulation study to evaluate the impact of count reduction on image quality and image interpretability before implementing this protocol in clinical practice is required to avoid inadvertent degradation of image quality. New software for SPECT reconstruction and use of the DCC with improved SPECT image quality has resulted in shorter image acquisition times since the new cardiac camera emerged, which is convenient for patients.

The impact of dose reduction on image quality was evaluated through simulating dose reduction on PET imaging. Gatidis et al. implemented this idea using list mode data acquired from PET imaging in vitro and simulated administered PET radioactivity reduction with retrospective under-sampling of list-mode data(51). List-mode data can be randomly under-sampled to simulate dose reduction. Additionally, imaging time reduction can be simulated by selectively removing counts recorded during a portion of the image acquisition time from the list-mode data. We used the latter methodology for this study.

The objective of this work is to determine the extent to which time can be reduced before significantly compromising the diagnostic accuracy of MPI.

2.4 Study Design

Myocardial perfusion imaging was investigated in this work utilizing pharmacologic stress. \Individuals referred for myocardial perfusion imaging were invited to participate in the study. A registered nurse working in nuclear cardiology interviewed the patients. Clinical information including the reason for referral, relevant clinical documents, past medical and drug histories, and weight and height were obtained. The inclusion criteria were: adults between the ages of 18-85 years 1) for the evaluation of CAD, 2) risk assessment of coronary artery disease without ischemic equivalent, 3) risk assessment before non-cardiac surgery without active heart disease, 4) risk assessment post-revascularization, 5) patients with abnormal baseline ECG, 6) risk stratification for patients who had myocardial infarction but were stable to undergo MPI and 7) patient with an abnormal EST. Exclusion criteria: 1) patients who had an allergy to vasodilator drugs or had severe asthma/bronchospastic lung disease, 2) pregnant women, 3) low systolic blood pressure less than 90 mmHg, 4) uncontrolled high systolic blood pressure greater than 200 mmHg,

5) high degree heart block (grade II and III) and not on a pacemaker, 6) unstable angina or acute coronary symptoms at the time of the study, or acute MI within four days before the study, 7) uncontrolled tachyarrhythmias and, 8) patients who consumed caffeine within 12 hours of the study.

After screening for patient eligibility, a physician (CO-PI in this study) interviewed the potential candidate to include in this study. All patients who decided to participate read the research protocol describing MPI, its advantages and disadvantages, detailed research project information and signed the consent form.

2.4.1 Study Sample Size

We included 26 patients in this study after consenting to participate. In this project, we used their myocardial perfusion imaging raw data and original non-time-reduced rest and stress images with the standard protocol to 1) simulate and reconstruct time-reduced images and to 2) compare the time-reduced images with the original series of images.

2.4.2 Study Protocol

Day one was the Rest study. A nuclear medicine technologist inserted an IV line in one of the antecubital veins.

Rest protocol:
1. injecting of the radiopharmaceutical (99m-Tc sestamibi) as per our departmental protocol with a administered activity ranging from 111-278 MBq in our cohort,
2. waiting for 45- 60 minutes in a waiting room,
3. acquiring a low-dose CT scan of the heart to create an attenuation map to be used for attenuation correction,
4. acquiring myocardial perfusion imaging under a DNM 530 DCC for 10 minutes,
5. reconstructing images by technologists and performing quality control and
6. discharging patients after fulfilling image quality controls.

Day two was the Stress study. Patient preparation had more steps, including changing clothes and putting on a gown, setting up an IV line in an antecubital vein, placing the patient on a

bed, and setting up the heart monitoring and blood pressure monitoring devices by nuclear medicine technologists.

Stress protocol: A 10-minute stress protocol starts with

1. slow injection of vasodilator drug (Dipyridamole) with a dose of 0.56 mg/kg over 4-minute,

2. during injection, if the participants were able to do cycling, encouraged to do so while they were on the bed,

3. injecting the radiopharmaceutical with an administered activity similar to rest protocol ranging from 111-278 MBq in our cohort as per our departmental procedure. The injection of radiopharmaceutical started three-minutes after the injection of the vasodilator drug was completed (7 minutes after starting the vasodilator drug).

4. injecting an antidote of dipyridamole (aminophylline) at a dose-ranging between 100-250 mg at a 10-minute time point to reverse the effects of dipyridamole,

5. continuous monitoring of heart rate (HR), blood pressure (BP) and ECG throughout 10 minutes of stress and 2 minutes into recovery (overall 12 minutes),

6. waiting for 30-45 minutes in a waiting room,

7. acquiring myocardial perfusion imaging under a DNM 530 DCC for 8 minutes and

8. reconstructing images by technologists and performing quality control and

9. discharging patients after fulfilling image quality controls.

Fig.2. 2 Illustrated the flow chart of the study.

Flowchart of the study

Patients are referred for MPI

|

Interview and history taking

|

Consenting to include in the study

|

Day #1 Rest protocol

|

Patient preparation for the study
(Blood pressure, pulse, height and weight, set up an IV line)

|

Radiopharmaceutical (99m-Tc Sestamibi) injection->Waiting for 45- 60 minute ->Low dose CT scan of the heart for attenuation map ->Image acquisition with a DDC for 10 minutes

|

Image reconstruction and quality control by technologist and discharge patient

|

Day#2 Stress protocol with vasodilator drug

|

Patient preparation
(Supine/semi supine on a bed, set up an IV, heart and blood pressure monitoring throughout stress and 2 minutes recovery)

|

Injection of vasodilator drug (Dipyridamole) slowly over 4-minute as per standard-of-care protocol

|

Waiting 3 minute after injection (7 minute after starting vasodilator drug)

|

Radiopharmaceutical injection

|

Aminophylline injection at 10 minutes and monitoring for 2 more minutes

|

Waiting for 30-45 minutes

|

Image acquisition with the same DDC as rest for 8 minutes

|

Image reconstruction and quality control by technologist and discharge patient

|

Sending images for clinical interpretation by physician

|

Post-processing raw data and image manipulation
Reframing raw data with incremental time reduction from 100% to 10% and creating new time-reduced cardiac SPECT and computer-generated parameters

|

Data analysis by
1-Evaluation of perfusion by two reviewers blindly and 2- recording functional parameters of time reduced and non time-reduced data

Figure 2. 2 The flowcharts of the study.

2.5 Image Reconstruction and Post-processing

The imaging device in this study was an NM 530 GE CZT camera, and the software employed for image reconstruction, creating polar maps and generating image-derived scores for both diagnostic images and simulated time-reduced images was Cedar Sinai QPS/QGS with Myoview. The software utilized to remove counts from the list-mode data, simulating time-reduced dataset intended for use by Cedar Sinai QPS/QGS for image reconstruction, was the Lister application.

The QPS/ QGS software on the camera workstation regenerates a series of standard reformatted images from the raw data in short axis, horizontal and vertical long axes, and creates polar maps (also called a Bull's eye plot). The polar maps provide a visual representation of normal or abnormal perfusion distinct from the reformatted 3-D slices. The QPS polar maps display information pertaining to radiopharmaceutical distribution throughout the myocardium, which helps evaluate perfusion abnormalities. The QGS package provides functional parameters of the left ventricular function, and the Myoview package provides additional information regarding count distribution in the polar map and a ratio of left ventricular volume at rest and stress, an index for detecting significant stress-induced perfusion abnormalities.

Important image-derived functional parameters, which are summarized in Table 2.1, include left ventricular ejection fraction (LVEF), end-diastolic volume (EDV), end-systolic volume (ESV), information of wall thickening, wall motion. Perfusion-related parameters include total perfusion deficits (TPD), summed rest score (SRS), summed stress score (SSS), summed difference score (SDS) and transient ischemic dilation index (TID) which acquired from non-gated images.

Table 2. 1 Perfusion and gated parameters and count statistics used in this study.

QPS parameters	QGS parameters	Myoview parameters
Summed Rest score (SRS) Summed Stress Score (SSS) Summed Difference Score (SDS) Total perfusion deficit (TPD)	End Diastolic Volume (EDV) End Systolic Volume (ESV) Ejection Fraction (EF)	Polar map count statistics: Total counts Maximum counts Average counts Count standard deviation Number of pixels in the polar map Transient ischemic dilation (TID)

The scores of perfusion deficits provided quantification of perfusion deficits and aid in determining the percentage and severity of perfusion defects. Gated image acquisition also enables software determination of ejection fraction (EF), left ventricular end-systolic volume (LVESV) and left ventricular end-diastolic volume (LVEDV).

After the standard non-time reduced images were reconstructed, the raw data were used for post-processing to simulate time reduction. The raw data was acquired in list mode for this study. List mode data acquisition, also called event-by-event data collecting, is a method of data acquisition in which every detected event has its own location parameters in the line of response (LOR) recorded in addition to recording of the time of the event. Because of the considerable amount of stored information associated with this type of data collection, it requires laborious intensive computational work and a large amount of computer memory to process the data. On the other hand, list mode enables precise manipulation of the image

data. In this study, data of varying lengths of time are removed from the end of the original non-time reduced data set. Simulated time-reduced images are generated by reconstructing the manipulated file containing truncated data from the end of the acquisition (52)(54).

The Lister application was utilized for reframing the raw data for this study. Multistep post-processing time reduction is achieved by incrementally reducing 10%-time intervals from the original datasets for rest and stress studies by the Lister application. Then, images are reconstructed from these time-reduced datasets with the QPS/QGS software. New sectional images, polar maps, gated images, and QPS/QGS parameters are generated for each set of new time-reduced images.

The steps on the workstation were as follows:

1. Select raw data of rest/stress tomographic data.
2. Select raw data of gated rest/stress tomographic data.
3. Run Lister software setting 90 (keeps 90% of the time of original data).
4. Two sets of reframed time-reduced data (rest and stress parts of the study) are created and saved under reframed 90.
5. Select these two sets of reframed data and run QPS/QGS software.
6. Sectional images and polar maps are created with computer-generated scores, and parameters are created. These images are saved as SPECT 90 for rest and stress images separately.
7. Steps A to E were repeated eight times to incrementally reduce 10% of the time by running Lister with setting 80, 70, ...,10 (keep the first 80, 70, ...,10% of the data with respect to event time respectively).

2.5.1 Lister Application

The List-mode data acquisition is an event-by-event count recording mode. This application allows for editing the lists of recorded data, creating revised lists with different time lengths, and reconstructing various fractions of acquired counts to simulate reduced imaging time. This too can be conceived to mimic the reduction of administered activity, so it can potentially serve to simulate dose reduction without impacting the patient's non time-

reduced diagnostic images(54). Lister software was employed to reframe the image by incrementally removing 10% of imaging time from the end of the recorded list. Nine lists of rest and stress imaging raw data for each patient with an imaging time ranging from 10%-90% compared to the original non-time-reduced image data were created. Figure 2. 3 represents the incremental time reduction of a dataset. Then, each set of time-reduced rest and stress images was reconstructed with QPS/QGS software and polar maps were created in addition to perfusion scores and functional parametric data for comparison with the original non-time-reduced images of the same patient.
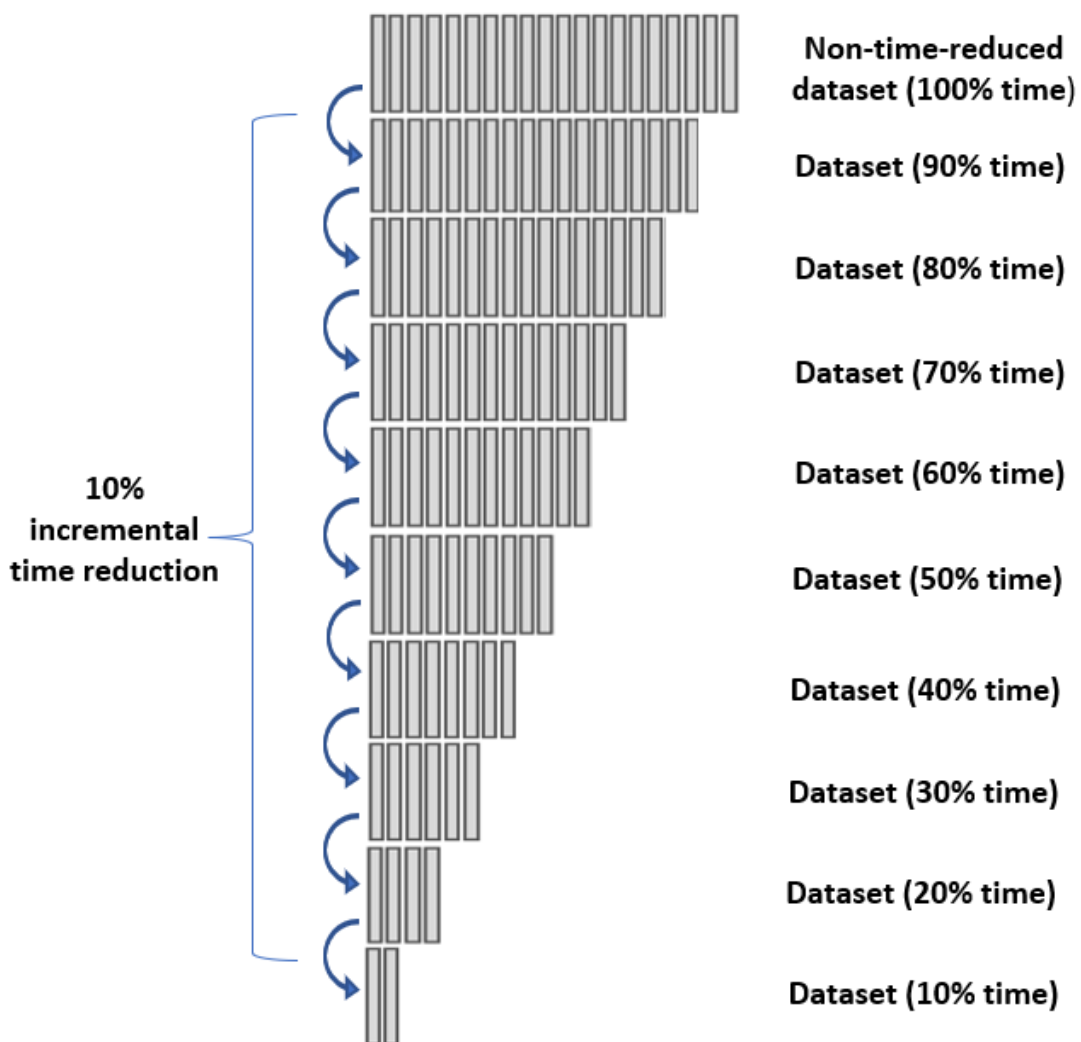
Figure 2. 3 Schematic representation of incremental time reduction implemented on our dataset

2.5.2 Image Reconstruction

Commercial cedar Sinai QPS/QGS software was used. All patients underwent low-dose CT imaging to obtain a CT attenuation map, also included in the image reconstruction process by the software. The software generated attenuation corrected (AC) and non-attenuation corrected (non-AC) images with multiple computer-generated parameters as per the standard of care protocol. Reconstructed rest and stress images underwent physician interpretation, including AC and Non-AC images. These images were original non-time-reduced images and were also used for diagnostic purposes. These images were considered to be the baseline data set used to compare with other incrementally time-reduced images in this study.

As mentioned in section 2.5.1, List mode was used for image acquisition and reframing raw data. In the next step, QPS/QGS software was ran on each truncated data list with reconstruction of a new series of cardiac polar maps, sectional images, gated images, and computer-generated parameters. Fig. 2. 4 summarize these steps.
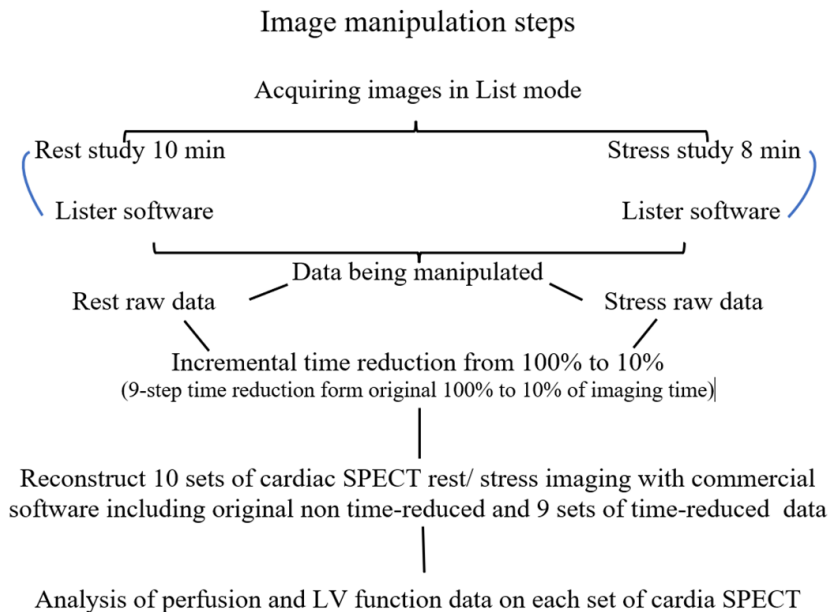
Figure 2. 4 Summary of image manipulation steps.

These images were referred to as "simulated time-reduced images". A CT attenuation map was not included in the reconstruction of the simulated time-reduced images.

2.5.3 Data Gathering and Image Interpretation

After creating reconstructed images, all original non-time-reduced and non-AC images and multistep time-reduced images were transferred to an external hard drive with two backup copies.

A master list for patient identification was created by assigning a number to each participant and recording their medical record number and initials. This master patients' list was linked with a research-generated ID number on a Redcap database. Through the master patient list and research ID number, the researchers could access detailed participants' clinical histories if needed.

First, the Cedar Sinai QPS/QGS application was run on all ten sets of the patient's raw data, including one non-time-reduced, non-AC data set and nine time-reduced data sets to generate polar maps and the parametric scores and numbers.

The following categories of information were gathered from the regenerated images:
1. General medical information for reporting standard-of-care images:
   a. demographics
   b. clinical
   c. past medical history
2. Parametric scores of perfusion images including:
   a. summed rest score (SRS)
   b. summed stress score (SSS)
   c. summed difference score (SDS)
   d. total perfusion deficit (TPD) at rest and stress
3. Parameters of left ventricular function include:
   a. end-systolic volume (ESV)
   b. end-diastolic volume (EDV)
   c. left ventricular ejection fraction (LVEF)

    d.   left ventricular wall motion abnormality and

    e.   transient ischemic dilation (TID) ratio

Information was gathered pertaining to count statistics, including total polar map counts, maximum counts per pixel and average counts per pixel for both rest and stress polar maps. This information was used for quality control measures and to monitor the accuracy of the Lister application in its generation of time-reduced lists with appropriate count statistics.

The next step was qualitative image analysis, completed after the image reconstruction. At this step, two researcher physicians, with 5 and 16 years of experience in nuclear cardiology, reviewed the original non-time-reduced and non-AC rest and stress polar maps and simulated time-reduced polar maps at different time points. They were blinded to the patient′s identifiers and the status of the imaging time frame of the polar maps they reviewed.

Image data series were randomly selected and were processed through QPS/QGS software to generate an image display for interpretation.

The qualitative assessment included evaluation of image interpretability, the certainty of the interpretation, the presence or absence of artifacts, the quality of the cardiac motion on gated images, and presence or absence of visual TID.

The physicians filled out a questionnaire regarding image quality and interpretation and had to rate whether the images were normal or abnormal, highlight any ischemia or infarct on the images, and finally answer questions regarding image interpretability, presence or absence of artifacts, and uncertainty about the image findings based on the artifacts such as those based on anatomic attenuating structures or artifacts caused by reduced imaging time. The physicians had the opportunity to incorporate computer-generated parametric scores and functional parameters into their decision-making for the purpose of finalizing their interpretation. After the questionnaire was answered, the case No, and reframed series of time reduction was identified. Finally, the information was transferred to the Redcap database to be used for further analysis. A sample of the questionnaire is provided in Fig. 2. 5.

Cardiac Research Dataset Questionnaire

Image interpretation by clinician

Case No.   **Reframe series:**

Rest perfusion scan:	**Normal** ☐ **Abnormal** ☐ **Artifact** ☐
Stress perfusion scan:	**Normal** ☐ **Abnormal** ☐ **Artifact** ☐
Infarct:	**Yes** ☐ **No** ☐ **Uncertain** ☐
Ischemia:	**Yes** ☐ **No** ☐ **Uncertain** ☐
TID:	**Yes** ☐ **No** ☐
Gated imaging quality:	**Good** ☐ **Mildly impaired** ☐ **Poor** ☐
Gated images:	**Normal** ☐ **Abnormal** ☐
If abnormal, why:	
Clinical evaluation:	**Normal** ☐ **Abnormal** ☐
Interpretable:	**Yes** ☐ **No** ☐
If not, why:	

Figure 2. 5 Research questionnaire.

2.5.4 Definition of the Perfusion Parameters

Summed rest score (SRS): The total amount of abnormality on the rest scan denoted by the computer software as a resting defect on the polar map (infarct or artifact). A rest score of SRS < 2 is considered normal.

Summed stress score (SSS): Total amount of abnormality on the stress scan that is detected by the computer software on a polar map (could be inducible ischemia or artifact with or without a fixed perfusion defect on rest status). SSS <4 is considered a normal or minimally abnormal stress perfusion study.

Summed difference score (SDS): Difference between SRS and SSS as a marker of reversibility. SDS >1 is considered abnormal and defined as the presence of inducible ischemia during the stress study.

The hypoperfusion severity was scored based on a 5-point scoring system defined as 0 = normal, 1 = minimal, mild perfusion abnormality, 2 = moderate perfusion impairment, 3 = significant perfusion impairment, and 4 = no perfusion.

Total perfusion deficit (TPD): A computer-generated score which includes the extent of perfusion deficits (above scores) and the severity of the deficits, expressed as a percentage relative to the whole left ventricular surface. A TPD < 5% is considered to be normal or minimal abnormality, TPD 5-9% represents mild perfusion abnormality, TPD 10-14% represents moderate perfusion abnormality, and TPD > 14% defines significant perfusion reduction.

The sensitivity, specificity and accuracy of the parameters mentioned above were evaluated as a function of time reduction.

2.6 Statistical Analysis

A comparison was made between computer-generated parametric scores of the original non-time-reduced and the time-reduced images. The sensitivity, specificity, and accuracy of the parameters in rating images as normal vs abnormal were evaluated as a function of time reduction.

For the two physicians , the sensitivity, specificity, and accuracy of the polar maps, sectional and gated image evaluation , presence or absence of ischemia, infarct and artifact, image interpretability and certainty of the imaging findings as a function of time reduction were analyzed separately.

In the following step, an inter-rater reliability test using Cohen′s Kappa statistics was implemented to measure the agreement between the two readers . Finally, the sensitivity, specificity, and accuracy of image interpretation as a function of time reduction for both readers were analyzed.

The changes in the mean of any scores in the cohort during simulated time reduction compared to non-time-reduced images as a function of time reduction were also analyzed using a student t-test for means, and relative p-values were provided.

The McNemar test was employed for analysis of paired nominal data of categorical change from normal to abnormal in reading polar maps by physicians as a function of count reduction by evaluating the p values. It was also used for evaluation of the impact of changing scores on changing category of the patient from normal to abnormal in SSS, SRS, SDS and percent of deficit in TPD at rest and at stress as a function of time reduction. Multiple p-values were generated and their statistical significance were evaluated.

The Microsoft Excel with Data Analysis ToolPack VBA package was used for data analysis.

Multiple graphic figures to better illustrate the findings were provided.

The formulae for calculating this study's sensitivity, specificity, accuracy and Cohen′s Kappa are shown below.

$$\text{Sensitivity:} \quad \frac{\text{True positive (abnormal cases)}}{\text{True positve+False negative}}$$

$$\text{Specificity:} \quad \frac{\text{True negative (normal cases)}}{\text{True negative+False positive}}$$

$$\text{Accuracy:} \quad \frac{\text{True positive+True negative}}{\text{True positive+False positve+False negative+True negative}}$$

Cohen's kappa is calculated based on the following formula:

$$K = \frac{p_0 - p_e}{1 - p_e}$$

Where p_0 is the relative observed agreement among raters and p_e is the hypothetical probability of chance agreement.

2.7 Results

2.7.1 The Impacts of Time Reduction on Image Homogeneity

Twenty-six patients were included with a mean age of 65 years (39-87 years). Among those enrolled, 14/26 (54%) were males. 16 out of 26 (61.5%) were normal, and 10 out of 26 (38.5%) were abnormal at baseline. The effect of time reduction on the visual appearance of polar map homogeneity can vary among patients. For example, the images shown below belong to a normal participant (ID no.6). The non-time-reduced polar maps (100% imaging time) were completely normal. They remained normal when imaging time was reduced to 60%, though the polar maps demonstrated mild inhomogeneity with mildly abnormal scores when the time was reduced to 10% (Fig. 2. 6)
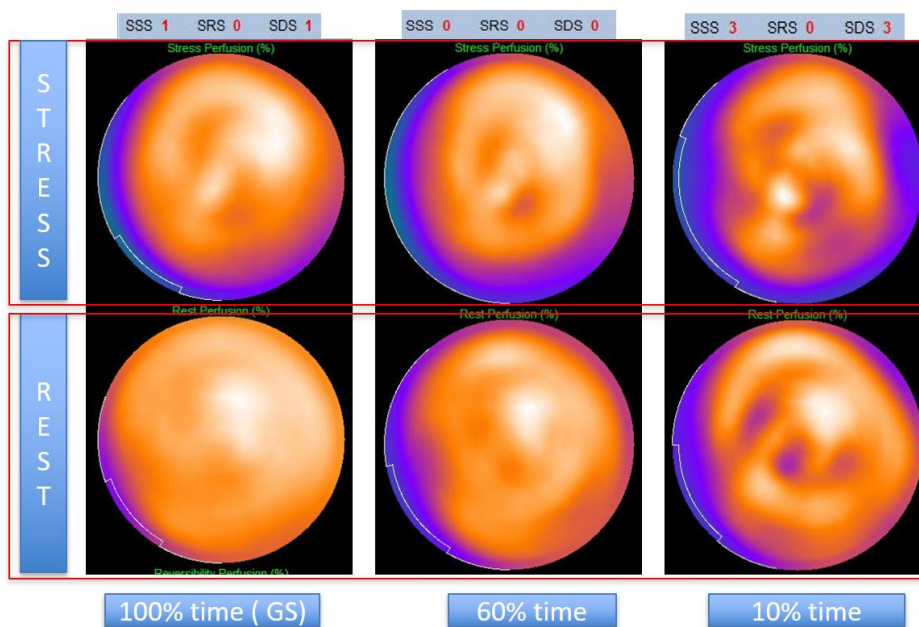
Figure 2. 6 Polar maps and scores of a normal study at baseline with a mild visual and minimal quantitative impact of time reduction at two-time points (60% and 10% imaging time reduction).

The following is an example of an abnormal image with 100% time, for participant ID no.24. This image contains an inferior wall defect (the inferior wall is often supplied by the right coronary artery). The defect appears as a purple region on the 100% imaging time polar plots. The inferior wall defect is present on both rest and stress images (which can represent an infarct). Defects on the polar map became more pronounced and computer-generated scores showed greater abnormality when the time was reduced to 70%. Further pronouncement of the defects and more score abnormality occurred when imaging time was further reduced to 10% compared to non-time-reduced images (Fig.2. 7).
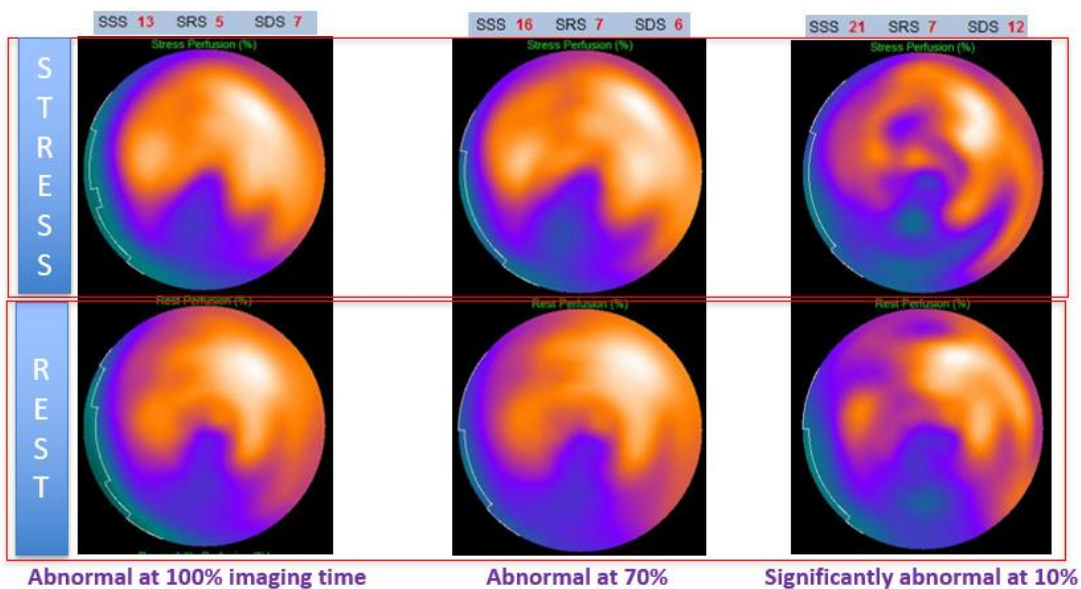
Figure 2. 7 Polar maps and scores of an abnormal study at baseline (infarct in the RCA territory), and polar maps at 70% and 10% of full imaging time. The polar maps illustrate successive pronouncement of the inferior wall baseline defect with progressive imaging time reduction and increasing quantitative abnormalities with progressive imaging time reduction.

2.7.2 Qualitative Analysis

Baseline non-time-reduced polar maps and 9-step time-reduced rest and stress polar maps (260 series of images) were read by two physicians. The interrater reliability of the two readers was evaluated with Cohen's Kappa, which demonstrated a substantial agreement with K=0.74.

The normalcy of separate reports generated by two readers for the same images demonstrated a relatively good correlation (Fig. 2. 8). A combined two reader normalcy report diagram (Fig 2. 9) showed 90% correct reads when the time was reduced to 80% of the baseline and a reasonably good percentage of 85.5% correct reads were achieved until the imaging time was reduced to 50% compared to non-time-reduced images.
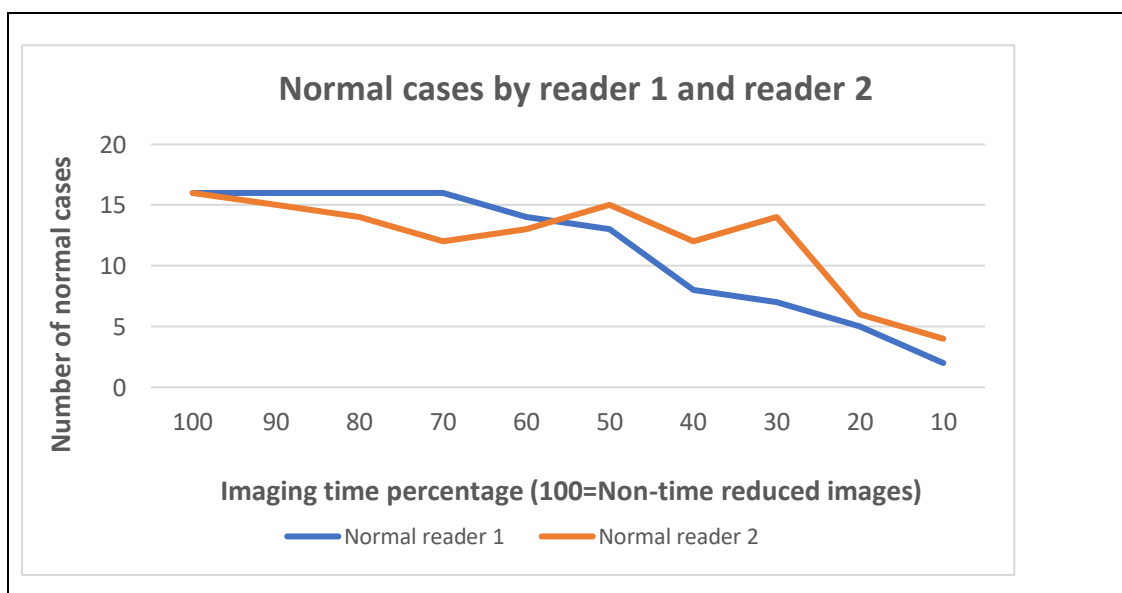
Figure 2. 8 Normal cases read by readers 1 and 2 separately. (16 out of 26 were normal at baseline in this study).
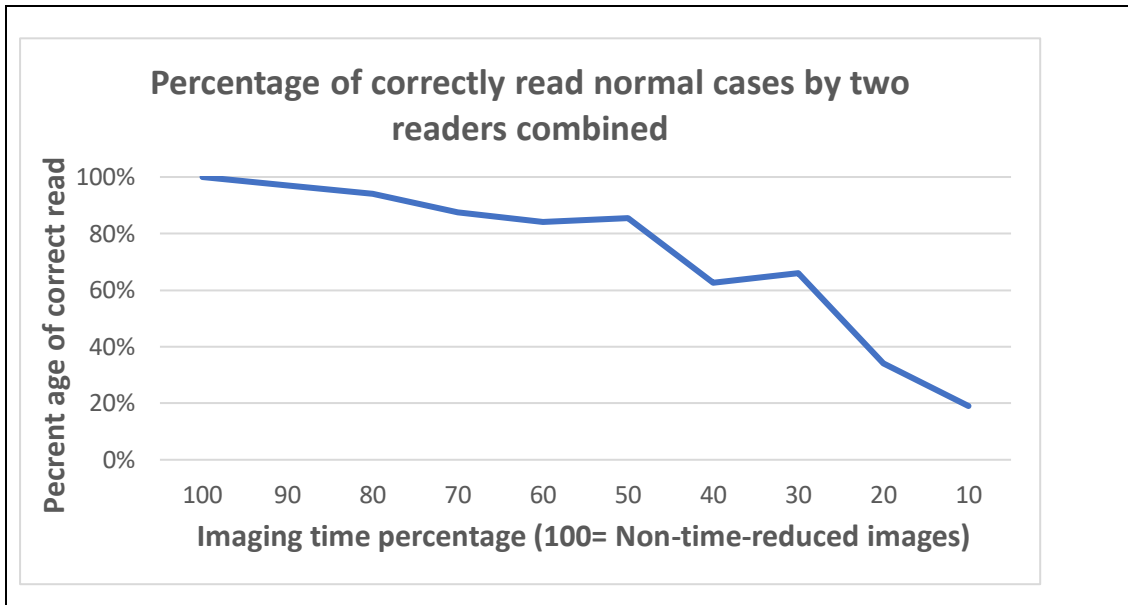
Figure 2. 9 The combined result of the percentage that two readers correctly read normal cases as a function of imaging time reduction.

The performance of two readers regarding image interpretability was impacted after multiple steps of time reduction (Fig.2. 10). The combined two-reader performance on image interpretability demonstrated that 98% of the polar maps were interpretable until the time was reduced to 60% compared to non-time-reduced images. The image interpretability remained high at 88% until the time was reduced to 50% (Fig. 2. 10).
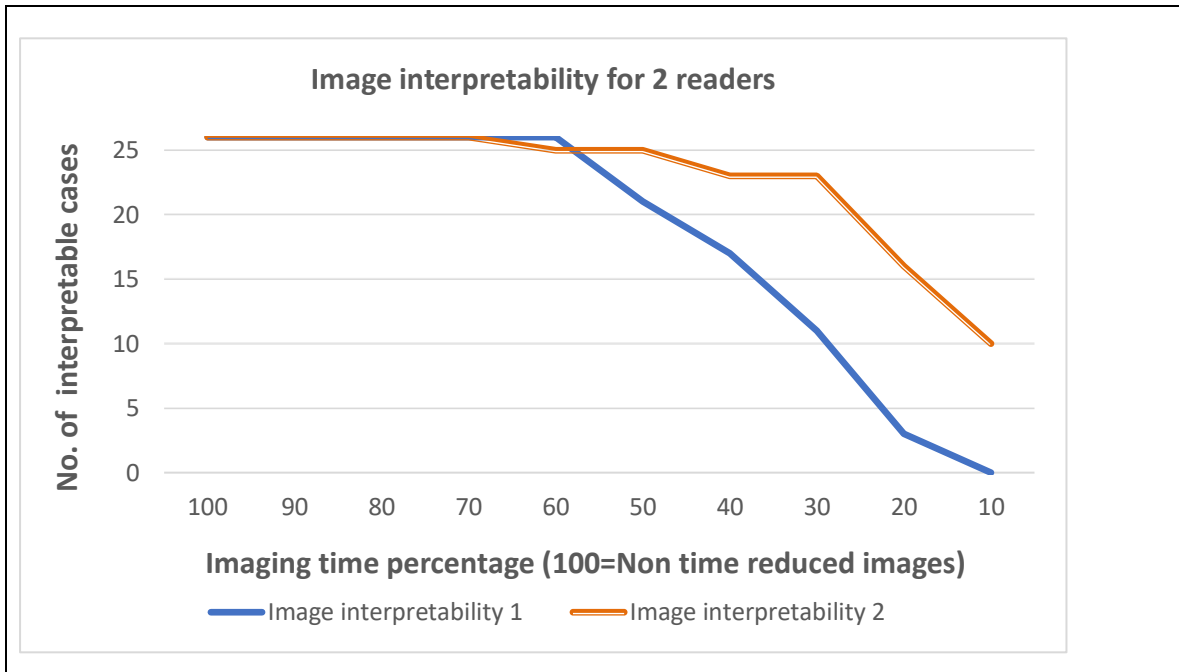
Figure 2. 10 Number of interpretable cases as a function of time reduction for each reader.
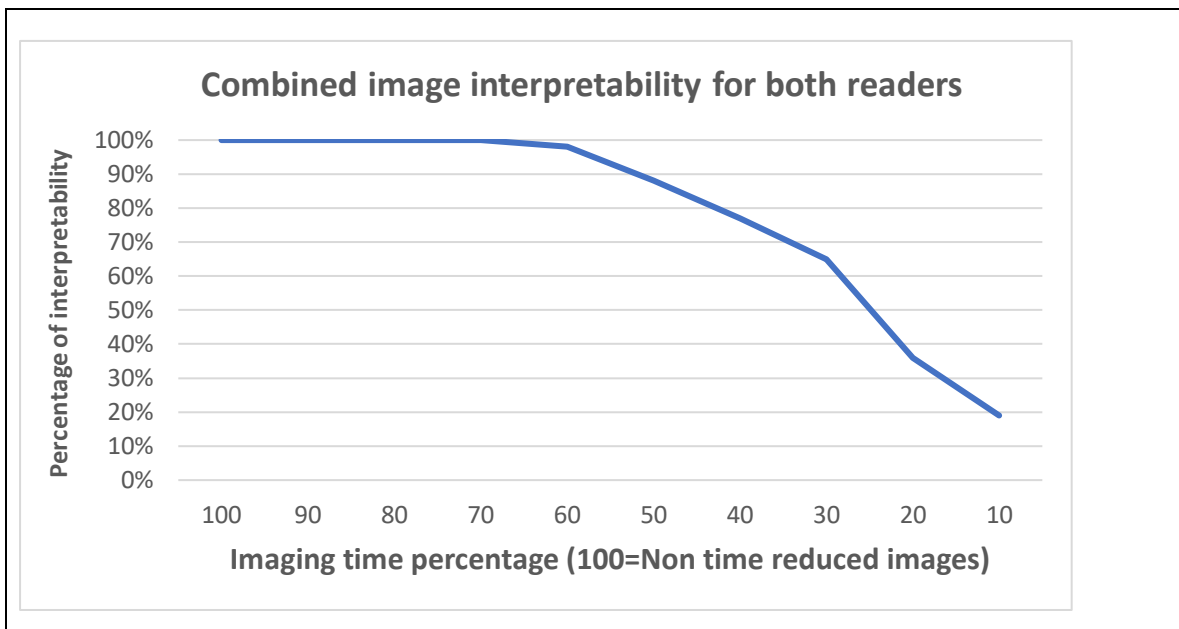
Figure 2. 11 Combined image interpretability for both readers as time reduced.

Certainty of image interpretation followed the same pattern as image interpretability which is shown in Fig. 2. 12. The combined two-reader performance demonstrated that certainty started to decline when time was reduced to 70% compared to non-time-reduced images (Fig. 2. 13).
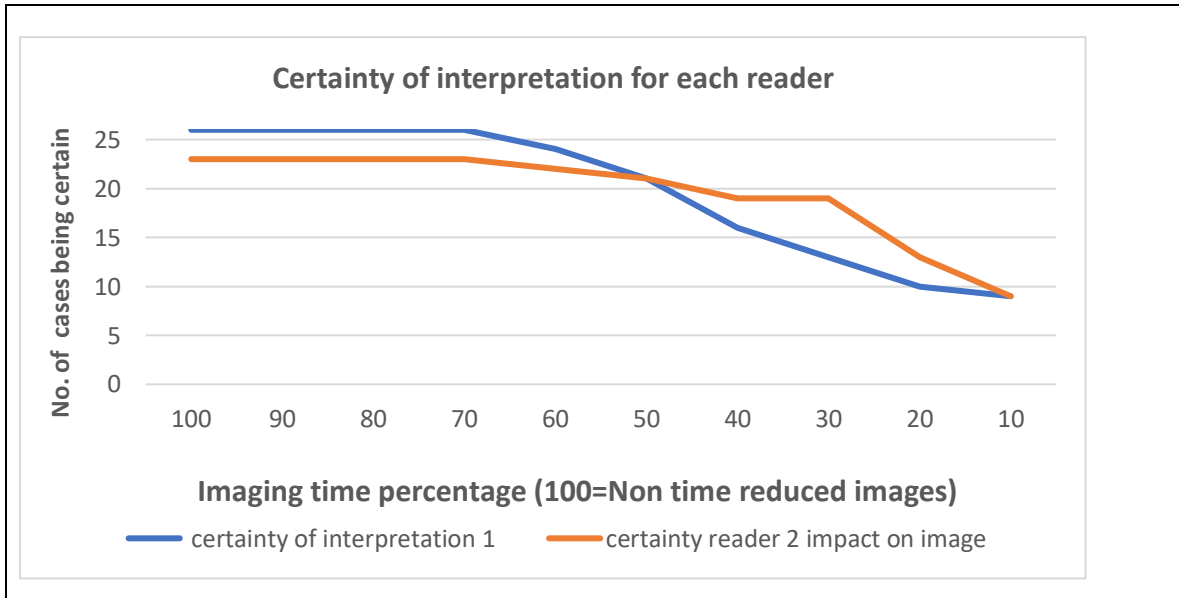
Figure 2. 12 Certainty of interpretation for readers 1 & 2 separately
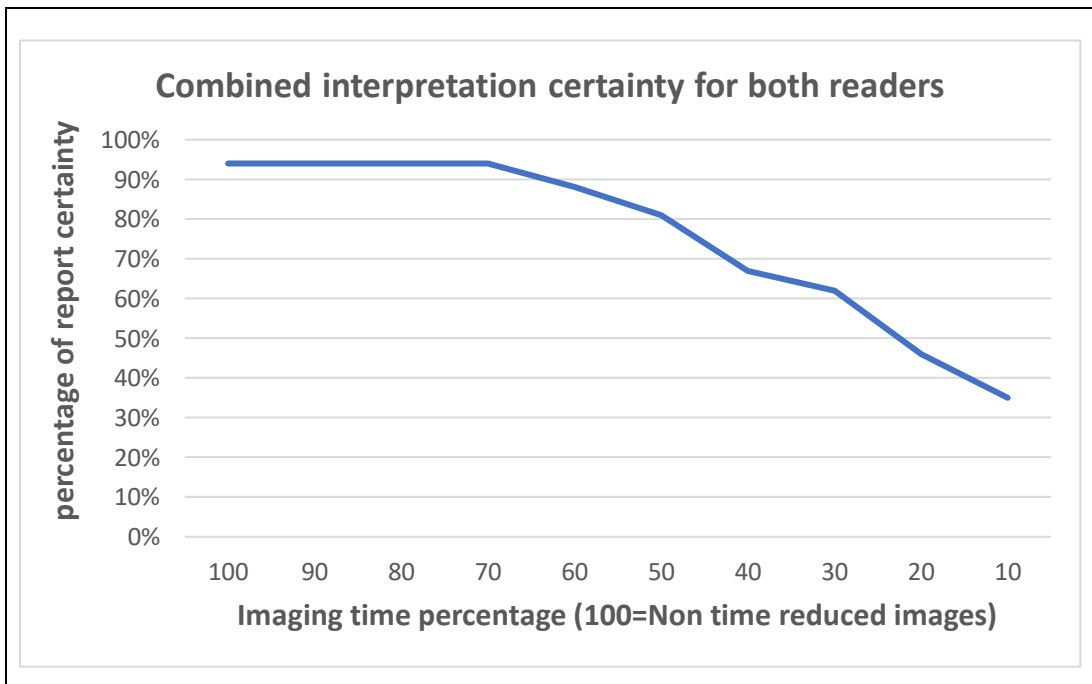
Figure 2. 13 Combined certainty of report interpretation for both readers.

Image interpretation by two readers demonstrated that time reduction increases image inhomogeneity and impacts the reader's ability to correctly define polar maps as normal vs abnormal. The sensitivity, specificity and accuracy of the test was affected by a decrease in the readers' ability to properly identify normal or abnormal polar maps with decreasing imaging time. The performance of each reader is demonstrated in Fig 2. 14-2. 17.

The combined performance of the two readers showed that the qualitative analysis of the rest polar maps had a sensitivity of more than 0.8 until the time was reduced to 40%. At the same level of time reduction, the specificity and accuracy remained close to 0.9. On stress images, sensitivity remained 0.84-1.0 throughout time reduction, but specificity and accuracy reduced to less than 0.8 when imaging time was reduced to 50% compared to non-time-reduced images (Fig. 2.18 & 2.19). (Fig. 2.18 & 2.19).
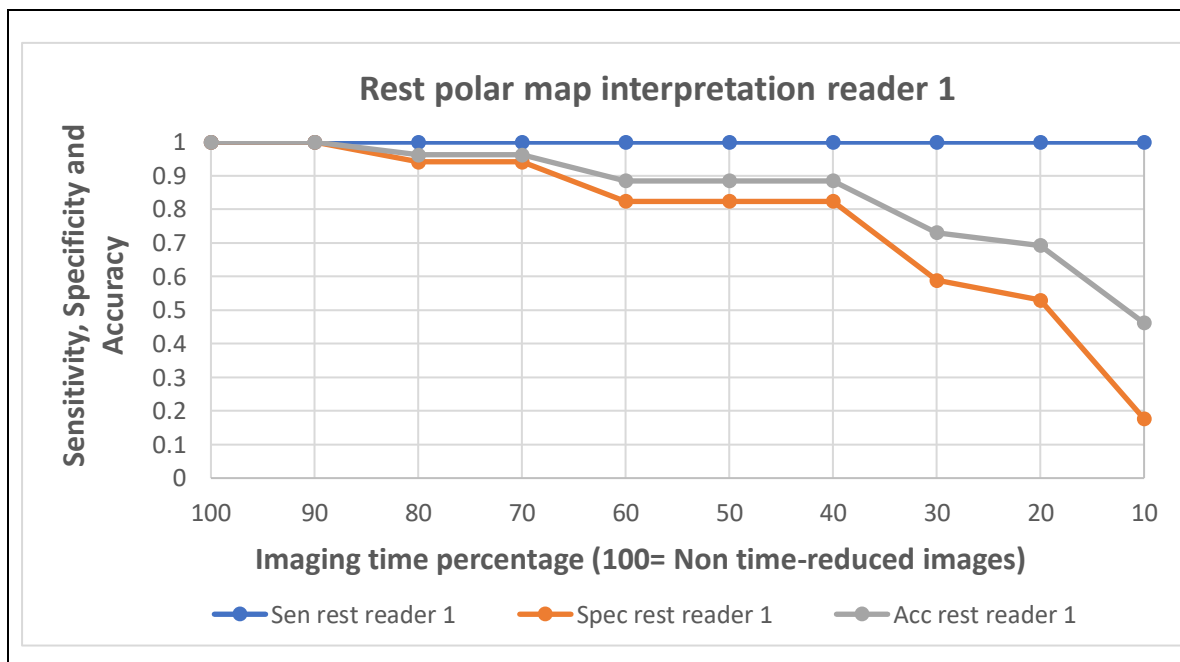
Figure 2. 14 Reader 1 rest image reading sensitivity, specificity, and accuracy.
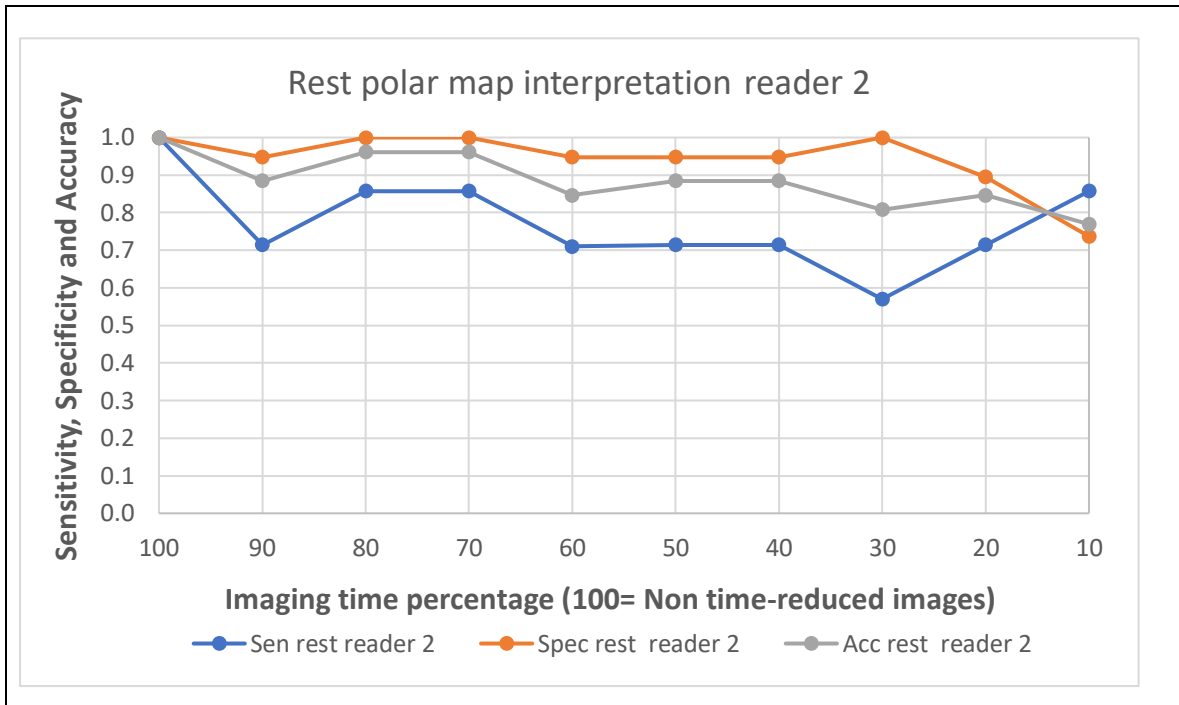
Figure 2. 15 Reader 2 rest image reading sensitivity, specificity, and accuracy.
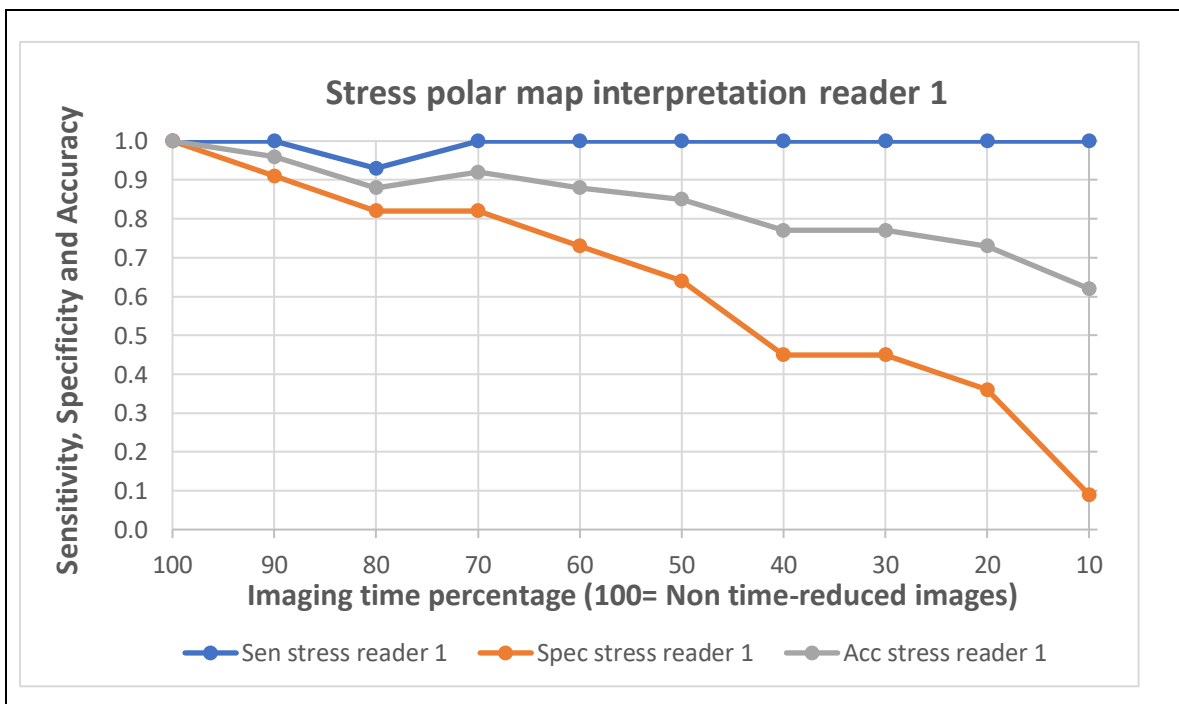
Figure 2. 16 Reader 1 stress image reading sensitivity, specificity, and accuracy.
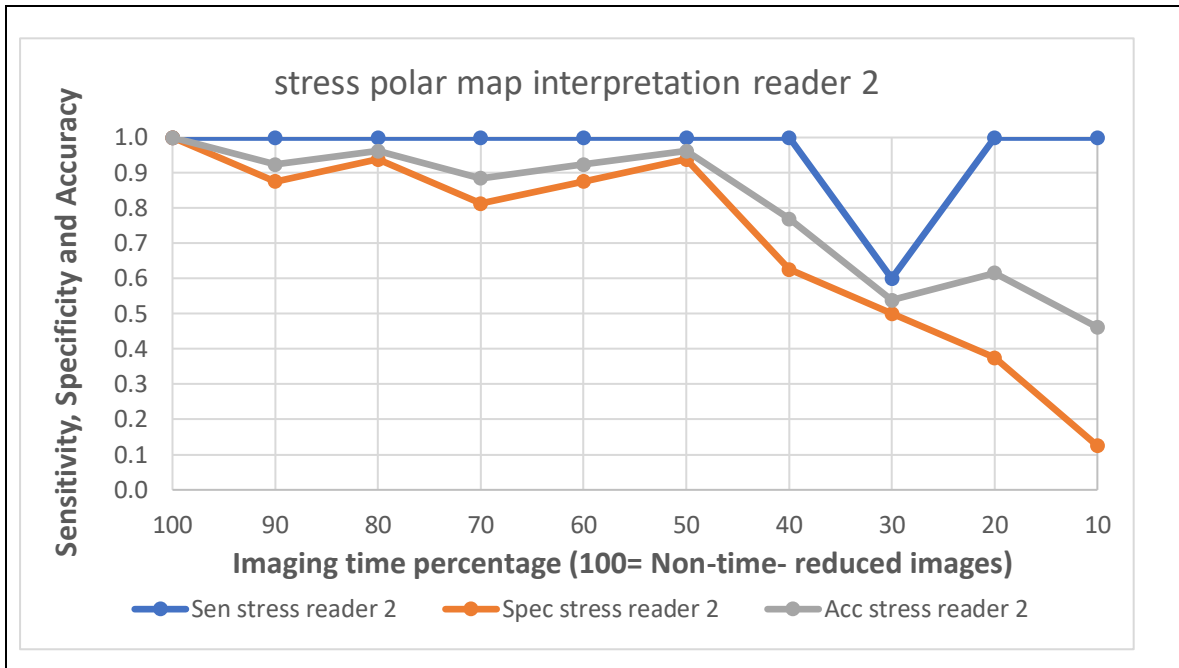
Figure 2. 17 Reader 2 stresses image reading sensitivity, specificity, and accuracy.
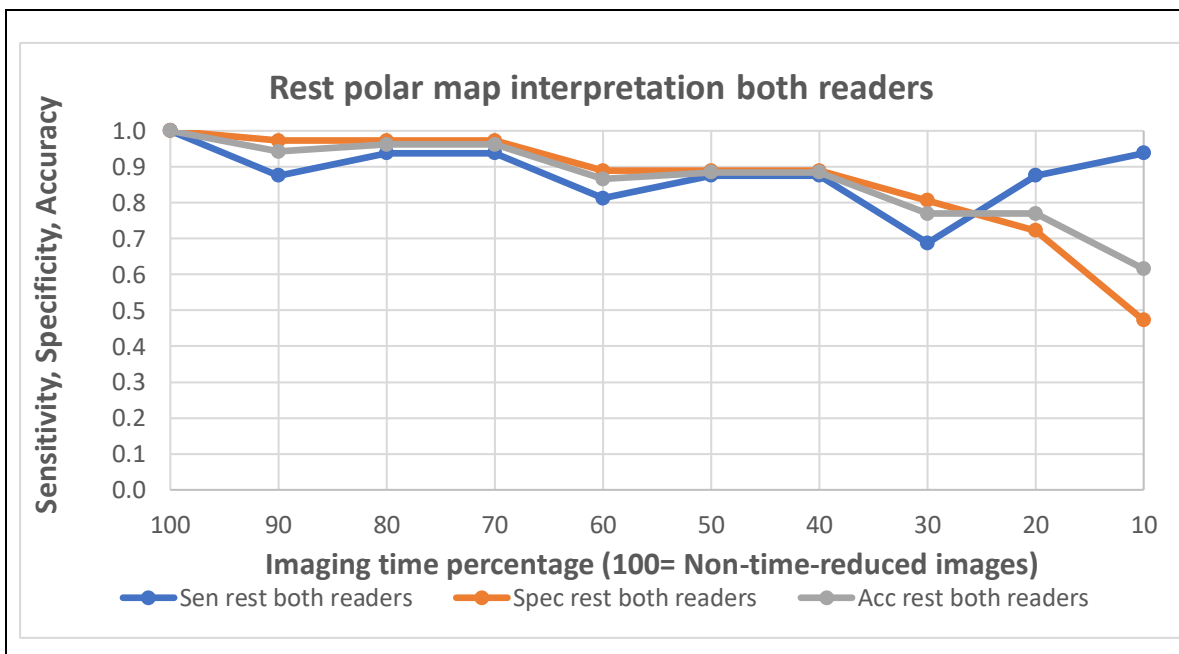
Figure 2. 18 Combined readers rest image reading sensitivity, specificity, and accuracy as a function of image time reduction.
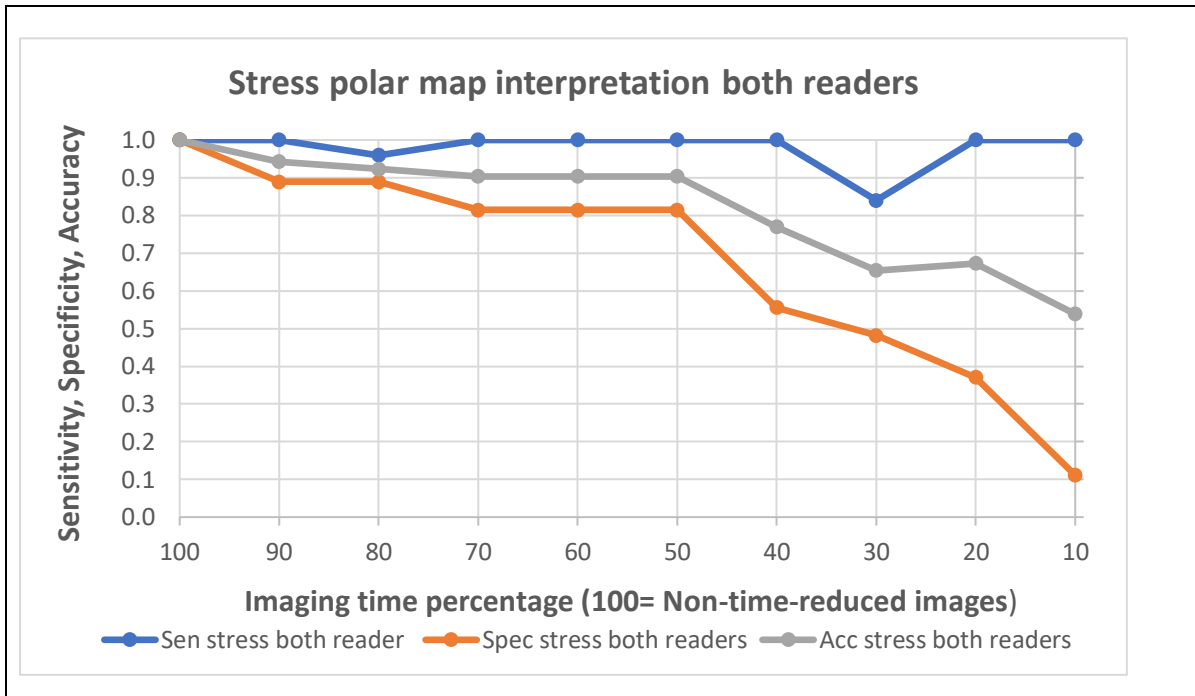
Figure 2. 19 Combined readers stress image reading sensitivity, specificity, and accuracy as a function of image time reduction.

For gated imaging, there was a deterioration in image quality when the imaging time was reduced to 30% compared to nonreduced time images (Fig.2. 20).
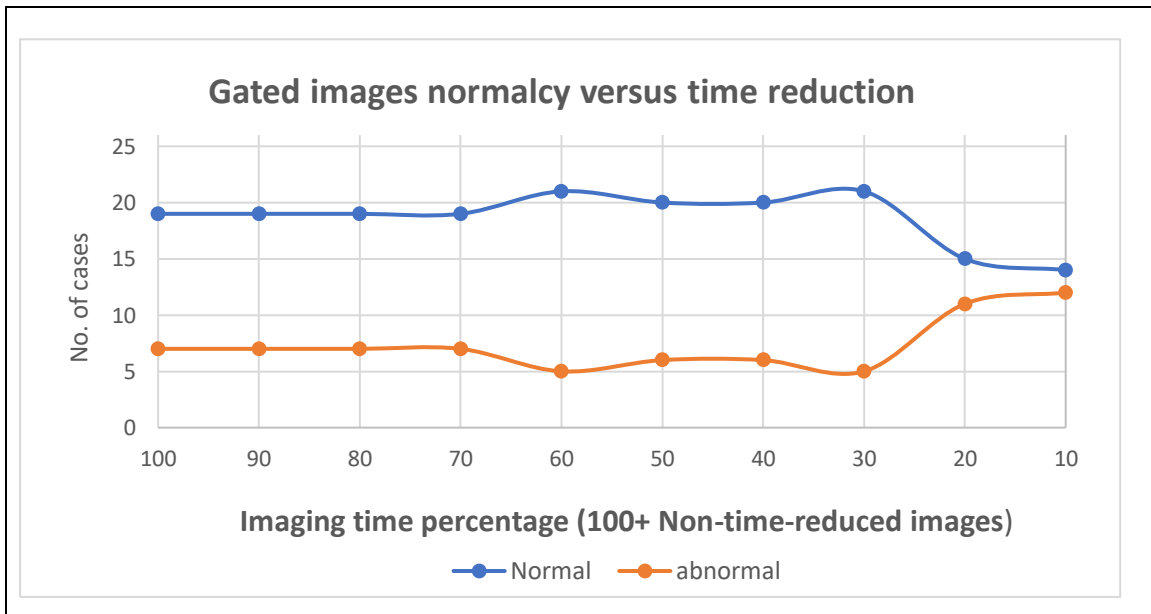
Figure 2. 20 The impact of time reduction on gated image normalcy.

2.7.3 Quantitative Analysis

Two sets of quantitative parameters were evaluated.

A) Perfusion parameters for all patients include 1) Summed rest score (SRS), a summation of all perfusion defect scores at rest image. According to our data, this parameter remained sensitive, specific, and accurate > 0.9 until the time was reduced to 30% compared to non-time-reduced images (Fig. 2.21).

2) Summed stress score (SSS), a summation of all perfusion defect scores at stress image. Our data showed that the specificity and accuracy of SSS remained constant at 0.8 and above until time reduced to 50% compared to non-time-reduced images. However, during the time reduction the sensitivity varied between 0.8 to 1.0 (Fig. 2.22).

3) Summed difference score (SDS) defines as a summation of difference scores at rest and stress (SSS-SRS). Our data showed more variability in this parameter's sensitivity, specificity and accuracy during time reduction than SRS and SSS. The specificity degraded earlier when the time was reduced to 80%, but accuracy remained ≥ 0.8 until the time was reduced to 50% (Fig. 2. 23).

4) Total perfusion deficit (TPD) at rest represents the severity and extension of perfusion deficits. Our study demonstrated TPD rest has high specificity and accuracy > 0.9 until time reduced to 30% compared to non-time-reduced images; however, it lost its sensitivity earlier when time just reduced to 90% (Fig. 2.24).

5) Total perfusion deficit (TPD) at stress showed sensitivity, specificity, and accuracy ≥ 0.8 until time reduced to 50% compared to non-time-reduced images (Fig. 2.25).
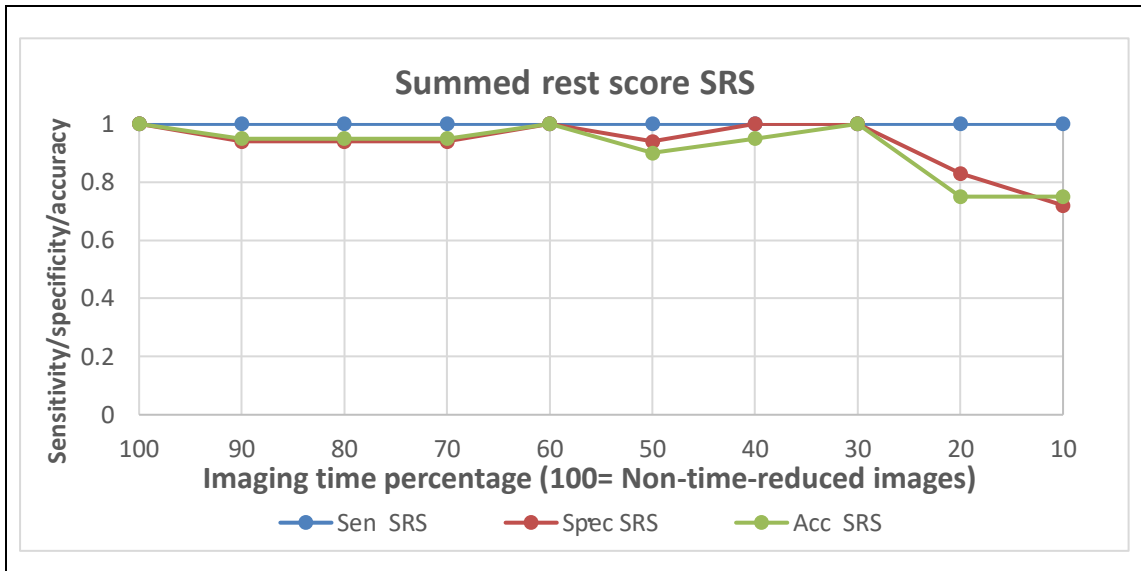
Figure 2. 21 Sensitivity, specificity, and accuracy of SRS during time reduction.
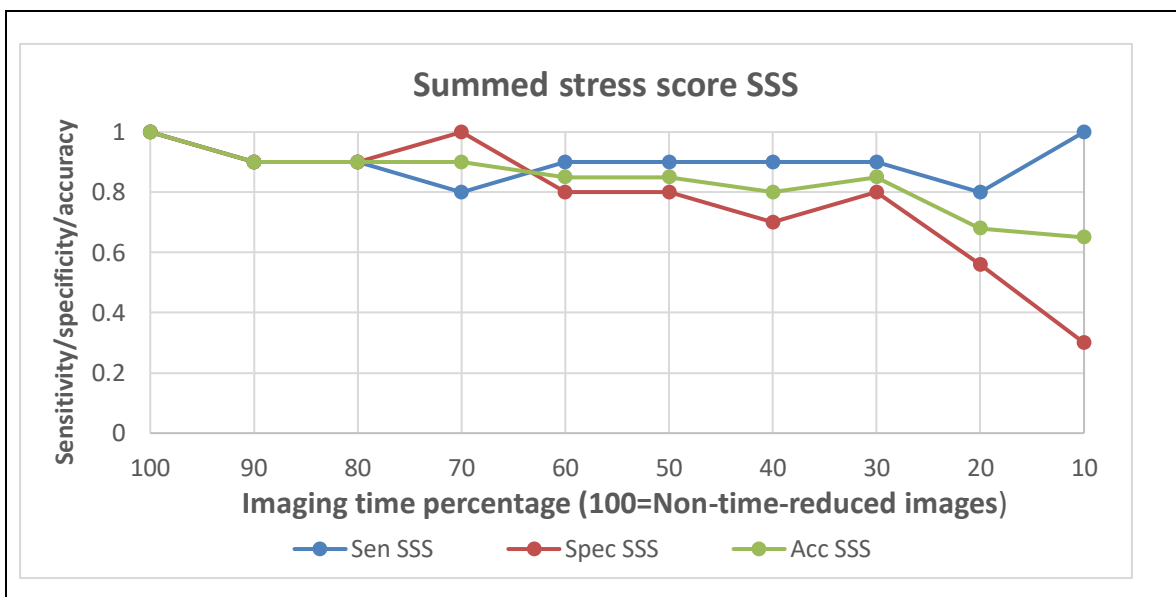
Figure 2. 22 Sensitivity, specificity, and accuracy of SSS during time reduction.
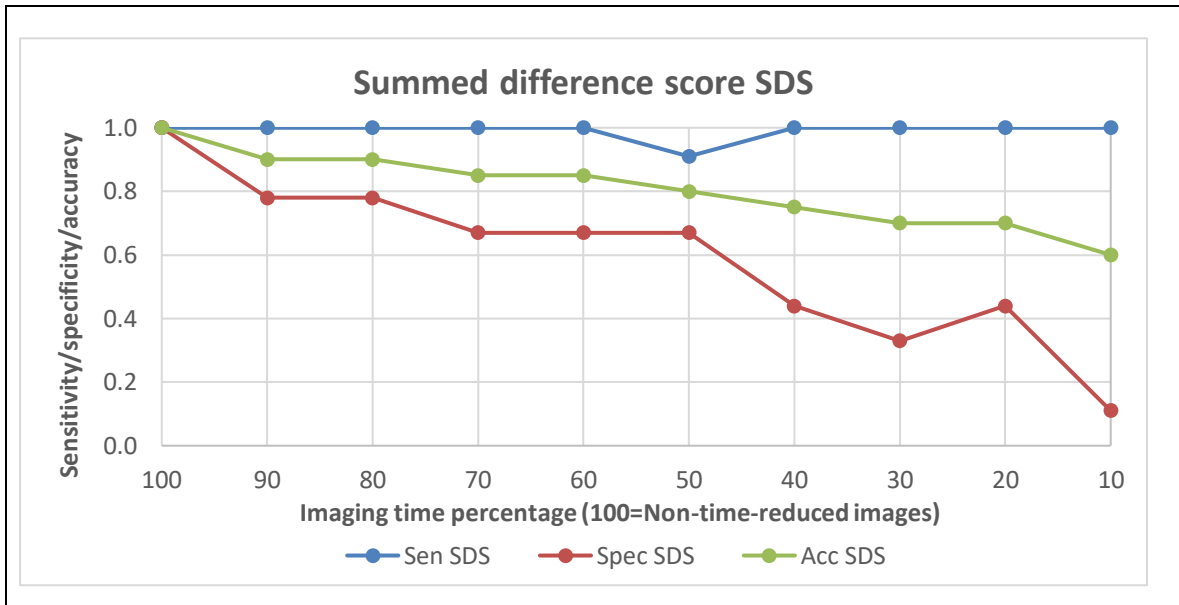
Figure 2. 23 Sensitivity, specificity, and accuracy of SDS during time reduction.
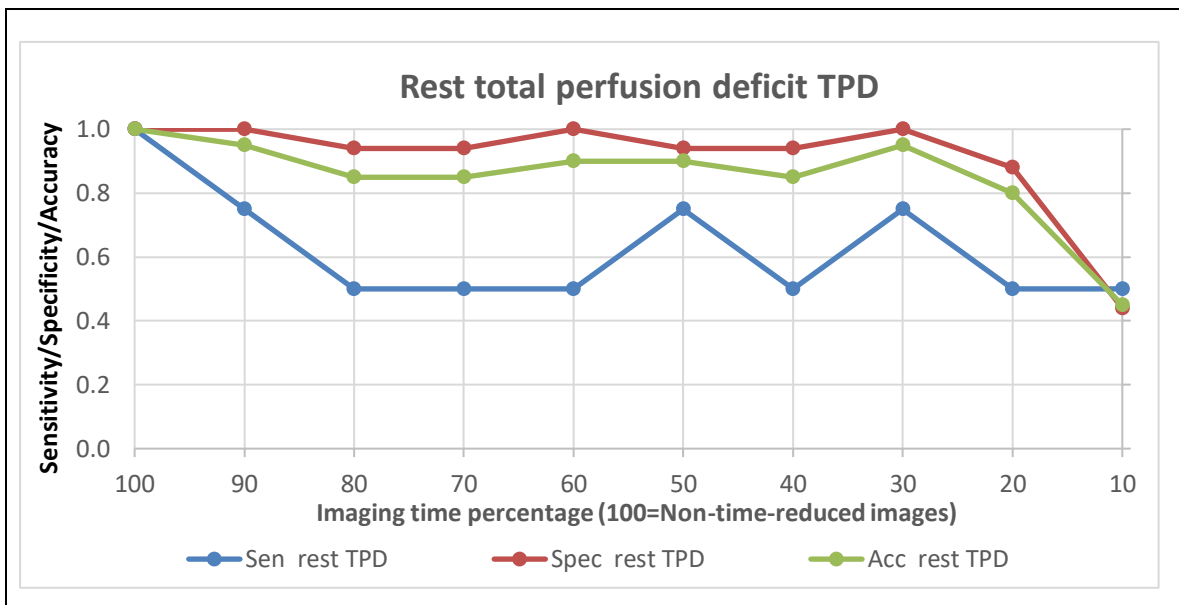
Figure 2. 24 Sensitivity, specificity, and accuracy of rest TPD during time reduction.
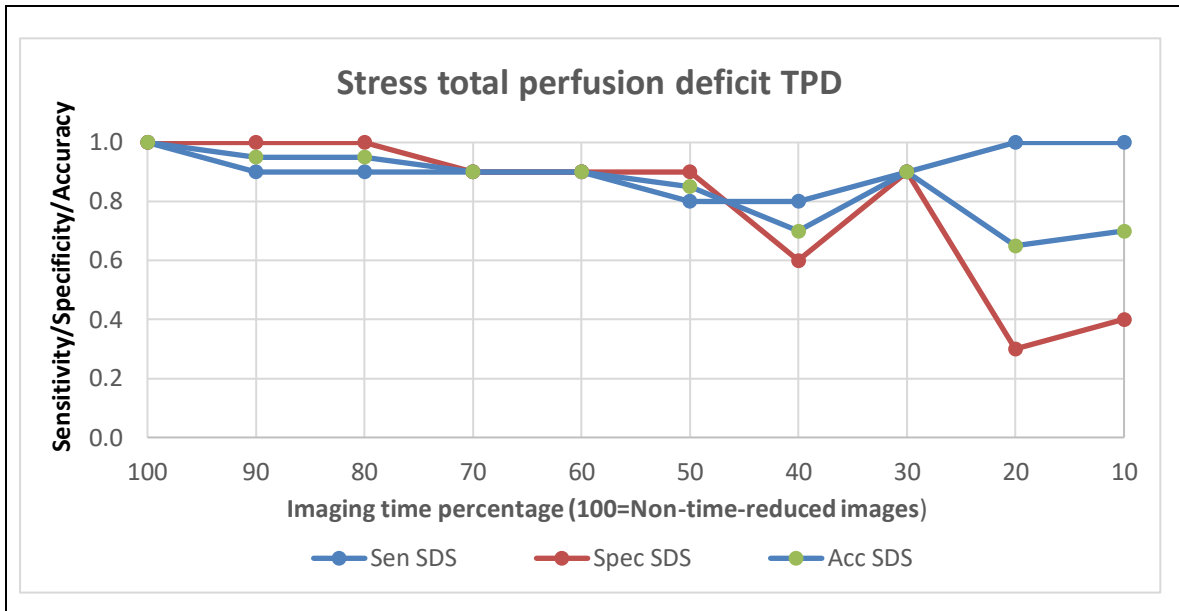
Figure 2. 25 Sensitivity, specificity, and accuracy of stress TPD during time reduction.

The relationship between the average of scores and average TPD of the cohort during time reduction are provided in Fig 2.26.
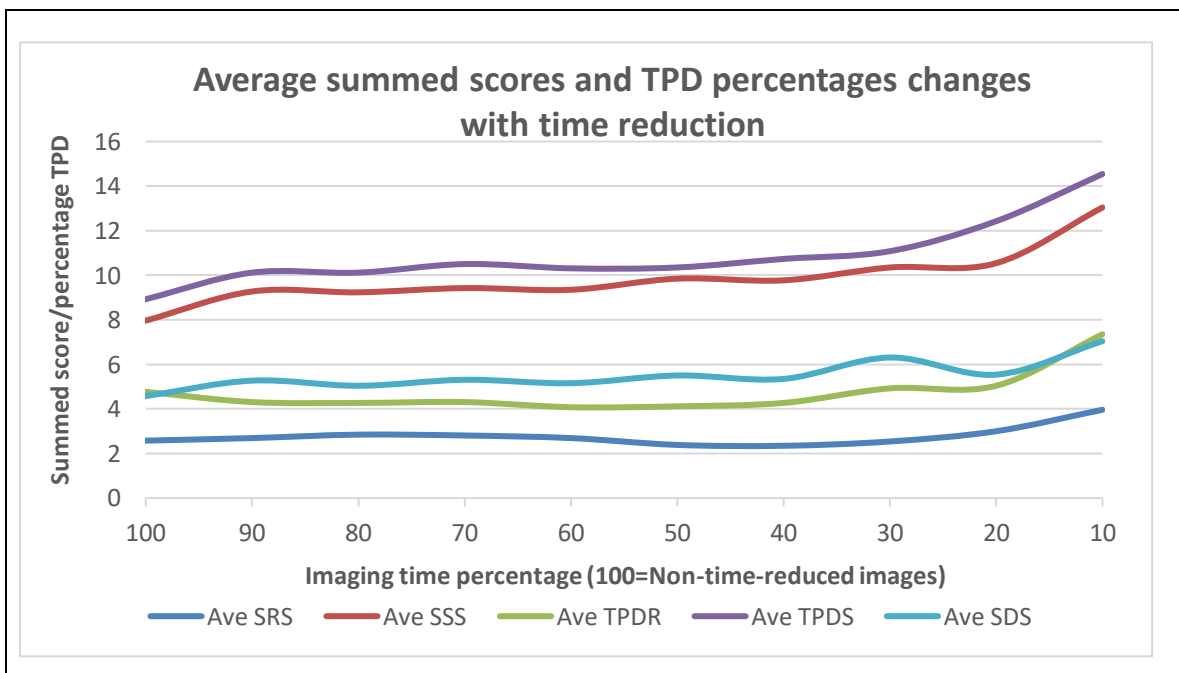
Figure 2. 26 Average of the scores and TPD changes during time reduction.

B) Functional parameters: 1) Ejection Fraction (EF) demonstrated changes with time reduction ranging from 21% to -45% on rest imaging and 11.5% to -28% on stress imaging predominantly in the negative direction (Fig. 2.27).
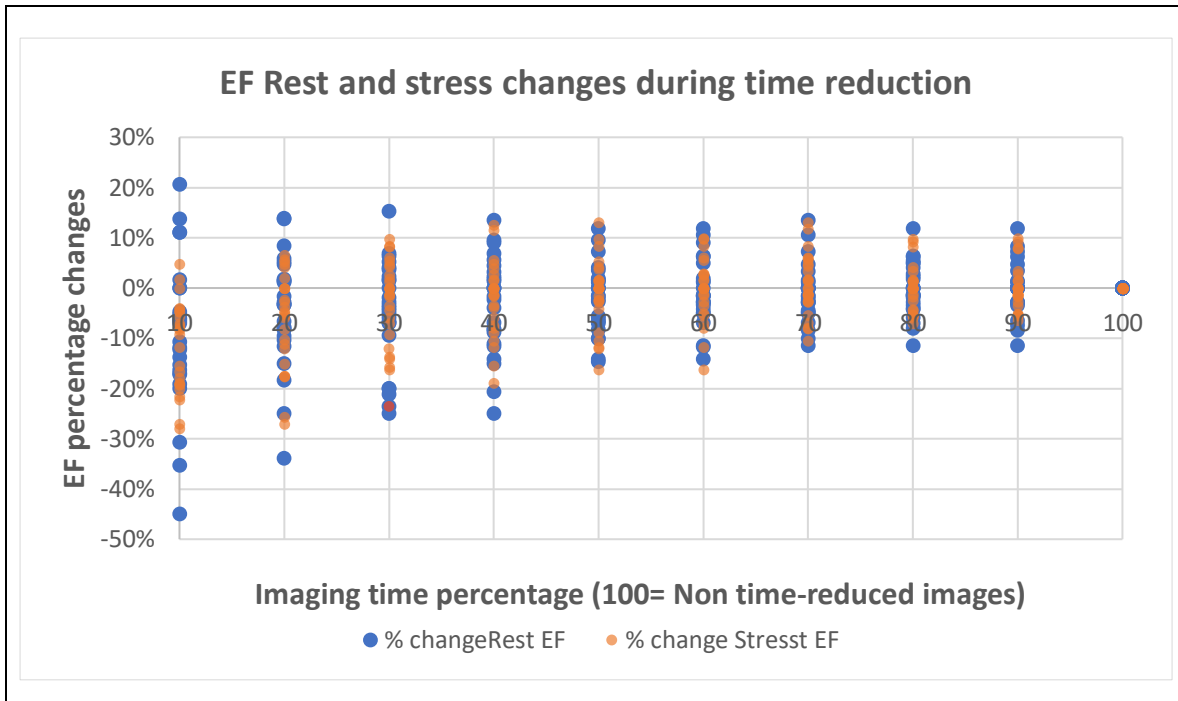
Figure 2. 27 Rest and stress EF changes during time reduction.

Regarding EF changes, there was no clear cut off point in literature review to define the level of a significant change. The EF changes > 15% in magnitude compared to non-time-reduced images were arbitrary selected in this study and considered significant. Rest and stress EF became abnormal with magnitude of change > 15% when time was reduced below 30% compared to non-time-reduced images (Fig. 2.28).
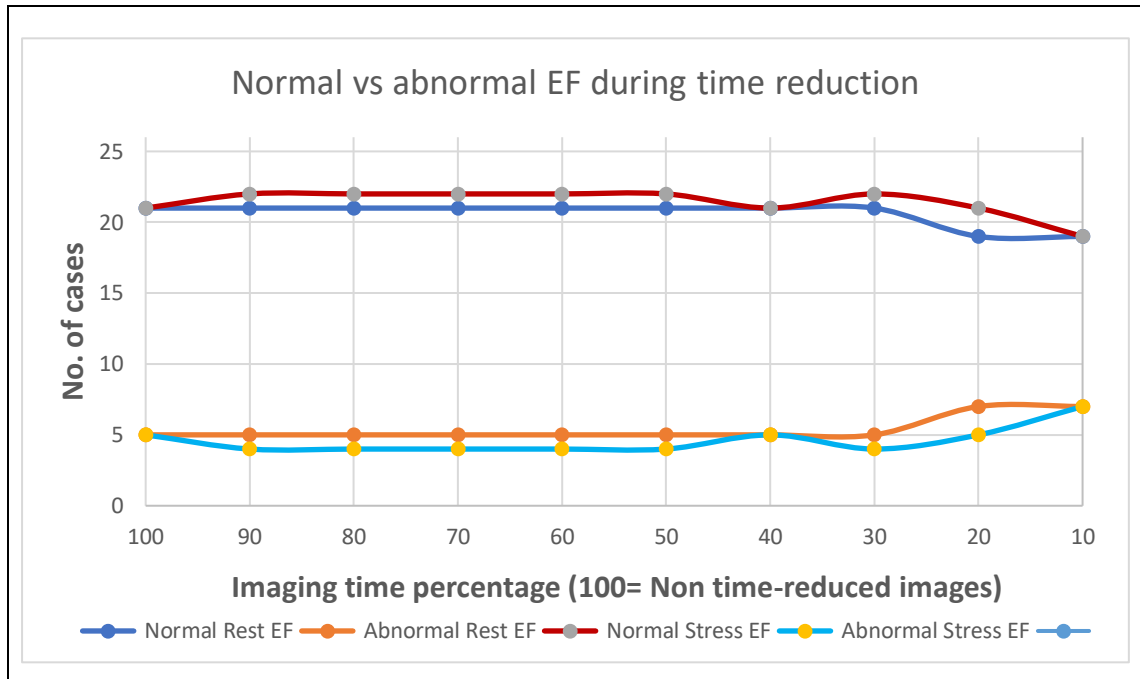
Figure 2. 28 Number of abnormal Rest and stress EF during time reduction.

2) End systolic volume (ESV) and 3) End diastolic volume (EDV). ESV demonstrated a wider range of changes from -36% to 150% for rest images and -32% to 139% for stress images, predominantly in the positive direction. EDV changes range from 22% to 35% for rest images and -41% to 26% for stress images compared to non-time-reduced images, predominantly in the negative direction.

Even though the range of volume changes was wide, the absolute value of the EDV and ESV remained in the same category of the normal or abnormal of the baseline imaging. (Fig. 2. 29 & 2. 30).
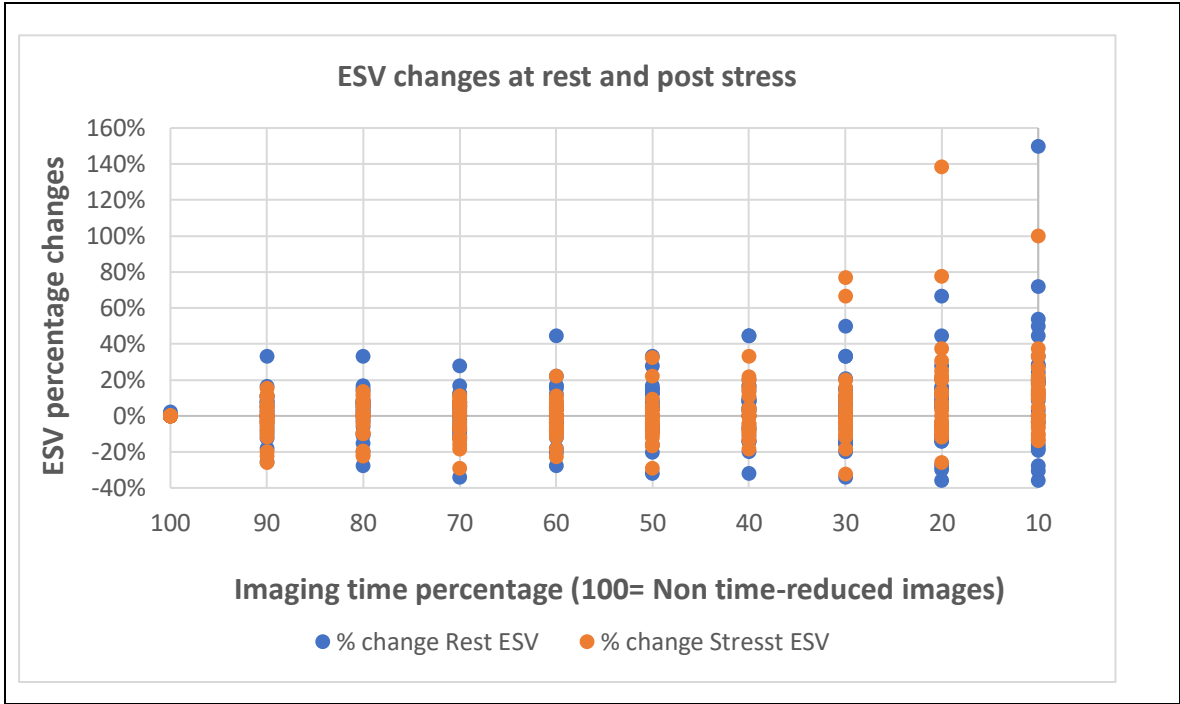
Figure 2. 29 ESV volume changes compared to non-time-reduced images.
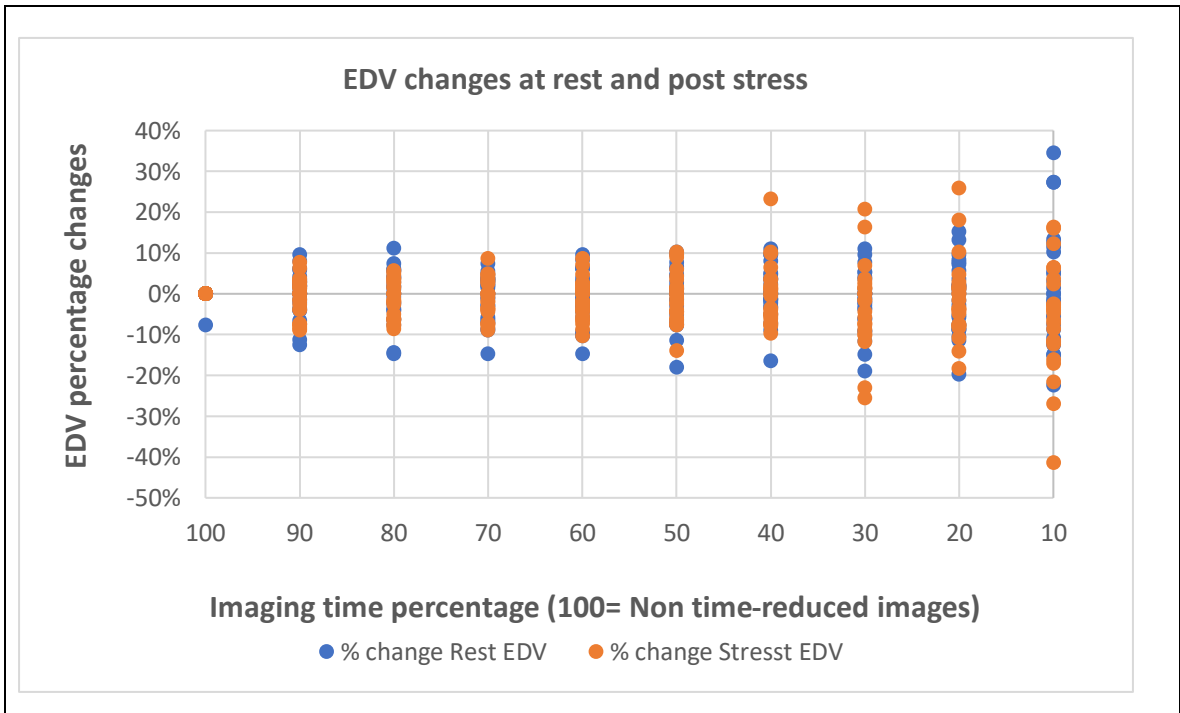
Figure 2. 30 EDV volume changes compared to non-time-reduced images.

The effect of time reduction on mean scores varied, as shown in Table 2. 2. SDS, SRS and TPD at rest demonstrated significant mean score changes when imaging time was reduced to 30% and 10%. Changes occurred at greater imaging time (i.e., less image time reduction) for SSS and for stress TPD.

Table 2. 2 Perfusion scores Means and Standard Deviations (SD) of the cohort during time reduction.

Parametric scores		Time 100%	Time 90%	Time 80%	Time 70%	Time 60%	Time 50%	Time 40%	Time 30%	Time 20%	Time 10%	p-value significance of the mean changes
SSS	Mean	8.0	9.3	9.2	9.4	9.2	9.7	9.8	10.3	10.5	13.0	All significant except at 80% & 60%
	SD	8.4	9.3	9.2	8.9	8.7	9.0	8.5	9.7	8.8	9.1	
SRS	Mean	2.6	2.7	2.8	2.8	2.7	2.4	2.3	2.5	3.0	4.0	Significant at 10%
	SD	5.2	5.1	5.5	5.3	5.5	5.0	4.9	5.9	6.2	6.2	
SDS	Mean	4.6	5.3	5.0	5.3	5.2	5.5	5.3	6.3	5.5	7.0	Significant from 10% - 30%
	SD	4.8	5.1	4.6	5.0	4.7	4.7	4.6	6.0	4.8	5.2	
TPD Rest	Mean	4.8	4.3	4.3	4.3	4.1	4.1	4.3	4.9	5.0	7.3	Significant at 10%
	SD	5.9	6.4	6.2	6.1	6.9	5.3	6.6	6.6	7.2	7.0	
TPD stress	Mean	8.9	10.1	10.1	10.5	10.3	10.3	10.7	11.1	12.4	14.5	All significant except at 90%, 80%, 50%
	SD	8.7	9.7	9.9	9.8	9.4	9.5	9.2	9.3	9.2	9.1	

The McNemar test was used for comparing paired nominal data of normal versus abnormal polar maps, SRS, SSS, SDS TPD at rest and stress.

The McNemar tests have shown that readers were less able to distinguish between normal and abnormal polar maps when imaging time was reduced to 40% and below. The p-values were as follows; p-value of 0.013 at the imaging time of 40%, p-value of 0.007 at the

imaging time of 30%, p-value of 0.004 at the imaging time of 20%, and p-value of 0.000 at the imaging time of 10%.

The McNemar test demonstrated no significant change in SRS, SSS and TPD rest during time reduction. For SDS, the McNemar test demonstrated significant change when imaging time was reduced to 10% with a p-value of 0.041. The TPD stress also demonstrated significant change when imaging time was reduced to 20% and 10%, with p-values of 0.023 and 0.041, respectively.

Table 2. 3 Summarizes McNemar test results. The significant p-values are provided.

Variables	P-value Time 90%	P-value Time 80%	P-value Time 70%	P-value Time 60%	P-value Time 50%	P-value Time 40%	P-value Time 30%	P-value Time 20%	P-value Time 10%
Polar map	Non-significant	Non-significant	Non-significant	Non-significant	Non-significant	0.013	0.007	0.004	0.000
SRS	Non-significant	Non-significant	Non-significant	Non-significant	Non-significant	Non-significant	Non-significant	Non-significant	Non-significant
SSS	Non-significant	Non-significant	Non-significant	Non-significant	Non-significant	Non-significant	Non-significant	Non-significant	Non-significant
SDS	Non-significant	Non-significant	Non-significant	Non-significant	Non-significant	Non-significant	Non-significant	Non-significant	0.041
TPD Rest	Non-significant	Non-significant	Non-significant	Non-significant	Non-significant	Non-significant	Non-significant	Non-significant	Non-significant
TPD Stress	Non-significant	Non-significant	Non-significant	Non-significant	Non-significant	Non-significant	Non-significant	0.023	0.041

2.8 Discussion

The purpose of this study is to assess the impact of reduction of count statistics on image quality; achieved by successively reducing imaging time while assessing for the maximum degree of time reduction that can be applied without adversely affecting image quality.

Nudi et al., in a meta-analysis comprised of 2092 individual cases evaluating the diagnostic accuracy of CZT SPECT in comparison to invasive coronary angiography, showed that the CZT SPECT system has a high sensitivity of 84% (95% confidence interval CI:0.78 to 0.89) and a specificity of 69% (95% CI:0.62 to 0.76) for demonstrating obstructive coronary artery disease(26).

In another prospective study by Danad et al.(55), 208 individuals with suspected coronary artery disease underwent coronary CT angiography, conventional nuclear medicine SPECT imaging and O-15 H2O PET-CT imaging, the SPECT study showed a sensitivity of 57% (95% CI, 46%-67%) and a specificity of 94% (95% CI, 88%-98%) and an accuracy of 77%; 95% CI, 71%-83%). There have been efforts to reduce patient radiation dose during myocardial perfusion imaging by implementing an iterative reconstruction algorithm with resolution recovery and wide beam reconstruction algorithm (WBR) using the new dedicated cardiac cameras (DCC) with innovative collimator and CZT detectors. Studies implementing these devices and reconstruction algorithms employed reduction of administered activity by half compared to conventional SPECT cameras(54)(56)(57)(58)(59).

In this work, time-reduced CZT SPECT images with lower count statistics retained acceptable diagnostic accuracy. There were some changes in the quantitative parametric scores among time-reduced images compared to non-time-reduced images; however, the differences were often not significant. There is suggestion, based on this work, that time-reduced-images can be used for diagnostic purposes while maintaining sensitivity, specificity, and accuracy compared to non-time-reduced images even for higher levels of time reduction.

Simulation of reduced imaging time in this work suggests the potential for further reduction of patient administered activity and radiation dose. This requires an assumption that imaging time and administered activity may be adjusted interchangeably to obtain an image with equivalent or similar count statistics.

This work shows that time reduction mainly impacts the specificity and accuracy of polar map interpretation by readers rather than the sensitivity. The ability of the readers to interpret polar maps with certainty is also affected at some point during time reduction. Reader certainty of interpretation of polar maps becomes degraded with sufficient image time reduction. Specifically, the combined two-reader results showed that reader certainty for interpretation of polar maps declined when imaging time was reduced to 60% compared to the current non-time-reduced imaging. The polar maps remained highly interpretable at 88% when imaging time was reduced to 50% compared to non-time-reduced imaging (Fig 2,18 & 2,19).

Our study showed variation in sensitivity and specificity of the polar maps during time reduction. The findings of Fig 2. 19 indicates that the sensitivity of stress polar map interpretation is maintained even when imaging time is reduced to as low as 10%. This suggests that true stress-induced perfusion defects remain detectable at shorter imaging times. In contrast, the specificity of stress polar maps starts to decline when imaging time falls below 50%. This indicates that distinguishing true defects from artifacts becomes more challenging with reduced imaging time.

The question arises as to why the sensitivity of detection of stress polar map defects is preserved down to lower imaging times compared with specificity which is not. The answer may be best understood by first considering a case of a normal resting polar plot and a normal stress polar plot. As imaging time is reduced and noise is created in the plots, artifactual defects can then be created. The specificity of the stress polar map becomes reduced when a significant defect on the stress images occurs with the same region on the rest polar plot appearing relatively normal (Fig. 2-31). Generation of a significant noise-induced defect on the stress polar plot, with no corresponding defect on the rest images, is a relatively high probability event. This apparently begins to occur at 50%-time reduction.

Noise-induced specificity degradation of stress polar plot
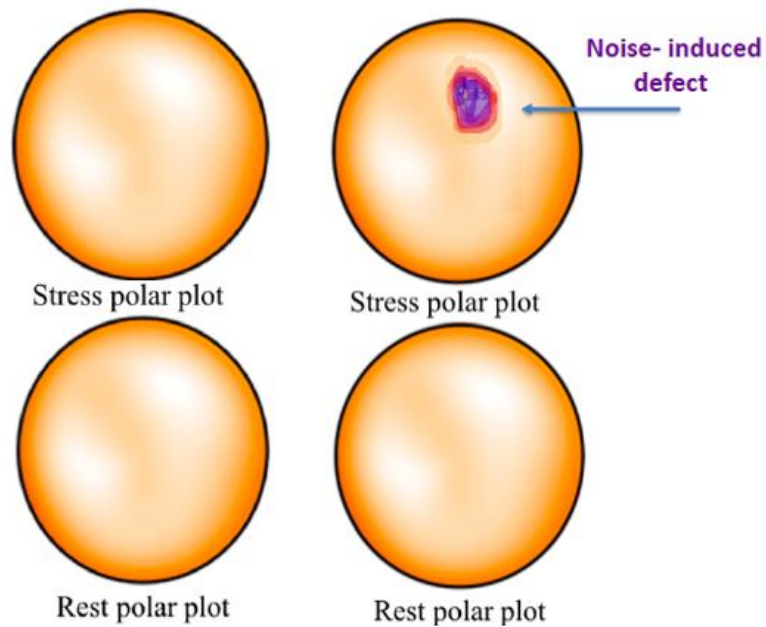
Figure 2. 31 Normal rest and stress polar plots (left) with artifactual noise-induced stress defect (right) reducing the specificity of interpretation of the stress polar plot image. Stress polar plot (top) and rest polar plot (bottom). Noise-induced defect causing false-positive interpretation of stress polar plot specificity for detecting ischemia **(A relatively high probability event-that can occur at higher imaging times).**

By contrast, if one considers a simple case of ischemia, in which the rest scan is normal and the stress scan contains a solitary defect, a degradation in sensitivity would require a noise-induced defect to occur on the rest scan in the same location as the defect already present on the stress scan (Fig. 2-32). This is a relatively low-probability event and would likely only occur after multiple other noise-induced defects have already evolved on the rest scan. It is for this reason that a loss of sensitivity requires much more noise degradation than a loss of specificity.

Noise- induced sensitivity degradation of stress polar plots
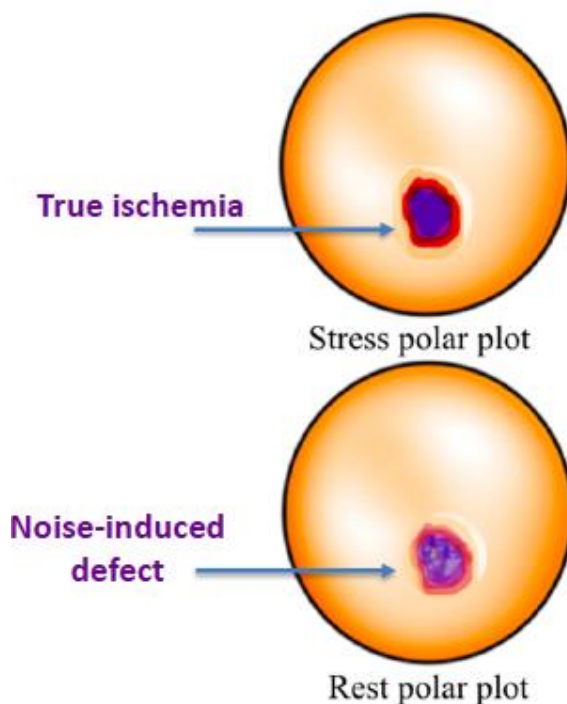
Figure 2. 32 True ischemia on stress polar plot with artifactual noise-induced rest defect reducing the sensitivity of interpretation of the stress polar plot images. Stress polar plot (top) and rest polar plot (bottom). True ischemia is present on stress image. A noise-induced defect on rest imaging in the same region as an ischemic defect on stress image resulting in the false negative interpretation of stress polar plot reducing sensitivity for detection of ischemia **(A relatively low probability event – unlikely to occur at higher imaging times).**

Another possible mechanism for loss in sensitivity of the stress polar plot may be caused by the generation of a sufficient number of random defects on the rest and stress images which can result in the elimination of the context of a single obvious reversible defect, i.e., that so many defects develop on both rest and stress images, that the reversible defect becomes hidden or camouflaged by noise on both scans (Fig. 2-33)

Noise-induced sensitivity degradation of stress polar plots caused by loss of defect contrast
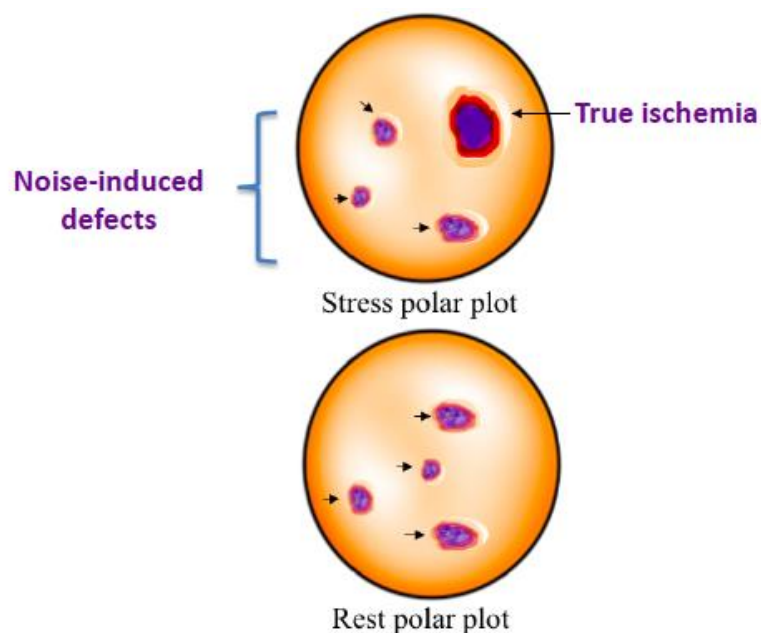
Figure 2. 33 True ischemia on stress polar plot with artifactual noise-induced defects on rest and stress images reducing the sensitivity of interpretation of stress polar plot images. Stress polar plot (top) and rest polar plot (bottom). A true ischemic defect on stress image (long arrow) with multiple noise-induced defects on rest and stress images (short arrows) which camouflages the true ischemic defect on stress images, reducing sensitivity for detection of ischemia. This requires multiple noise events to occur at reduced imaging times **(Requires multiple noise events – more likely to occur at lower imaging times).**

The findings of Fig 2. 18 suggest that reduced imaging time has less detrimental effects on the sensitivity and specificity of the interpretation of rest polar maps. Sensitivity is relatively well-maintained down to 10% imaging time and specificity becomes degraded at 20% or less.

To understand why the sensitivity of interpretation of rest polar maps remains high down to low imaging times, one can consider the effects of count reduction on a case of rest and stress polar plots which both contain the same true resting defect. As imaging time is reduced, a loss in sensitivity requires a loss of context of the defect which can occur

because of noise-created defects hiding real lesions or alternatively because of loss of conspicuity of defect-based lesions due to generalized reduced counts in surrounding normal myocardial segments in the polar plot (Fig. 2-34). A significant loss of counts would be required to compromise the integrity of a true resting lesion which most commonly appears the same on both the rest and stress polar plots. Additionally, both rest and stress gated images are also used by interpreters to assess the validity of a resting perfusion defect, by detection of corresponding abnormal left ventricular wall thickening in the location of resting defect. The added use of gated data may assist a reader in confirming the presence of a true resting defect rather than falsely interpreting the count reduction as artifact (e.g., secondary to attenuation effects), and thereby preserve sensitivity. The specificity of the interpretation of rest polar maps was also maintained down to low imaging times. This contrasts with stress polar plot interpretation in which specificity is degraded with mildly reduced imaging times. To understand why the specificity of interpretation of rest polar maps is maintained down to low imaging times, we consider again the case of two normal rest and stress perfusion plots. A decrease in specificity for resting images would require that two defects occur in the same location on two separate rest and stress polar plots, a relatively low-frequency event (Fig. 2-35). With severe count impairment, such defects may become manifest. Additionally, gated images at higher count states might help to confirm normal wall thickening of a potential noise-induced defect, thereby preserving specificity. At lower count states the gated images themselves would be count deprived and may erroneously confirm impaired wall thickening at sites of artifactually generated rest and stress defects, thereby also contributing to the impairment in specificity.

Noise-induced sensitivity degradation of rest polar plots caused by loss of defect context
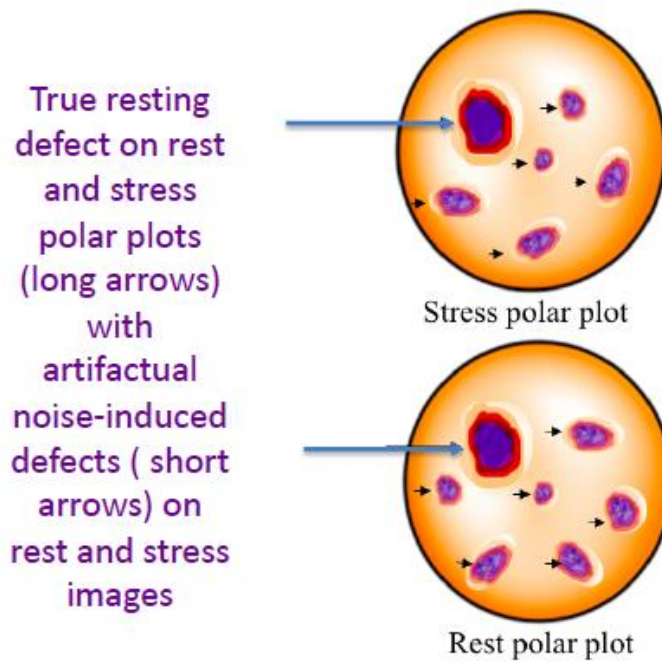
Figure 2. 34 True resting defect on rest and stress polar plots with artifactual noise-induced defects on rest and stress images reducing the sensitivity of interpretation of rest polar plot images. Stress polar plot (top) and rest polar plot (bottom).

A true resting defect on both rest and stress images (long arrow). Multiple noise-induced defects on rest and stress images (short arrows) reduce the conspicuity of the true resting defect on both rest and stress images, reducing the sensitivity for the detection of ischemia. **This requires multiple noise events and would tend to occur at reduced imaging times.**

Noise-induced specificity degradation of rest polar plots
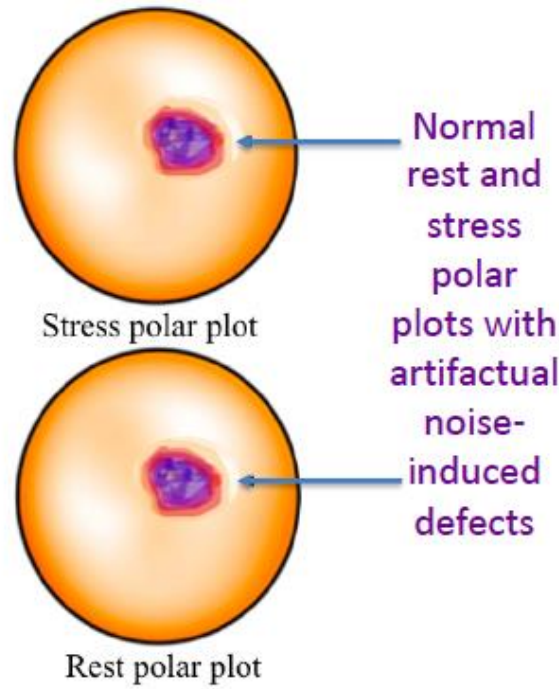
Figure 2. 35: Normal rest and stress polar plots with artifactual noise-induced defects occurring in the same region for both rest and stress images (arrows) reducing the specificity of interpretation of the rest polar plot images. Stress polar plot (top) and rest polar plot (bottom). A noise-induced defect on stress image coincidentally occurs in the same location as a noise-induced rest defect causing a false positive interpretation of rest polar interpretation **(A relatively low probability set of events – unlikely to occur at high imaging times).**

It should be noted that reduced imaging time leads to a more pronounced reduction in specificity. This suggests that as imaging time decreases, there is a greater likelihood of artifactual reversible defects appearing on the polar maps. These artifacts arise due to diminished counts caused by shorter imaging times, resulting in a reduced target-to-background uptake ratio. Consequently, computer algorithms may incorrectly delineate the myocardial wall, contributing to the appearance of these artifacts.

Our study also indicates that reduced imaging time has a less detrimental effect on specificity and sensitivity in the case of rest polar maps. This difference could be attributed to how rest imaging is interpreted and the distinct pattern of attenuation artifacts affecting these images and in combination with stress polar plots.

Gated images are shown to be valuable in accurately identifying artifacts and reducing the likelihood of misinterpreting attenuation artifacts as real defects. Gated images provide added value by aiding in the assessment and confirmation of diagnoses, ideally by demonstrating impaired wall thickening at the locations corresponding to perfusion defects.

A crucial concept in myocardial perfusion imaging interpretation is that both rest and stress polar plots are essential for a comprehensive analysis. In the case of a scar or infarction, a resting defect should be consistently visible on both rest and stress images, maintaining the same appearance in both polar plots. Gated images play a vital role in confirming the diagnoses by unveiling impaired wall thickening at the sites of perfusion defects. Distinguishing stress-induced perfusion defects (in the case of ischemia) involves identifying reductions of count in stress polar plots that are not present in rest images, essentially pinpointing defects in only one polar plot. The probability of randomly encountering a solitary stress defect is considerably higher than randomly observing two perfectly aligned rest and stress defects. Consequently, the specificity of stress images (stress defects) is expected to deteriorate more rapidly with reduced imaging time compared to the specificity of rest defects.

Imaging time reduction showed variation in mean quantitative perfusion parameters for SRS, SSS and TPD. On the other hand, the impact of the score changes on image interpretability, and the accuracy of the final diagnosis was downgraded because image interpretation incorporated gated imaging parameters and wall thickening of regions of myocardium with abnormal scoring on perfusion imaging. This approach helped to differentiate artifacts (usually present on both rest and stress images) from actual perfusion abnormalities which might be present on perfusion images and are also denoted as

perfusion deficits by computer scoring. These artifacts potentially become more prominent during time reduction due to lower count statistics.

The SRS and TPD at rest remained greater than 0.8 for specificity and accuracy for imaging times of 30% or greater compared to non-time-reduced images; however, 0.8 specificity and accuracy were maintained for SSS, SDS and stress TPD for imaging times of 50% or greater compared to non-time reduced images.

Functional parameters were also impacted by time reduction. Myocardial perfusion imaging volumetric parameters obtained by computer software segmentation are dependent on correct contour placement along the epicardial and endocardial borders of the myocardium. The accuracy of segmentation is dependent on the count statistics of the image. The computer algorithm determined the maximum counts per pixel in any given slice and would typically use it to define the mid-myocardial region, then searched for pixels inward and outward of the so-called mid-myocardial pixel to reach a threshold of 2.5 SD of counts compared to the mid-myocardial region. Those pixels define the epicardial and endocardial margins. When imaging time and count statistics are reduced, increased image noise occurs which impairs the algorithm's ability to successfully define layers such as the mid-myocardial region and epicardial and endocardial contours. The resultant failure of the algorithm to correctly delineate myocardial surfaces leads to incorrect calculations of left ventricular volume at rest, at stress, and on gated images.

Other researchers found similar results when reducing administered radioactivity(33)(59). It is noted that the consistency in the findings of this work in comparison with other studies exists even though simulated time-reduced images in this work were reconstructed without implementation of attenuation correction methods (such as CT attenuation maps or supine-prone imaging) which were applied in the other studies.

It was postulated that stress images might be less affected by faulty contour detection with time reduction compared with rest images because of relative higher counts per pixel during stress imaging due to a relative hyperemic state post-stress in which more radioactivity is delivered to the myocardium. The results confirmed that EF on rest images degraded when imaging time was reduced to 50%, while the EF on stress images degraded

when imaging time was reduced to 30%. The EF changes, however, had no effect on image interpretation and did not change the classification of normal vs. abnormal studies. The same behavior was observed for EDV and ESV with no parameter change down to 50% imaging time for rest images and down to 30% imaging time for stress images; and image time reduction did not significantly impact image interpretation or classification of normal vs abnormal. Variation of both parameters became greater when imaging time was reduced below 50% of baseline imaging time at both rest and stress.

A study by Nakazato et al(54) demonstrated that acquisition of one million counts on an LV polar map would produce a myocardial image comparable to an image containing 8.0 million counts, for both quantitative perfusion and gated parameters. For a dedicated cardiac camera with CZT detectors, images can be acquired with a standard administered activity and an imaging time of 1/8th of the standard time (i.e., 1 min 45 s vs. 14 min). The authors showed that reducing administered activity to the patient by a factor of 8 (with a 14 min scan time) or reducing the administered activity by a factor of 6 and scanning the patient for 10 min provided the same image quality. Such reduction of administered activity can reduce the effective radiation dose to the patient to less than 1 mSv without significantly sacrificing accuracy(54). Nakazato's study underscores the significance of the research findings of this work which have shown potential for reducing imaging time in MPI; and that such imaging time reduction may instead be applied toward reducing administered activity in selected patients, thereby further reducing radiation dose delivered to the patient during MPI.

In summary, our study drew a picture of the impact of imaging time reduction on stress and rest polar map interpretation in myocardial perfusion imaging. It emphasizes the challenge of maintaining specificity under time constraints and underscores the importance of gated images in enhancing accuracy. Additionally, our findings highlighted the distinctions between stress and rest defects and their implications for specificity, providing valuable insights regarding the possibility of acquiring interpretable information from MPI during imaging time reduction.

Chapter 3

3   Conclusion

The aim of this research is to evaluate the influence of reducing count statistics on image quality by progressively decreasing imaging time and determining the maximum allowable time reduction without compromising image quality. The study involves the examination of time-reduced CZT SPECT images with lower count statistics, revealing that they maintain acceptable diagnostic accuracy. The current study showed the feasibility of image acquisition time reduction during MPI. Although image time reduction had variable impact on parametric scores, image quality, and image interpretability in time-reduced images compared to non-time-reduced ones, the differences were often not statistically significant. Notably, the study suggests that time-reduced images can be utilized for diagnostic purposes, maintaining sensitivity, specificity, and accuracy, even with higher levels of time reduction. Simulating reduced imaging time in the research suggests the potential for further reduction in patient-administered activity and radiation dose, assuming that imaging time and administered activity are interchangeable to achieve equivalent count statistics. For a Discovery NM 530 CZT camera rest imaging employing 111-278 MBq Tc99m sestamibi on day one and stress imaging employing 111-278 MBq of Tc99m sestamibi on day two, and for a rest imaging time of 10 minutes and for stress imaging time of 8 minutes the highlight of this thesis finding regarding simulated imaging time reduction can be summarized as follow:

1. Sensitivity of stress polar map interpretation is maintained even when imaging time is reduced to as low as 10%, suggesting that true stress-induced perfusion defects remain detectable at shorter imaging times.

2. In contrast, the specificity of stress polar maps starts to decline when imaging time falls below 50%. This indicates that distinguishing true stress defects from artifacts becomes more challenging with relatively smaller reductions in imaging time.

3. Sensitivity and specificity of interpretation of rest polar maps are well-maintained down to 10% imaging time and down to 20% imaging time or less respectively.

4. Imaging time can be reduced with little change to diagnostic accuracy of interpretation of polar maps down to 50% imaging time for the cases included in this investigation. Further evaluation would be needed to confirm whether a 50% imaging time reduction would be valid in cases where counts are substantially reduced such as in cardiomyopathy or in situations of significant patient-related attenuation effects (e.g., elevated BMI).

5. Implementing attenuation correction by CT-attenuation map would improve the report's certainty and the image's interpretability.

The study demonstrates that time reduction primarily impacts the specificity and accuracy of polar map interpretation by readers rather than sensitivity. The findings also underscore distinctions between stress and rest defects, offering valuable insights for acquiring interpretable information from MPI during imaging time reduction. Future work may explore optimizing imaging protocols for improved efficiency without compromising diagnostic accuracy.

3.1   Limitation and Future Work

3.1.1 Limitation

There were some limitations to our work. The first was related to normalization in our study which was done based on a normal database created from non-time-reduced images of normal persons. The parametric scores of the polar maps, specifically TPD, are based on comparing the patient count distribution on the myocardium with a normal database. Many factors should be considered for an accurate comparison, including gender, administered activity, camera specification and algorithm for image reconstruction(42). Also, comparing polar maps between different camera systems and software with various setups needed a new specific normal database to normalize the polar map(60). Using a full-time/ full-count normal database for imaging with various count statistics was associated with increasing bias in computer-generated scores. Creating a normal database from count-reduced images would limit this bias due to changes in the normal threshold(54).

Another study showed that the normal database and MPI parameters depend mainly on count statistics. The same research on one type of camera (Philips) concluded that a

threshold of 50% reduction in the count would be a limit that allowed the reduced dose images to be comparable with the existing normal database to prevent a significant variation in myocardial perfusion quantification. This result has not been tested for other software packages(47).

Our study results about the accuracy of MPI parameters in low-count images are impacted by comparing lower-count statistics images with full-count normal databases.

The sample size in the study was another limitation factor. Even though patients with large body habitus and non-ischemic underlying heart disease were included, the sample size prevents comparison between different types of patients.

The score changes could be attributed to the fact that imaging in this cohort was acquired without correcting for photon attenuation, which imposed artifacts. These artifacts also impact the interpretability of the image by physicians and the certainty of the report to a lesser degree.

Lastly, the study was done in a single center which imposed another limitation.

3.1.2 Future Work

Creating a normal database for time-reduced imaging protocol is essential to improve normalization and analysis for time-reduced images.

Attenuation correction protocol would help improve the confidence and interpretability of the report provided by the physician.

Future multicentric research in a larger cohort with diversity in body habitus and underlying heart disease, including patients with cardiomyopathy, would help increase the generalizability of the results of the time reduction protocol.

Polar map count distribution demonstrated heterogeneity during time reduction, and some regions showed more heterogeneity during time reduction, like in the inferior wall, which caused artifacts. Comparing the count statistics in various vascular territories would be an

exciting topic. This subject is also interesting for defining the presence of artifacts during time reduction.

Finally, exploring the impact of reduced administered activity on image quality interchangeably with time reduction would be important from the perspective of total radiation dose reduction to the patient, and would support adherence to the 'As Low As Reasonably Achievable' principle or ALARA, as introduced by International Commission on Radiological Protection and advocated by radiology societies(21)(61).

References

1. Government of Canada. Heart Disease in Canada [Internet]. [cited 2022 Oct 17]. Available from: https://www.canada.ca/en/public-health/services/publications/diseases-conditions/heart-disease-canada.html

2. Secretariat MA. Non-Invasive Cardiac Imaging Technologies for the Diagnosis of Coronary Artery Disease A Summary of Evidence-Based Analyses Medical Advisory Secretariat Ministry of Health and Long-Term Care. *Ont Heal Technol Assess Ser* [Internet]. 2010;10(7):1–40. Available from: http://www.health.gov.on.ca/ohtas.

3. Loewen OK, Ekwaru JP, Ohinmmaa A VP. Economic burden of not complying with Canadian food recommendations in 2018. *Nutrients* [Internet]. 2019 [cited 2021 May 22];11(10):2529. Available from: /pmc/articles/PMC6835951/

4. Dewey M, Siebes M, Kachelrieß M, Kofoed KF, Maurovich-Horvat P, Nikolaou K, Bai W, Kofler A, Manka R, Kozerke S, Chiribiri A, Schaeffter T, Michallek F, Bengel F, Nekolla S, Knaapen P, Lubberink M, Senior R, Tang MX, Piek JJ, van de Hoef T, Martens J SLQCISG. Clinical quantitative cardiac imaging for the assessment of myocardial ischaemia. *Nat Rev Cardiol* [Internet]. 2020;17(7):427–50. Available from: http://www.nature.com/articles/s41569-020-0341-8

5. Jain D. Technetium-99m labeled myocardial perfusion imaging agents. *Semin Nucl Med*. 29(3):221–36.

6. Nakano S, Trummer M. 4D Reconstruction of Dynamic Studies with the Discovery NM 530c SPECT Camera. Mathematics Thesis. [Internet]. Simon Fraser; 2016. Available from: https://summit.sfu.ca/item/16400

7. INTERNATIONAL ATOMIC ENERGY AGENCY. Nuclear Cardiology: Guidance on the Implementation of SPECT Myocardial Perfusion Imaging. IAEA Human Health Series No. 23 (Rev. 1), IAEA, Vienna; 2016.

8. Hachamovitch R. Does Ischemia Burden in Stable CoronaryArtery Disease Effectively IdentifyRevascularization Candidates? *Circ Cardiovasc Imaging*. 2015;8(5):discussion p 8.

9. Zeiher AM, Drexler H, Wollschläger H JH. Endothelial Dysfunction of the Coronary Microvasculature Is Associated With Impaired Coronary Blood Flow Regulation in Patients With Early Atherosclerosis. *Circulation* [Internet]. 1991 [cited 2021 May 11];84(5):1984–92. Available from: http://ahajournals.org

10. Salerno M BG. Noninvasive assessment of myocardial perfusion. *Circ Cardiovasc Imaging* [Internet]. 2009 [cited 2021 May 11];2(5):412–24. Available from: http://ahajournals.org

11. Lebowitz E, Greene MW, Fairchild R, Bradley-Moore PR, Atkins HL, Ansari AN, et al. Thallium-201 for Medical Use. I. *J Nucl Med*. 1975;16(2).

12. Savi A, Gerundini P, Zoli P, Maffioli L, Compierchio A, Colombo F, Matarrese M DE. Biodistribution of Tc-99m methoxy-isobutyl-isonitrile (MIBI) in humans. *Eur J Nucl Med*. 1989;15(9):597–600.

13. Carvalho PA, Chiu ML, Kronauge JF, Kawamura M, Jones AG, Holman BL, et al. Subcellular Distribution and Analysis of Technetium-99m-MIBI in Isolated Perfused Rat Hearts. Vol. 33, The Journalof NuclearMedicineâ€¢.

14. Anger H. Use of a Gamma-Ray Pinhole Camera for in vivo Studies. *Nature* [Internet]. 1952;170(4318):200–1. Available from: https://www.nature.com/articles/170200b0

15. Bocher M, Blevis IM, Tsukerman L, Shrem Y, Kovalski G, Volokh L. A fast cardiac gamma camera with dynamic SPECT capabilities: Design, system validation and future potential. *Eur J Nucl Med Mol Imaging*. 2010;37(10):1887–902.

16. Peterson T, Furenlid L. SPECT detectors: The Anger Camera and beyond. *Phys Med Biol*. 2011;56(17):R145-82.

17. Bailey DL, Humm JL, Todd-Pokropek A, Aswegen A van. Nuclear Medicine Physics. A Handbook for Teachers and Students. *Med Phys*. 2014;

18. Dorbala S, Ananthasubramaniam K, Armstrong IS, Chareonthaitawee P, DePuey EG, Einstein AJ, et al. Single Photon Emission Computed Tomography (SPECT) Myocardial Perfusion Imaging Guidelines: Instrumentation, Acquisition, Processing, and Interpretation. *J Nucl Cardiol* [Internet]. 2018;25(5):1784–846. Available from: https://doi.org/10.1007/s12350-018-1283-y

19. Gullberg GT, Reutter BW, Sitek A, Maltz JS, Budinger TF. Dynamic single photon emission computed tomography—basic principles and cardiac applications. *Phys Med Biol* [Internet]. 2010;55(20):R111–91. Available from: https://iopscience.iop.org/article/10.1088/0031-9155/55/20/R01

20. Itti R, Casset D, Philippe L, Brochier M. Single photon emission computed tomography of the heart: A functional image? *Int J Card Imaging*. 1986;2(1):47–52.

21. Dorbala S, Di Carli MF, Delbeke D, Abbara S, De Puey EG, Dilsizian V, et al. SNMMI/ASNC/SCCT Guideline for Cardiac SPECT/CT and PET/CT 1.0. *J Nucl Med* [Internet]. 2013 [cited 2022 Feb 19];54(8):1485–507. Available from: https://jnm.snmjournals.org/content/54/8/1485

22. Ljungberg M, Pretorius PH. SPECT/CT: an update on technological developments and clinical applications. *Br J Radiol* [Internet]. 2016;90. Available from: https://doi.org/10.1259/bjr.20160402

23. Patton J, Slomka P, Germano G, Berman D. Recent technologic advances in nuclear cardiology. *J Nucl Cardiol* [Internet]. 2007;14(4):501–13. Available from:

http://link.springer.com/10.1016/j.nuclcard.2007.06.003

24.   Patton J, Sandler M, Berman D, Vallabhajosula S, Dickman D, Gambhir S, et al. D-
      SPECT: A new solid state camera for high speed molecular imaging. *J Nucl Med*
      [Internet]. 2006;47(suppl 1):189P LP-189P. Available from:
      http://jnm.snmjournals.org/content/47/suppl_1/189P.1.abstract

25.   Garcia E V, Faber TL, Esteves FP. Cardiac Dedicated Ultrafast SPECT Cameras:
      New Designs and Clinical Implications. *J Nucl Med* [Internet]. 2011;52(2):210 LP –
      217. Available from: http://jnm.snmjournals.org/content/52/2/210.abstract

26.   Nudi F, Iskandarian A, Schillaci O, et.al. Diagnostic Accuracy of Myocardial
      Perfusion Imaging With CZT Technology Systemic Review and Meta-Analysis of
      Comparison With Invasive Coronary Angiography. *ACC Cardiovasc Imaging*.
      2017;10(7):787–94.

27.   Miao TL, Kansal V, Glenn Wells R, Ali I, Ruddy TD, Chow BJW. Adopting new
      gamma cameras and reconstruction algorithms: Do we need to re-establish normal
      reference values? *J Nucl Cardiol* [Internet]. 2016;23(4):807–17. Available from:
      https://link.springer.com/content/pdf/10.1007/s12350-015-0172-x.pdf

28.   Abbott BG, Case JA, Dorbala S, Einstein AJ, Galt JR, Pagnanelli R, et al.
      Contemporary Cardiac SPECT Imaging-Innovations and Best Practices: An
      Information Statement from the American Society of Nuclear Cardiology. *J Nucl
      Cardiol* [Internet]. 2018;25:1847–60. Available from:
      https://doi.org/10.1007/s12350-018-1283-y]

29.   Erlandsson K, Kacperski K, van Gramberg D, Hutton BF. Performance evaluation of
      D-SPECT: a novel SPECT system for nuclear cardiology. *Phys Med Biol* [Internet].
      2009;54(9):2635–49. Available from:
      https://iopscience.iop.org/article/10.1088/0031-9155/54/9/003

30.   Herzog BA, Buechel RR, Katz R, Brueckner M, Husmann L, Burger IA, et al.
      Nuclear Myocardial Perfusion Imaging with a Cadmium-Zinc-Telluride Detector

Technique: Optimized Protocol for Scan Time Reduction. *J Nucl Med* •. 2010;51(1):46–51.

31.   Sharir T, Slomka PJ, Hayes SW, DiCarli MF, Ziffer JA, Martin WH, Dickman D, Ben-Haim S BD. Multicenter Trial of High-Speed Versus Conventional Single-Photon Emission Computed Tomography Imaging: Quantitative Results of Myocardial Perfusion and Left Ventricular Function. *J Am Coll Cardiol* [Internet]. 2010;55(18):1965–74. Available from: https://www.jacc.org/doi/full/10.1016/j.jacc.2010.01.028

32.   Ramon AJ, Yang Y, Pretorius PH, Slomka PJ, Johnson KL, King MA, et al. Investigation of dose reduction in cardiac perfusion SPECT via optimization and choice of the image reconstruction strategy. *J Nucl Cardiol* [Internet]. 25. Available from: http://www.springerlink.com

33.   Einstein AJ, Blankstein R, Andrews H, Fish M, Padgett R, Hayes SW, et al. Comparison of Image Quality, Myocardial Perfusion, and Left Ventricular Function Between Standard Imaging and Single-Injection Ultra-Low-Dose Imaging Using a High-Efficiency SPECT Camera: The MILLISIEVERT Study. *J Nucl Med*. 2014;55(9):1430–7.

34.   Czaja MZ, Wygoda Z, Duszańska A, Szczerba D, Głowacki J, Gąsior M, et al. Myocardial perfusion scintigraphy – interpretation of gated imaging. Part 2. *Kardiochirurgia i Torakochirurgia Pol* [Internet]. 2018;15(1):49–56. Available from: https://doi.org/10.5114/kitp.2018.74676

35.   Germano G, Kiat H, Kavanagh PB, Moriel M, Mazzanti M, Su HT, et al. Automatic quantification of ejection fraction from gated myocardial perfusion SPECT. *J Nucl Med*. 1995;36(11):2138–47.

36.   Faber TL, Cooke CD, Folks RD, Vansant JP, Nichols KJ, DePuey EG, Pettigrew RI GE. Left Ventricular Function and Perfusion from Gated SPECT Perfusion Images: An Integrated Method. *J Nucl Med*. 1999;40(4):650–9.

37.   Germano G, Kavanagh PB, Waechter P, Areeda J, Van Kriekinge S, Sharir T, et al.
      A new algorithm for the quantitation of myocardial perfusion SPECT. I: Technical
      principles and reproducibility. *J Nucl Med.* 2000;41(4):712–9.

38.   Germano G, Kavanagh PB, Slomka PJ, Van Kriekinge SD, Pollard G, Berman DS.
      Quantitation in gated perfusion SPECT imaging: The Cedars-Sinai approach. *J Nucl
      Cardiol* [Internet]. 2007 [cited 2021 May 15];14(4):433–54. Available from:
      https://pubmed.ncbi.nlm.nih.gov/17679052/

39.   Garcia EV, Faber TL, Cooke CD, Folks RD, Chen J SC. The increasing role of
      quantification in clinical nuclear cardiology: The Emory approach. *J Nucl Cardiol*
      [Internet]. 2007 [cited 2021 May 15];14(4):420–32. Available from:
      https://pubmed.ncbi.nlm.nih.gov/17679051/

40.   Ficaro EP, Lee BC, Kritzman JN, Corbett JR. Corridor4DM: The Michigan method
      for quantitative nuclear cardiology. *J Nucl Cardiol* [Internet]. 2007 [cited 2021 May
      15];14(4):455–65. Available from: https://pubmed.ncbi.nlm.nih.gov/17679053/

41.   Germano G, Kavanagh PB, Su H-T, Mazzanti M, Kiat H, Hachamovitch R, et al.
      Automatic Reorientation of Three-Dimensional, Transaxial Myocardial Perfusion
      SPECT Images. *J Nucl Med* [Internet]. 1995 [cited 2021 Sep 12];36(6):1107–14.
      Available from: https://pubmed.ncbi.nlm.nih.gov/7769436/

42.   Rubeaux M, Xu Y, Germano G, Berman DS, Slomka PJ. Normal Databases for the
      Relative Quantification of Myocardial Perfusion. *Curr Cardiovasc Imaging Rep*
      [Internet]. 2016;9(8):22. Available from: http://link.springer.com/10.1007/s12410-
      016-9385-x

43.   Pelletier-Galarneau M, Ruddy TD. The potential of regional myocardial blood flow
      measurement with SPECT. *J Nucl Cardiol*. 2021;28(1):260–2.

44.   Depasquale EE, Nody AC, Gordon Depuey E, Garcia E V, Pilcher G, Bredlau C, et
      al. Quantitative rotational thallium-201 tomography for identifying and localizing
      coronary artery disease. *Circulation* [Internet]. 1988 [cited 2021 Sep 7];77(2):316–

27. Available from: http://ahajournals.org

45.   Slomka PJ, Nishina H, Berman DS, Kang X, Friedman JD, Hayes SW, Aladl UE GG. Automatic Quantification of Myocardial Perfusion Stress–Rest Change: A New Measure of Ischemia. *J Nucl Med* [Internet]. 2004 [cited 2021 Sep 19];45(2):183–91. Available from: https://pubmed.ncbi.nlm.nih.gov/14960634/

46.   Maddahi J, van Train K, Prigent F, Garcia E V., Friedman J, Ostrzega E, et al. Quantitative single photon emission computed thallium-201 tomography for detection and localization of coronary artery disease: Optimization and prospective validation of a new technique. *J Am Coll Cardiol* [Internet]. 1989 [cited 2023 Jul 11];14(7):1689–99. Available from: https://www.sciencedirect.com/science/article/pii/073510978990017X

47.   Scabbio C, Malaspina S, Capozza A, Selvaggi C, Matheoud R, Del Sole A LM. Impact of low-dose SPECT imaging on normal databases and myocardial perfusion scores. *Phys Med* [Internet]. 2019 [cited 2022 Oct 17];59:163–9. Available from: http://www.physicamedica.com/article/S1120179719300523/fulltext

48.   Garcia E V., Slomka P, Moody JB, Germano G, Ficaro EP. Quantitative Clinical Nuclear Cardiology, Part 1: Established Applications. *J Nucl Cardiol*. 2020;27(1):189–201.

49.   Czaja M, Wygoda Z, Duszańska A, Szczerba D, Głowacki J, Gąsior M WJ. Interpreting myocardial perfusion scintigraphy using single-photon emission computed tomography. Part 1. *Kardiochir Torakochirurgia Pol* [Internet]. 2017 [cited 2021 Jul 26];14(3):192–9. Available from: https://pubmed.ncbi.nlm.nih.gov/29181048/

50.   Lecchi M, Martinelli I, Zoccarato O, Maioli C, Lucignani G, Sole A Del. Comparative analysis of full-time, half-time, and quarter-time myocardial ECG-gated SPECT quantification in normal-weight and overweight patients. *J Nucl Cardiol* [Internet]. 2017 [cited 2021 Nov 7];24(3):876–87. Available from: https://pubmed.ncbi.nlm.nih.gov/26911365/

51. Gatidis S, Würslin C, Seith F, Schäfer JF, la Fougère C, Nikolaou K, Schwenzer NF SH. Towards tracer dose reduction in PET studies: Simulation of dose reduction by retrospective randomized undersampling of list-mode data. *Hell J Nucl Med* [Internet]. 2016 [cited 2021 Jul 24];19(1):15–8. Available from: www.nuclmed.gr

52. Pretorius PH, Ramon AJ, King MA, Konik A, Dahlberg ST, Parker MW, Botkin NF, Johnson KL, Yang Y WM. Retrospective fractional dose reduction in Tc-99m cardiac perfusion SPECT/CT patients: A human and model observer study. *J Nucl Cardiol* [Internet]. 2021 [cited 2021 Nov 7];28(2):624–37. Available from: https://pubmed.ncbi.nlm.nih.gov/31077073/

53. Watabe H, Matsumoto K, Senda M, Iida H. Performance of list mode data acquisition with ECAT EXACT HR and ECAT EXACT HR+ positron emission scanners. *Ann Nucl Med* [Internet]. 2006 [cited 2021 Dec 23];20(3):189–94. Available from: https://pubmed.ncbi.nlm.nih.gov/16715949/

54. Nakazato R, Berman DS, Hayes SW, Fish M, Padgett R, Xu Y, et al. Myocardial Perfusion Imaging with a Solid-State Camera: Simulation of a Very Low Dose Imaging Protocol. *J Nucl Med* [Internet]. 2013;54(3):373–9. Available from: https://pubmed.ncbi.nlm.nih.gov/23321457/

55. Danad I, Raijmakers PG, Driessen RS, Leipsic J, Raju R, Naoum C, et al. Comparison of Coronary CT Angiography, SPECT, PET, and Hybrid Imaging for Diagnosis of Ischemic Heart Disease Determined by Fractional Flow Reserve Supplemental content. *JAMA Cardiol* [Internet]. 2017;2(10):1100–7. Available from: https://jamanetwork.com/

56. Dorbala S, Blankstein R, Skali H, Park MA, Fantony J, Mauceri C, Semer J, Moore SC DCM. Approaches to reducing radiation dose from radionuclide myocardial perfusion imaging. *J Nucl Med* [Internet]. 2015;56(4):592–9. Available from: https://pubmed.ncbi.nlm.nih.gov/25766891/

57. DePuey EG, Bommireddipalli S, Clark J, Leykekhman A, Thompson LB FM. A comparison of the image quality of full-time myocardial perfusion SPECT vs wide

beam reconstruc- tion half-time and half-dose SPECT. *J Nucl Cardiol* [Internet].
2011;18:273–80. Available from: https://pubmed.ncbi.nlm.nih.gov/21287370/

58. Bateman TM, Heller GV, McGhie AI, Courter SA, Golub RA, Case JA CS.
Multicenter investigation comparing a highly efficient half-time stress-only
attenuation correction approach against standard rest-stress Tc-99m SPECT imaging.
J Nucl Cardiol [Internet]. 2009;16(5):726–35. Available from:
https://pubmed.ncbi.nlm.nih.gov/19548048/

59. Marcassa C, Campini R, Zoccarato O CP. Wide beam reconstruction for half-dose or
half-time cardiac gated SPECT acquisitions: optimization of resources and reduction
in radiation exposure. *Eur J Nucl Med Mol Imaging* [Internet]. 2011;38(3):499–508.
Available from: https://pubmed.ncbi.nlm.nih.gov/21069317/

60. Zoccarato O, Marcassa C, Lizio D, Leva L, Lucignani G, Savi A, Scabbio C,
Matheoud R, Lecchi M BM. Differences in polar-map patterns using the novel
technologies for myocardial perfusion imaging. *J Nucl Cardiol* [Internet].
2017;24(5):1626–36. Available from: https://pubmed.ncbi.nlm.nih.gov/27233252/

61. ICRP. Recommendations of the ICRP. ICRP Publication 26. *Ann ICRP* [Internet].
1977 [cited 2023 Jul 19];1(3). Available from:
https://www.icrp.org/publication.asp?id=icrp publication 26

Curriculum Vitae

Name: Alireza Khatami

Post-secondary   The University of Western Ontario
Education and   London, Ontario, Canada
Degrees: 2021-2023, MSc. Medical Biophysics.

                     The University of Western Ontario
                     London, Ontario, Canada
                     2017-2022, Nuclear Medicine Residency

                     Shahid Beheshti University of medical sciences SBMU
                     Tehran, Iran
                     1998-2001, Diagnostic Radiology Residency.

                     Tehran University of Medical Sciences
                     Tehran, Iran
                     1989-1996, Medicine.

Honours and   Award winner, educational exhibit, Canadian Association of
Awards: Radiologist, May 2015

                     Medical Imaging Outstanding Teaching Award SBMU, IRAN
                     2009

Related Work   Nuclear Medicine Specialist
Experience   The University of Ottawa 2023

                     Consultant Radiologist, Iran
                     SBMU 2004-2012

Poster Presentation

Alireza Khatami, James, Warrington, Robert Stodilka. The impact of simulated image acquisition time reduction on image quality and parameters of myocardial perfusion imaging using a dedicated cardiac camera, Canadian Association of Nuclear Medicine CANM 2022 Annual Conference, Sep 29-Oct 1, 2022, Montreal QC, Canada.

Publications:

Alireza Khatami, Golmehr Sistani, Duncan Sutherland, et al. Toxicity and Tolerability of 177Lu-DOTA-TATE PRRT with a Modified Administered Activity Protocol in NETs of Variable Origin – A Phase 2 Registry Study. Current Radiopharmaceuticals. 2022;15(2):123-33. DOI: 10.2174/18744710146662108101 00435.

Swiha M, Sutherland DEK, Golmehr Sistani G, Khatami A, Abazid R, Mujoomdar A, Wiseman D, Romsa J, Reid R, Laidley D. Survival predictors of 177Lu-Dotatate peptide receptor radionuclide therapy (PRRT) in patients with progressive well- differentiated neuroendocrine tumors (NETS). J Cancer Res Clin Oncol. 2022 Jan;148(1):225-236. doi: 10.1007/s00432-021-03672-w. Epub 2021 Jun 10. PMID: 34110489; PMCID: PMC8752529.

Abazid RM, Khatami A, Romsa JG, Warrington JC, Akincioglu C, Stodilka RZ, Fox S, Kiaii B, Vezina WC. Hiatal hernia after robotic-assisted coronary artery bypass graft surgery. J Thorac Dis 2021 http://dx.doi.org/10.21037/jtd-20-2557.

Sistani G, Sutherland DEK, Mujoomdar A, Wiseman D, Khatami A, Tsvetkova E, Reid RH, Laidley DT. Efficacy of 177Lu-Dotatate Induction and Maintenance Therapy of Various Types of Neuroendocrine Tumors: A Phase II Registry Study.Curr. Oncol. 2021, 28, 115–127.